Magnetism and Lattice Dynamics under High Pressure Studied by Nuclear Resonant Scattering of Synchrotron Radiation

Dem Fachbereich Physik
der Universität - GH - Paderborn
zur Erlangung des Grades eines Doktors der
Naturwissenschaften (Dr. rer. nat.)

vorgelegte

Dissertation

von

Rainer Lübbers

Paderborn, im März 2000

Gutachter: Prof. Dr. G. Wortmann
Prof. Dr. W.B. Holzapfel

Tag der Einreichung: 9.3.2000
Tag der mündlichen Prüfung: 16.05.2000

Contents

Chapter 1

Introduction

High-pressure experiments with conventional Mössbauer Spectroscopy (MS) are well established since the early days of this method [PBD61, Hol75]. Up to now, high-pressure MS delivers very useful information in many scientific fields such as solid-state physics, geophysics or mineralogy [TP90, MH98]. The study of magnetism is one of the most prominent subjects for high-pressure MS. Here, both the magnetic ordering temperatures and local moments can be studied. When diamond-anvil cells (DACs) are used, MS is possible at pressures well above 100 GPa (corresponding to 1 Mbar) [PTJ97], allowing a huge variation of the lattice parameters.

The use of synchrotron radiation (SR) for Mössbauer Spectroscopy was proposed in 1974 [Rub74], the first successful experiments were performed a decade later by the group of E. Gerdau using nuclear Bragg reflection from an YIG single crystal [GRW85]. Polycrystalline samples could be investigated with the method of Nuclear Forward Scattering (NFS) introduced in 1991 by Hastings et al. [HSB91, BSH92]. It became immediately evident that the NFS method, which is the time analog of the classical Mössbauer effect, is especially suited for high-pressure experiments with DACs by taking advantage of the laser-like collimation of SR.

The extremely fruitful symbiosis between high-pressure research and synchrotron radiation is documented by an enormous progress of x-ray diffraction studies in the Mbar range [LLH96, LTW99]. Other SR methods benefitted also very much from this development, enabling high-pressure studies, for instance, with x-ray absorption [BFM98], inelastic x-ray scattering [KMM97] and x-ray fluorescence [BSS99].

The subject of this thesis are high-pressure studies with two new methods applying Nuclear Resonant Scattering of SR. These methods are:

(a) Nuclear Forward Scattering of SR for the study of hyperfine interactions, based on recoilless absorption and emission of gamma quanta similar to conventional MS, and

(b) Nuclear Inelastic Scattering (NIS) of SR, which uses the energy transfer connected with the inelastic nuclear absorption of gamma quanta. This new method, introduced

in 1995 by M. Seto et al. [SYK95] and W. Sturhahn et al. [STA95], allows a direct experimental determination of the phonon density of states (DOS) in a solid.

In both cases specially modified diamond-anvil cells are used. The NFS studies are concerned with the magnetism in RFe_2 Laves phases, the NIS studies with the phonon DOS in the α- and ε-phase of metallic iron.

To (a): Magnetic intermetallic compounds of rare earth elements (R) with iron-group transition metals have been intensively studied since decades both for a principal understanding of their magnetic properties as well as for technological application. In this thesis the magnetic properties of RFe_2 Laves phases (R=Y, Gd, Sc) are studied with NFS at pressures up to about 100 GPa. Due to their simple crystallographic structures, these RFe_2 systems are considered as model systems for magnetism in R-Fe compounds. The application of external pressure allows for a systematic study of the large variety of magnetic properties in these systems, which are normally caused by the different constituents R [BCK90]. The present work is a continuation of the first high-pressure NFS study of the α-ε transition in metallic iron, performed by H.F. Grünsteudel in the framework of his PhD thesis at the University of Paderborn [Grü97].

To (b): The inner core of the Earth is composed almost entirely of iron or iron-rich alloys [Buk99]. This geophysical aspect is one of the many motivations to study the phase diagram of iron with its various isomorphs in a wide pressure and temperature range. The hcp high-pressure phase of iron (ε-Fe) is considered the most relevant phase for the solid inner core [YAC95]. While a considerable amount of data on the pressure and temperature phase diagram of iron is available [And97], there is much less experimental information on the lattice dynamics of ε-Fe. Here we determine experimentally with NIS up to 42 GPa the phonon DOS in the α-phase and, for the first time, in the ε-phase of iron. From these data a variety of thermodynamic parameters were derived, such as Debye temperatures, Grüneisen parameters, the vibrational contributions to entropy and specific heat. Of particular geophysical interest are the derived sound velocities.

The thesis is organized as follows: The special properties of SR are described in chapter 2. Chapter 3 provides an introduction to the basic features of Nuclear Resonant Scattering. A considerable part of the thesis work was concerned with the development of new diamond-anvil cells and gasket materials. These experimental aspects are outlined in chapter 4 together with the experimental set-up of the Nuclear Resonance Beamline at the European Synchrotron Radiation Facility (Grenoble). The experimental results of NFS high-pressure studies of RFe_2 systems and the derived magnetic properties are presented and discussed in chapter 5. The NIS study of the phonon DOS in iron and the derived thermodynamic properties are contained in chapter 6. The final chapter summarizes the results and gives an outlook to future NFS and NIS experiments.

Chapter 2

Synchrotron Radiation

The investigation of magnetic and dynamic properties of RFe_2 systems and metallic iron in this thesis was performed with Nuclear Resonant Scattering (NRS). The rapid development of this new spectroscopy and its applicability at very high pressures is made possible by the special properties of synchrotron radiation (SR) at third generation sources like the *European Synchrotron Radiation Facility* (ESRF) in Grenoble or the *Advanced Photon Source* (APS) at the Argonne National Laboratory, Chicago.

The aim of this chapter is to introduce briefly the basic features of SR followed by a short description of radiation sources. For further details the reader is referred to the literature [Jac75, IFF92].

2.1 Basic Features

Synchrotron Radiation is electromagnetic radiation which is emitted by charged relativistic particles on a curved trajectory. It is no longer used at circular particle accelerators (the actual *synchrotrons*) but at storage rings, where the particles are stored at constant energy E. In this case the radiated power is [Jac75]

$$P_S = \frac{e^2 c}{6\pi\varepsilon_0 (m_0 c^2)^4} \frac{E^4}{R^2} \tag{2.1}$$

with particle charge e and rest mass m_0, vacuum permittivity ε_0 and radius of curvature R.

Due to the factor m_0^4 in the denominator, it is obvious that only light particles such as electrons or positrons are used for the generation of SR. In a magnetic field B, the particles can be forced to follow a circular trajectory with radius

$$R\,[m] = 3.336\ \frac{E\ [GeV]}{B\,[T]} \tag{2.2}$$

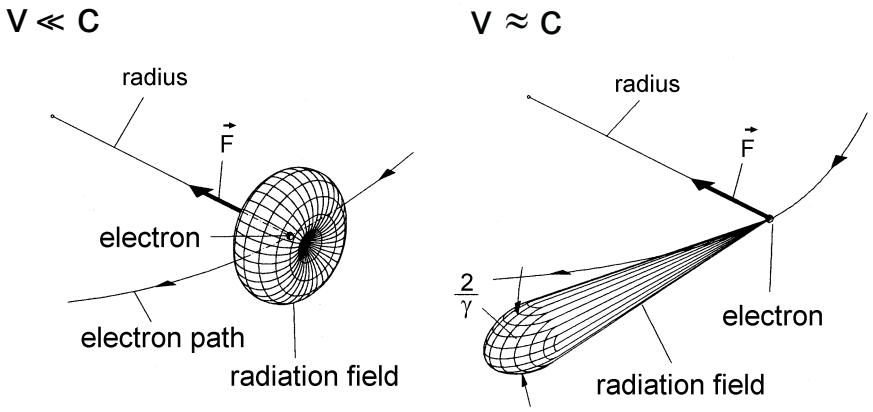

Figure 2.1: Emission of radiation from a radially accelerated electron for non-relativistic (left) and relativistic (right) velocities [Wil96].

The energy loss during one cycle of a relativistic electron is

$$\Delta E\ [keV] = 88.46\ \frac{E^4\ [GeV]}{R\ [m]}. \tag{2.3}$$

For the storage ring at the ESRF with $E = 6\ GeV$ and $R = 23.4\ m$, one obtains 4.9 MeV per cycle. The resulting total radiation power along the ring is 490 kW, when a typical beam current of 100 mA is assumed.[1]

The radiation pattern of a radially accelerated electron is shown in figure 2.1 for velocities $v \ll c$ and $v \approx c$. The radial distribution for the non-relativistic case has the well-known dipole character, whereas for $v \approx c$ one has to perform a Lorentz transformation. The radiation in the laboratory frame is emitted into a small cone with an energy-dependent opening angle

$$\Theta\ = \frac{1}{\gamma} = \frac{m_0 c^2}{E}. \tag{2.4}$$

As a consequence, the radiation seen by a stationary observer is a short pulse originating from the passing electron. This leads to a wide distribution of the energy spectrum, which is characterized by the critical energy [IFF92]

$$E_c = \frac{3\hbar c \gamma^3}{2R} = 2.22\ \text{keV}\,\frac{(E\ [\text{GeV}])^3}{R\ [m]} \tag{2.5}$$

below which half of the radiation power is emitted. The critical energy for a bending magnet at the ESRF is E_c= 20.5 keV.

[1]This value represents the minimum power for re-acceleration of the electrons. With additional *Insertion Devices* (see section 2.2) an actual power of about 5 MW is necessary at ESRF to keep up the beam [ESR96].

Intensity

For a quantitative description of SR sources, the three physical parameters *brightness*, *flux* and *brilliance* are defined [IFF92]. *Brightness* is the number of photons per second which are emitted in a solid angle of 1 mrad^2 within an energy bandwidth $\Delta E/E = 0.1\%$. Integration over the vertical opening angle of the beam gives the *flux*. If the *brightness* is normalized to the size of the electron beam (in mm^2), one obtains the *brilliance* which is given by

$$\text{brilliance} = \frac{\text{photons/s}}{\text{solid angle [mrad}^2\text{]} \cdot \text{source size [mm}^2\text{]} \cdot 0.1\% \text{ bandwidth}} \tag{2.6}$$

This parameter is a measure of the spatial photon density in the beam and therefore most important for high pressure experiments.

2.2 Insertion Devices

Very high brilliance SR is generated by *insertion devices*, which consist of periodic magnetic structures installed in the straight sections of a storage ring (see figure 2.2). Their purpose is to force the particles on a sinusoidal trajectory and enhance the emitted radiation without perturbing the stored electron beam. The optical properties of an insertion device are characterized by the undulator parameter K: the ratio between the maximum deflection angle α in the device and the opening angle Θ of the SR

$$K = \frac{\alpha}{\Theta} = \frac{e\,\lambda_0\,B_0}{2\,\pi\,m_e\,c} = 0.934 \cdot \lambda_0[cm] \cdot B_0[T]\ , \tag{2.7}$$

where λ_0 is the period length and B_0 the peak value of the magnetic field. With respect to the parameter K, one can distinguish two basic types of insertion devices: wigglers and undulators.

Wigglers

A wiggler is characterized by a large period length and a high magnetic field ($K \gg 1$). Due to the large deflection angle α, the radiation of each wiggle adds up incoherently and the intensity from N magnetic periods is 2N times the intensity of a single bending magnet. A wiggler can be regarded as a set of stacked bending magnets and has therefore similar characteristics: a broad energy distribution and an emission in a relatively large solid angle.

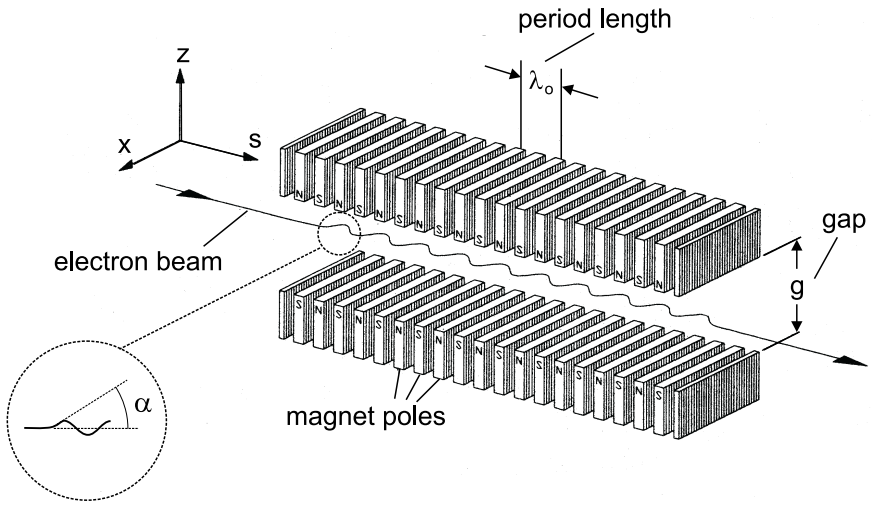

Figure 2.2: Schematic sketch of an insertion device, consisting of a magnetic array which deflects the electrons on a sinusoidal trajectory; modified after [Wil96].

Undulators

For undulators the parameter K is ≤ 1. The angle α is small and the radiation of successive periods adds up coherently. Interference leads to sharp peaks in the spectral brilliance at

$$\lambda_n = \frac{\lambda_0}{2n\gamma^2}\left(1+\frac{K^2}{2}+\gamma^2\phi^2\right) \quad n = 1,2,... \tag{2.8}$$

where ϕ is the angle to the undulator axis. The intensity is increased by a factor $(2N)^2$ and on the axis ($\phi = 0$) only the odd harmonics (n = 1,3,...) can be observed. The spectral width of the peaks depends on the number of periods N:

$$\frac{\Delta\lambda}{\lambda} \approx \frac{1}{nN}. \tag{2.9}$$

The energy position of the harmonics can be tuned by changing the gap between the magnetic poles. A reduction of the gap increases the magnetic field and the parameter K, and shifts the peaks to smaller energies. Table 2.1 shows the characteristics of the two undulators installed at the Nuclear Resonance Beamline ID18. Undulator 1 is used for nuclear scattering experiments with the ^{57}Fe resonance.

	Undulator 1	Undulator 2
period λ_0	2.28 cm	3.4 cm
magnetic field B_0	0.12 T	0.16 T
undulator parameter K	0.256	0.857
energy	14.4 keV	6..8/21.5..27 keV
power (100 mA)	0.05 kW	0.28 kW
source size (h x v)	812 x 54 μm^2	812 x 54 μm^2
divergence (h x v)	28 x 4 μrad	28 x 4 μrad
beam size @30 m (h x v)	1.8 x 0.6 mm^2	1.8 x 0.5 mm^2

Table 2.1: Characteristics of undulators at the Nuclear Resonance Beamline ID18 at ESRF [ESR97].

2.3 Properties of Synchrotron Radiation

The important properties of SR with respect to NRS experiments are summarized below:

- **time structure:**
  The energy loss of the particles in a storage ring is compensated in radio frequency cavities. Since only particles with the right phase relative to the radio frequency ν_{rf} are re-accelerated, they are grouped together in bunches. Depending on the operation mode at the ESRF storage ring (circumference l = 844 m, ν_{rf} = 352 MHz), the time window between two adjacent bunches (i.e. two radiation pulses) ranges from 2.8 μs (= l/c) with only one single bunch to 2.8 ns (= $1/\nu_{rf}$) for complete filling. The nuclear scattering experiments discussed in this thesis are mostly performed during 16-bunch-mode with a time window of 176 ns. The pulse duration is 20 ps for bending magnets and 100 ps for insertion devices [ESR92].

- **high brilliance:**
  The intense laser-like collimated beam of undulators results in short data accumulation times even in high pressure experiments, where only very small sample amounts (about 1μg at 100 GPa) are available.

- **polarization:**
  SR is 100% linearly polarized in the plane of the storage ring. This feature allows the excitation of certain nuclear sublevels in NRS, when the orientation of internal hyperfine fields is well defined (e.g. for a magnetic sample in an external magnetic field as discussed in chapter 3.2.5).

- **broad energy distribution:**
  The broad energy distribution of SR from the infrared to the hard x-ray region allows a wide range of energy tunability using appropriate undulators and monochromators. This tunability is essential for NRS experiments on two different energy scales. First, by variation over several keV, the resonance energies of many different nuclei can be provided. Second, the tunability in the meV range around a nuclear resonance has opened up the new spectroscopic branch of Nuclear Inelastic Scattering which enables the investigation of lattice dynamics.

Chapter 3

Nuclear Resonant Scattering

In this chapter a survey of Nuclear Resonant Scattering techniques is given, considering both elastic Nuclear Forward Scattering (NFS), the analogue of conventional Mössbauer Spectroscopy, and Nuclear Inelastic Scattering (NIS) for the study of lattice dynamics. We start with a few remarks on ^{57}Fe and classical Mössbauer Spectroscopy.

3.1 Fundamentals

3.1.1 The ^{57}Fe Nucleus

The probe for Nuclear Resonant Scattering (NRS) experiments in this thesis is the ^{57}Fe nucleus with a natural abundance of 2%. The nuclear level scheme is shown in figure 3.1.

The nuclear level with spin I = 3/2 has an excitation energy E_γ = 14.413 keV and a relatively long lifetime τ_0 of 141 ns. The transition to the ground state can proceed by

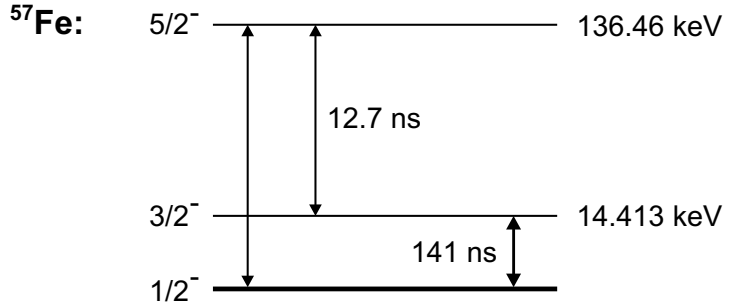

Figure 3.1: Energy level scheme for ^{57}Fe. The nuclear spin I is marked on the left, the energy relative to the ground state on the right.

the emission of a photon with energy E_γ or an internal conversion process, in which the excitation energy is transferred to a shell electron (mostly from the K-shell). Since E_γ is larger than the binding energy (7.11 keV for the K-shell), the electron is removed from the atomic shell and triggers a cascade of fluorescence radiation, mainly K_α with 6.4 keV and K_β with 7.1 keV (relative weight $K_\alpha/K_\beta \approx 7$ [Sco74]). The ratio of conversion processes to direct γ-transitions for ^{57}Fe is $\alpha = 8.2$. The linewidth Γ_0 of the transition is Γ_0 = 4.7 neV.

When built into a solid crystal, the nucleus interacts with its electric and magnetic surrounding. These *hyperfine interactions* lead to a shift and/or splitting of the nuclear levels. The type and size of hyperfine interactions yield information about structural and magnetic properties of the investigated sample (see e.g. [Gib76]).

The rest of the chapter will show that this information is obtained in very different ways, depending on the type of radiation source, which is used for excitation of the nuclear levels.

3.1.2 Mössbauer Spectroscopy

In conventional Mössbauer Spectroscopy (MS), nuclear levels are excited with radioactive sources, which emit a resonant photon with energy E_γ after a preceding nuclear decay. Since the transitions in source and absorber have approximately the same small linewidth Γ_0, a recoil during the emission and/or absorption process makes resonance fluorescence[1] impossible:

$$\text{recoil energy } E_R = p^2/2m = E_\gamma^2/2mc^2 \approx 2meV \gg \Gamma_0 \tag{3.1}$$

The effect of recoilless nuclear resonance fluorescence in solids was first discovered in ^{191}Ir by Rudolf Mössbauer [Mös58a]: if the nucleus is bound in a crystalline structure, the solid as a whole can take up the recoil momentum leading to a negligible recoil energy. The probability for such a process increases at lower temperatures and is given by the so-called Lamb-Mössbauer factor f_{LM}.

Soon after this discovery, it was shown that the *Mössbauer Effect* can provide a powerful spectroscopic tool [Mös58b]: based on an idea of Moon [Moo51], the relative velocity v between radioactive source and sample is varied inducing a Doppler shift $E_D = (v/c)E_\gamma$ between the corresponding resonance energies. A detector behind the sample measures the transmission as a function of the Doppler shift (see figure 3.2). The resulting energy spectrum gives information on the nuclear level splitting in the sample. For ^{57}Fe, with energy splittings smaller than 500 neV, the necessary peak velocities of 10 mm/s are easily accessible. The importance of iron in many scientific branches and the large Lamb-Mössbauer factor even at high temperatures ($f_{LM} \approx 0.8$

[1] Excitation of a nuclear level with a photon resulting from the de-excitation of a nuclear level of the same kind.

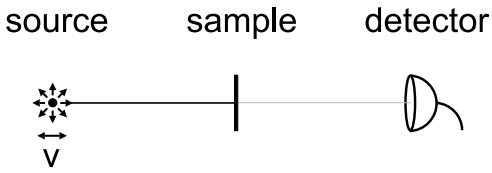

Figure 3.2: Principle of conventional Mössbauer spectroscopy.

at 300 K) have ensured that ^{57}Fe is the most commonly used isotope for MS. As an example, figure 3.3 shows the Mössbauer spectrum of α-iron at ambient conditions. The typical six line pattern is due to Zeeman splitting of the nuclear levels in a magnetic hyperfine field of 33 T.

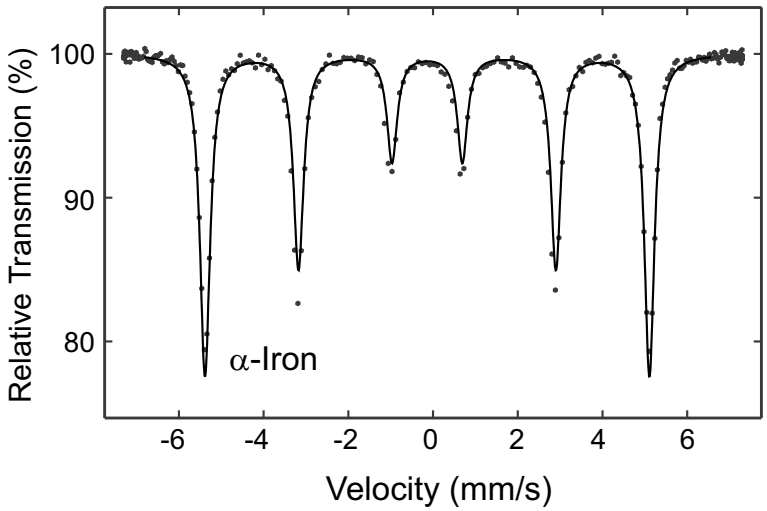

Figure 3.3: Conventional Mössbauer spectrum of α-iron at ambient conditions. The relative energy between source and absorber is given in mm/s (1 mm/s = 48 neV). The source was ^{57}Co in a rhodium matrix.

3.1.3 Excitation of Nuclei with Conventional X-ray Sources

The observation of nuclear resonance excitation with conventional (= non-radioactive) x-ray sources is extremely difficult. The reason is the large linewidth of such sources: even with a highly sophisticated crystal monochromator the linewidth of the excitation (≈ 1 *meV*) exceeds the width of the nuclear resonance by more than 5 orders-of-magnitude. A normal transmission experiment like in MS is impossible. The resonant absorption process can be verified only by the detection of the re-emitted photon. For the joint treatment of absorption and subsequent re-emission, the description shifts

to a scattering point of view, where the time constant of the scattering is determined by the lifetime τ_0 of the excited state. The Lamb-Mössbauer factor f_{LM} denotes the probability of elastic scattering without recoil.

Scattering Geometry

In a real scattering experiment, an ensemble of nuclei is involved, resulting in a superposition of different scattering responses. The scattering characteristics depend very much on the phase relationship between these different contributions. In the absence of a constant phase in space, one obtains *incoherent* scattering, which is randomly distributed in all directions (in 4π solid angle). This behaviour occurs e.g. in all inelastic scattering events, where the creation or annihilation of a phonon is involved. Internal conversion leads also to incoherent scattering. *Coherence* (= constant relative phase) between different nuclei is obtained for elastically scattered photons and the respective phase shift $\Delta\varphi$ depends on the spatial arrangement of the particles and the scattering geometry. The superposition leads to constructive interference for forward scattering ($\Delta\varphi = 0$) and for scattering from single crystals under a Bragg angle ($\Delta\varphi = n \cdot 2\pi$). In every other direction the scattering responses cancel out.

However, the detection of nuclear fluorescence radiation is extremely hampered by the huge amount of electronic non-resonant scattering, caused by the linewidth mismatch between source radiation and nuclear resonance. Two ways to solve this problem were proposed already in 1962 by Seppi and Boehm [SB62]:

- *"The use of a very intense x-ray source with improved energy resolution due to monochromatization with high-index reflections.*
- *The background problem might be solved by taking advantage of the instantaneous character of atomic (= non-resonant) scattering as compared to the relatively long lifetime of the nuclear excited states. Through the use of a pulsed X-ray beam and a properly gated detector it should be possible to observe only nuclear excitation events in the sample."*

The technical realization of these suggestions was far beyond the scope of that time. It was not until the beginning of the nineties that the combination of high-resolution monochromators ($\Delta E = 5\ meV$) and x-ray detectors with sufficient time resolution ($\approx$ 1 ns) and dynamic range (>10^5) led to the first observation of Nuclear Resonant Scattering in the forward direction [HSB91]. Before that, S. Ruby [Rub74] first proposed the use of synchrotron radiation for such experiments and E. Gerdau et al. [GRW85] had performed the first Nuclear Resonant Scattering experiments with SR under a Bragg angle. The Gerdau group used an electronically forbidden reflection of an Yttrium Iron Garnet single crystal to suppress the non-resonant scattering. However, the rapid development of NRS for hyperfine spectroscopy is connected with the

utilization of powder samples in forward scattering experiments. The special properties of SR open up a variety of new possibilities. For the extreme conditions of a high-pressure experiment, the high brilliance of synchrotron radiation is especially advantageous when compared to radioactive sources, which emit their radiation in 4π solid angle.

3.2 Nuclear Forward Scattering

The principle of NFS is presented in figure 3.4. In the 16-bunch mode at ESRF (see chapter 2) a synchrotron pulse of 100 ps length strikes the sample every 176 ns. The countrate after the high-resolution monochromator (HRM) is about 10^9 Hz in a bandwidth of 5 meV. A few ns after the excitation, when all electronic scattering processes (time constant 10^{-15} s) are completed, the detector starts to count nuclear resonant events as a function of time after excitation ($\approx$ 100 Hz).

For the hypothetical time spectrum of an isolated ^{57}Fe nucleus, a simple exponential decay $\propto \exp(-t/\tau_0)$ is expected with the lifetime τ_0 as time constant. This is indicated by the straight line in the logarithmic scale in figure 3.4. However, NFS of an ensemble of nuclei is a collective effect and the influence of coherence is reflected by a modulation of the time spectra.

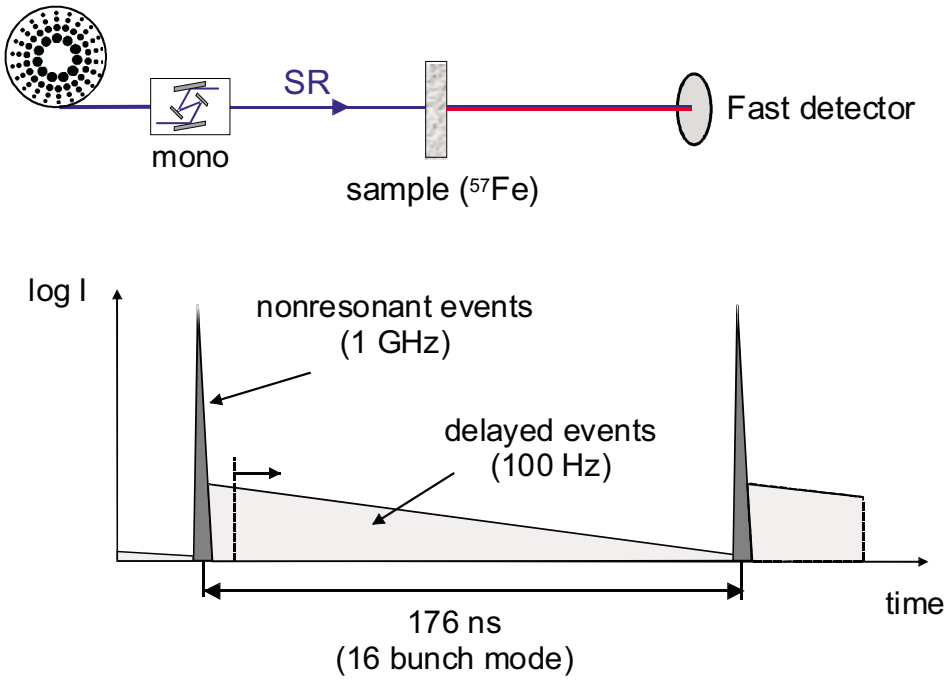

Figure 3.4: Principle of Nuclear Forward Scattering, showing the schematic set-up at the top and a simplified time spectrum at the bottom of the figure.

The two main coherence effects are (more details in sections 3.2.2 and 3.2.3):

- **Speed-up of the exponential decay:** With increasing number of ^{57}Fe nuclei, the probability for multiple scattering increases, resulting in a speed-up of the exponential decay.
- **Quantum beats:** In case of a hyperfine splitting of the nuclear levels, all possible transitions are excited by the broadband synchrotron pulse. The interference of the re-emitted radiation components with different resonance frequencies leads to beats in the time spectrum, which are determined by the level splitting.

3.2.1 Mathematical Treatment

The interaction of radiation with matter can be treated very generally with the concept of a complex index of refraction $\tilde{n}(\omega)$. Considering the solution of the wave equation in a dispersive medium, the amplitude E_{tr} of an electromagnetic wave transmitted through such a medium of thickness d is related to the incident wave E_i by

$$E_{tr}(\omega) = e^{-i\,\tilde{n}(\omega)\,k\,d}\,E_i(\omega), \tag{3.2}$$

where k is the wave vector in vacuum and ω the photon frequency. In case of a scalar index of refraction, $\tilde{n}(\omega)$ can be expressed by the nuclear scattering amplitude $f(\omega)$ for elastic nuclear scattering [Jac75]:

$$\tilde{n}(\omega) = \sqrt{1+\frac{4\pi}{k^2}\,\eta_s\,f(\omega)} \;\approx\; 1+\frac{2\pi}{k^2}\,\eta_s\,f(\omega). \tag{3.3}$$

Here η_s denotes the volume density of elastic scatterers and f the nuclear scattering amplitude. The approximation in equation 3.3 is valid in the x-ray region, because $\tilde{n}(\omega)$ differs not very much from 1. Analogously to the case of atomic scattering, the nuclear scattering amplitude f can be decomposed into a non-resonant Thomson term f_0 and a resonant contribution $f' + if''$ called *anomalous scattering* with real and imaginary part [HT94]. For nuclear scattering the Thomson term is proportional to Ze^2/m_pc^2, involving the large proton mass m_p; it is therefore negligible.

The resonant term for a single nuclear resonance is given by [Smi96]:

$$f(\omega) \;=\; -\frac{k}{8\pi}\,\sigma_0\,\frac{\Gamma_0}{\hbar(\omega-\omega_0)-i\,\Gamma_0/2} \tag{3.4}$$

$$\;=\; \underbrace{-\frac{k}{8\pi}\,\sigma_0\,\frac{x}{x^2+1/4}}_{f'} \;+\; i\;\underbrace{\frac{k}{8\pi}\,\sigma_0\,\frac{-1/2}{x^2+1/4}}_{f''} \tag{3.5}$$

$$\text{with}\quad x \;=\; \frac{\hbar(\omega-\omega_0)}{\Gamma_0},\quad \sigma_0 = \frac{2\pi}{k^2}\,\frac{1}{(1+\alpha)}\,\frac{2I_e+1}{2I_g+1}\;.$$

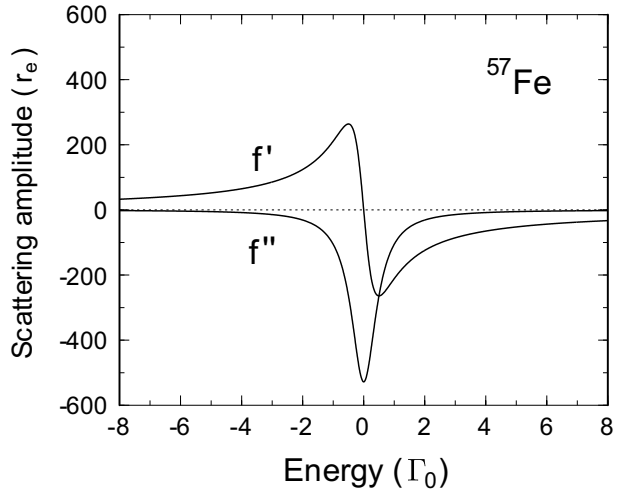

Figure 3.5: Real f' and imaginary f'' part of the nuclear scattering amplitude for ^{57}Fe in units of the classical electron radius $r_e = 2.82 \cdot 10^{-15} m$. For the graph, f_{LM} is taken as unity.

The maximum resonance cross section σ_0 contains the conversion coefficient α and the nuclear spins I_g and I_e of the ground and excited states, respectively. Since the resonant wave length (≈ 1 Å) is large compared with the size of the nuclei, the angular dependence of the nuclear scattering amplitude is very weak. Hence, we can take f in equation 3.4 as the forward scattering amplitude with a very sharp frequency dependence. Combining equations 3.2 and 3.3, the transmitted wave E_{tr} can be written as[2]

$$E_{tr}(\omega) = \exp(-ikd)\,\exp(-i\lambda\eta_s d\, f(\omega))\, E_i(\omega) \tag{3.6}$$

$$= \exp(-ikd)\,\underbrace{\exp(-i\lambda\eta_s d\, f'(\omega))}_{\text{phase shift}}\,\underbrace{\exp(\lambda\eta_s d\, f''(\omega))}_{\text{attenuation}}\, E_i(\omega). \tag{3.7}$$

The first exponential term on the right-hand side accounts for the phase shift of the unperturbed wave after travelling the distance d. Modifications of the incident wave are due to forward scattering: while the real part f' of the scattering amplitude causes a frequency dependent phase shift, the imaginary part f'' determines the attenuation. Figure 3.5 shows f' and f'' in units of the classical electron radius r_e.

Exactly at resonance, the attenuation reaches a maximum whereas the phase shift is zero. The maximum values of f' and f'' are almost two orders-of-magnitude larger than the electronic scattering factor, which can be estimated as $Z \cdot r_e$ with $Z = 26$ for the number of electrons in an iron atom. Far off resonance, f' drops in value according to E^{-1} and is large in comparison to f'', which drops according to E^{-2}.

[2]Here and in the following equations for E_{tr}, the electronic attenuation term $\exp(-\mu_e d/2)$ is omitted for clarity, because it shows no time or frequency dependence in the investigated energy band.

So far, we treated only the transmitted wave amplitude $E_{tr}(\omega)$. The finally measured physical quantity is the transmitted intensity I_{tr}. As mentioned in chapter 3.1.2, conventional MS monitors the transmitted intensity for varying photon energies. This can be obtained from equation 3.7 by taking the square modulus:

$$I_{tr}(\omega) = |E_{tr}|^2 = \exp\left(2\,\lambda\,\eta_s\,d\,f''(\omega)\right) I_i(\omega) \tag{3.8}$$

$$= \exp\left(-\frac{\eta_s\,d\,\sigma_0\,f_{LM}/4}{x^2+1/4}\right) I_i(\omega) \tag{3.9}$$

$$= \exp\left(-\frac{\chi/4}{x^2+1/4}\right) I_i(\omega) \tag{3.10}$$

$$\text{with} \quad \chi = \eta_s\,d\,\sigma_0\,f_{LM} \tag{3.11}$$

χ is called *effective thickness*. Exactly at resonance ($x = 0$) the transmitted intensity is $I_{tr}(\omega_0) = \exp(-\chi)\,I_i(\omega_0)$. [3] The information about the real part of the scattering amplitude is lost in a conventional Mössbauer experiment. An increasing thickness χ broadens the Lorentzian shape (given for $\chi < 1$ using the approximation $\exp(z) \approx (1+z)$) of an absorption line to a more complicated shape[4] according to equation 3.10. In the presence of several nuclear resonances due to hyperfine splittings, the overall absorption is obtained from the superposition of the absorption effects of the single resonances considering the respective transition intensities.

The effect of a large effective thickness χ and a multiple nuclear resonance on the NFS spectra will be discussed in the next two sections.

3.2.2 Speed-up of the Exponential Decay

In a NFS experiment the incident radiation is a short synchrotron radiation pulse, which has a uniform amplitude distribution within the energy band selected by the HRM: $E_i(\omega,t) = E_0 \cdot \exp(i\,\omega t)$. We get the frequency-dependent transmitted wave by inserting this relation into equation 3.7 and substituting χ from equation 3.11:

$$E_{tr}(\omega) = E_0\,\exp\left(i\,(\omega t - k\,d)\right) \exp\left(i\,\frac{x\chi/4}{x^2+1/4}\right) \exp\left(-\frac{\chi/8}{x^2+1/4}\right) \tag{3.12}$$

$$= E_i(\omega) + E_{fs}(\omega) \tag{3.13}$$

[3] The definition of χ in equation 3.11 is commonly used in conventional MS and has its origin in this relation. In the literature on NFS (e.g. [HSB91], [BSH92]), the effective thickness is defined as $\chi/4$, which gives a simpler presentation of most of the formulas on NFS as we will see later in equation 3.12. However, the priority is on the side of MS and for easier comparison we will use the introduced definition 3.11 for both spectroscopies.

[4] The actually measured transmission spectrum in MS arises from the folding with the line shape of the source.

The transmitted wave E_{tr} can be regarded as a superposition of the incident wave E_i and the forward scattered wave E_{fs}. However, in the frequency domain these two components can not be decomposed experimentally. To obtain the time-dependent representation of E_{tr} we have to integrate over all frequency components in equation 3.12. From a mathematical point of view this is a complex Fourier transformation. The result can be expressed in the form [KAK79]

$$E_{tr}(\tau) \propto \left[\Delta(\tau) - \exp\left(i\,\omega_0\,\tau\,\tau_0 - \frac{\tau}{2} \right) \frac{\chi}{2} \frac{J_1(\sqrt{\chi\,\tau})}{\sqrt{\chi\,\tau}} \right], \tag{3.14}$$

where τ is the time in units of the nuclear lifetime τ_0 and J_1 is the first-order Bessel function. The influence of the incident amplitude E_i is reflected by the δ-function at $\tau = 0$ which can be separated from the delayed nuclear scattering at $\tau > 0$. Taking the square of the modulus leads to the time dependent intensity (for $\tau > 0$):

$$I_{tr}(\tau) \propto \exp(-\tau)\,\frac{\chi}{\tau}\,J_1^2(\sqrt{\chi\,\tau}). \tag{3.15}$$

For thin samples with small χ or during a short time after excitation, this expression can be approximated by [BSH92]

$$I_{tr}(\tau) \propto \chi^2 \exp[\,-(1+\chi/4)\,\tau\,]. \tag{3.16}$$

This equation describes an exponential decay with an accelerated decay rate $(1+\chi/4)$, which leads to the so-called *speed-up* (see figure 3.6). Whereas the absorption effect in conventional MS increases with χ (see equation 3.10), the time-dependent NFS intensity for thin samples is proportional to χ^2. This enhanced sensitivity of nuclear

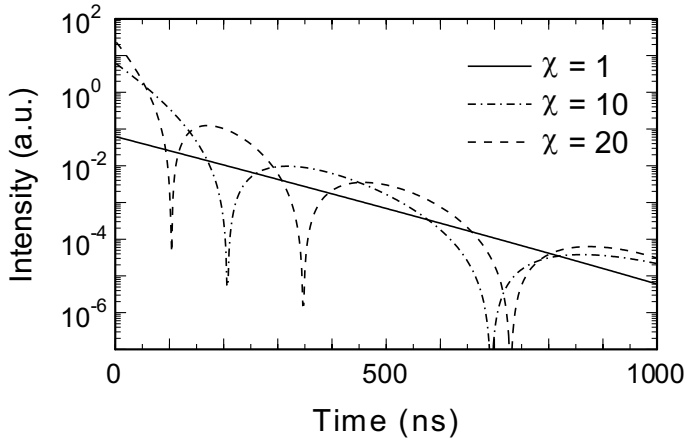

Figure 3.6: Calculated NFS spectra for different sample thickness according to equation 3.15. The thin sample with $\chi = 1$ gives an exponential decay represented by a straight line in a logarithmic scale. For sample thicknesses of $\chi = 10$ and $\chi = 20$ dynamical beat modulations are visible, with the first minimum shifted to earlier times for $\chi = 20$.

scattering was shown experimentally in investigations of surface structures containing down to one monolayer of ^{57}Fe [NMR98].

For thick samples, equation 3.16 is not a valid approximation and the time dependence shows beat modulations according to the Bessel function with larger separation of the minima at later times.

The exact positions of the minima are determined by the zero points of $J_1(\sqrt{\chi\tau})$ and the first minimum t_1 is related to the effective thickness χ by

$$\sqrt{\chi t_1/\tau_0} \approx 3.8 \;\Rightarrow\; t_1 \cdot \chi \approx 2040\,\text{ns} \tag{3.17}$$

3.2.3 Quantum Beats

So far, we have considered a single resonance line with degenerated nuclear levels. In the presence of hyperfine interactions, the degeneracy is removed and several nuclear resonances can occur. According to the type of nuclear transition (M1 for ^{57}Fe) the particular transitions have different polarization properties and the nuclear scattering amplitude must be written in matrix form [Smi96]:

$$\left[f_{s,s'}(\omega)\right]_{s,s'} = \text{const.} \cdot \sum_j \frac{\Gamma_0}{\hbar(\omega-\omega_{0,j}) - i\,\Gamma_0/2}\, G^2(m_g, m_e, j)\, P_{s,s'}(j) \tag{3.18}$$

where $\omega_{0,j}$ denotes the resonance frequency of transition j. The square of the Clebsch-Gordon coefficients G provides the probability of the respective transition which depends on the magnetic quantum numbers m_g and m_e of the ground and excited states. $P_{s,s'}$ is the polarization factor for the polarization state of incident radiation (s) and forward scattered radiation (s'). As shown by U. Bergmann, the formalism with a complex index of refraction (see equations 3.2 and 3.3) can be extended to scattering amplitudes in matrix form [Ber94].

In the following the simplified case of two resonance lines with the same probability and polarization is discussed. When the energy separation $\Delta E_{hf} = \hbar\Delta\omega$ between the two lines is large compared to their effective width, the resulting time spectrum is well approximated by multiplying the single-line pattern by a cos^2 term representing the interference of the two lines [Smi96]:

$$I_{tr}(t) \propto \exp(-\tau)\,\frac{\chi}{\tau}\, J_1^2(\sqrt{0.5\cdot\chi\tau})\, \cos^2\left(\frac{\Delta\omega}{2}t + \frac{\chi\,\Gamma_0}{8\,\Delta E}\right) \tag{3.19}$$

The first term in the argument of cos^2 describes the *quantum beat* modulation determined by the line splitting. The beating period T_{qb} is given by

$$T_{qb} = \frac{2\pi}{\Delta\omega} = \frac{880\,\text{ns}}{\Delta E_{hf}[\Gamma_0]} = \frac{86\,\text{ns}}{\Delta E_{hf}[mm/s]} \tag{3.20}$$

The second term in the argument of $\cos^2$ reflects the influence of the interaction between the two transitions. It depends on χ and ΔE_{hf}, and causes a small shift Δt_{qb} of the quantum beats to shorter times:

$$\Delta t_{qb} = \frac{\chi}{(\Delta E_{hf}\,[\Gamma_0])^2} \cdot 35\,\mathrm{ns} = \frac{\chi}{(\Delta E_{hf}\,[mm/s])^2} \cdot 0.34\,\mathrm{ns} \qquad (3.21)$$

According to equation 3.19 the resulting time spectrum for the two-line case is a multiplicative combination of Bessel beats and quantum beats. The Bessel beat modulation for this case is the same as for the single-line case if the sample is twice as thick (i.e. when it has the same effective thickness per resonance line). This is demonstrated in figure 3.7, where the time spectrum of a single resonance with $\chi = 10$ forms the envelope of a quantum beat pattern originating from a splitting of 1 mm/s and $\chi = 20$. The first half period is shortened by 6.8 ns, the time shift given in equation 3.21 for $\chi = 20$.

As the effective thickness gets larger, the approximation 3.19 fails due to the increasing overlap between the tails of the two lines, causing the lines to become strongly asymmetric [BSH92]. In this regime, the NFS spectrum can be calculated by numerical computation of the Fourier transform of equation 3.7 using the modified nuclear scattering factor of equation 3.18.

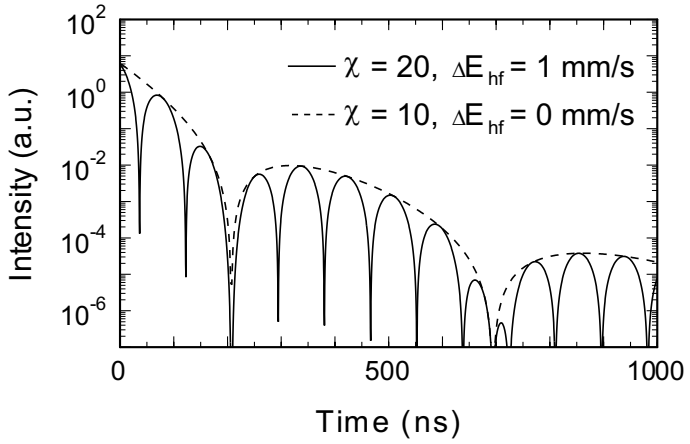

Figure 3.7: Calculated NFS spectrum for a hyperfine splitting of ΔE_{hf} = 1 mm/s (solid line) and $\chi = 20$ according to equation 3.19. The period of the quantum beat modulation is 86 ns. The dashed line indicates the spectrum for the single-line case with $\chi = 10$.

3.2.4 Coherence

As seen in the last section, the interference of two (or more) different nuclear scattering amplitudes A and B can lead to quantum beat modulations in the forward scattered intensity

$$I = A^2 + B^2 + 2AB\cos(\Delta\omega t - \Delta\varphi) \; . \tag{3.22}$$

However, modulations of the time spectra due to interference effects occur only if the scattering components have a constant phase difference $\Delta\varphi$ in time and space (*temporal and spatial coherence*). Otherwise the interference term cancels out and I is just the sum of the two intensities A^2 and B^2.

The requirement for temporal coherence is fulfilled, when the width of the SR pulse t_{SR} is small compared to both the lifetime τ_0 of the excited state and the beat period T_{qb}. This yields a well-defined time zero for all excitation processes. Both conditions are fulfilled for ^{57}Fe ($t_{SR} \approx 100\,ps, \tau_0 = 141\,ns, \Delta E_{hf} < 10\,mm/s \;\Rightarrow\; T_{qb} > 8\,ns$). If two hyperfine transitions belong to the same single nucleus with a split excited state, spatial coherence is not necessary and temporal coherence alone can result in beat modulations. The observation of such *single-nucleus quantum beats* in NFS was first reported by [BCR96]. It gives information on the excited-state splitting only and does not require recoilless scattering.[5]

However, the full information about both excited and ground state splittings can be extracted only if the interference of transitions from different nuclei is included. This requires spatial coherence of an ensemble of nuclei and therefore elastic (recoilless) scattering. Depending on the kind of separation of elastic scatterers parallel *or* perpendicular to the beam propagation direction, one can distinguish between longitudinal and transverse coherence, respectively.

longitudinal coherence:
In NFS the phase shift between two scatterers, lying "behind each other" in the beam propagation direction, is zero: the geometrical phase difference kx, due to their distance x, is compensated by the temporal phase ωt, caused by the time t, the wave field needs to propagate between the two scatterers in vacuum: $\omega t = kct = kx$.

transverse coherence:
When two scatterers are separated perpendicular to the beam direction, a geometrical phase difference $\Delta\varphi$ has to be considered. It is determined by the length difference Δl between the scattering paths from a source point z_s to a detector point z_d, as shown in figure 3.8. Since the phase difference $\Delta\varphi = k\Delta l$ varies for different detector and source points, the integration over the full source and detector size leads to a blurring of a

[5] Quantum beats following the excitation of single nuclei are well known from time-dependent perturbed angular correlation (TDPAC) experiments [SH72]. In TDPAC the nuclear sublevels are populated by the decay of a radioactive parent state. The beats are then measured with a time reference set by observing the gamma photon from the parent state decay.

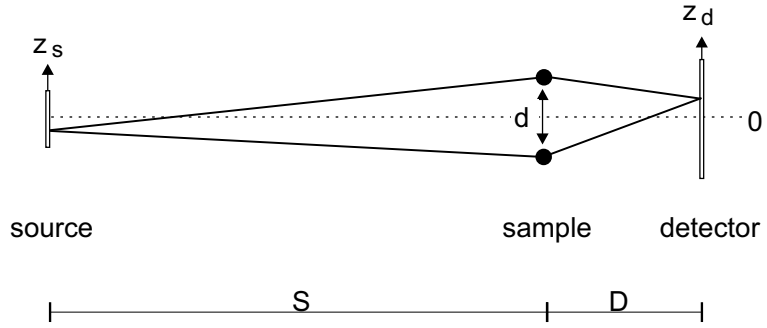

Figure 3.8: Measuring geometry and transverse coherence for an example of two scatterers, separated by a distance d.

quantum beat pattern. When the phase differences involved are larger than $\approx \pi$, the beat pattern vanishes and the two scattering components add incoherently. Extending this discussion, Baron et al. [BCG96, Bar99] calculated the phase differences for a Gaussian distribution of source size (σ_0) and detector size (σ_d). They defined an effective transverse coherence length L_{tr} as the minimum transverse separation between parts of the sample necessary to ensure that their responses add incoherently:

$$L_{tr} = \frac{\lambda}{2\pi}\,\frac{1}{\sigma_t} \quad ; \quad \sigma_t^2 \;=\; \left(\frac{\sigma_0}{S}\right)^2 + \left(\frac{\sigma_d}{D}\right)^2 \tag{3.23}$$

For a typical experiment at ESRF with $S = 40\,m$, $D = 1\,m$, $\sigma_0 = 50\,\mu m$ and $\sigma_d = 0.5\,mm$ the value of L_{tr} is dominated by the effect of a finite detector size:

$$\sigma_0 \;=\; 50\,\mu m,\ \sigma_d \;=\; 0 \qquad \rightarrow \quad L_{tr,source} \approx 10\,\mu m \quad \text{source effect}$$

$$\sigma_0 \;=\; 50\,\mu m,\ \sigma_d \;=\; 0.5\,mm \;\rightarrow \quad L_{tr} \approx 30\,nm \quad \text{total effect}$$

The value given for the pure source effect is calculated for the ideal case of a point detector ($\sigma_d = 0$) on the optical axis.

Summarizing the effects of longitudinal and transverse coherence on the NFS spectra, it should be mentioned that coherent and incoherent superpositions of scattering components can not be distinguished for completely homogenous samples. Inhomogeneities lead to a noticeable incoherent superposition, when parts of the sample with a certain property (say "blue") are as large as the sample thickness in the beam direction and separated from regions with property "red" by more than L_{tr} perpendicular to the beam. An example for such an inhomogeneity was observed for metallic iron under pressure. In the transition region of the $\alpha - \varepsilon$ phase transformation, the two crystallographic phases are spatially separated and produce a complex mixture of coherent and incoherent behaviour [Grü97]. Incoherent superposition is also obtained for thickness distributions in powder samples. Here the thickness varies on a length scale compara-

ble to the grain size which is usually in the range of μm and therefore much larger than L_{tr}. The effect of these distributions on the NFS spectra is discussed in more detail in chapter 5.2.3.

3.2.5 Examples

Figure 3.9 presents NFS spectra of non-magnetic stainless steel and magnetic iron, the latter measured without and with an external polarizing field of 0.6 T. The three spectra serve as a finger print for different magnetic states of iron atoms. For comparison, the corresponding conventional Mössbauer spectra are shown in the right panel.

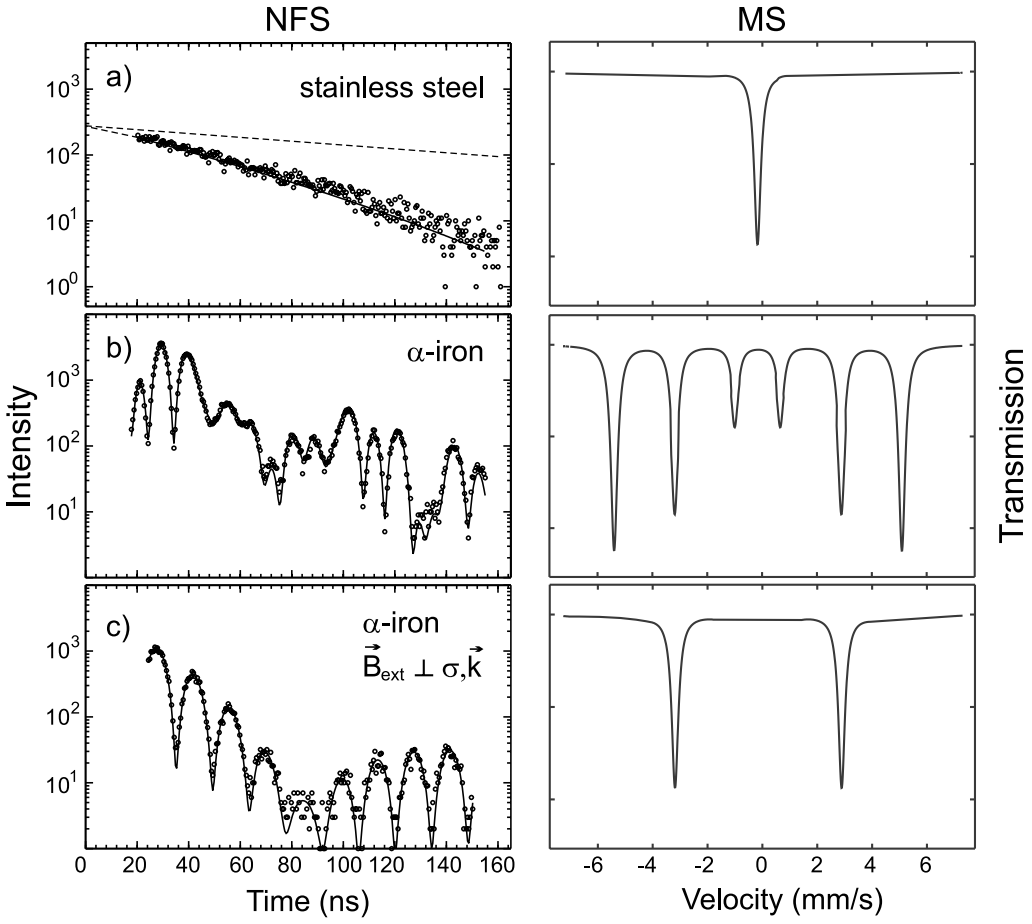

Figure 3.9: The left panel presents NFS spectra of (a) non-magnetic stainless steel ($\chi \approx 5$) and (b,c) magnetic α-iron ($\chi \approx 50$). The dashed line in (a) indicates the natural decay $\propto \exp(-t/\tau_0)$. Part (c) shows the time spectrum for a totally polarized iron foil in an external field perpendicular to the σ-polarization and the direction of the incoming beam. The corresponding Mössbauer spectra (schematic) are shown in the right panel. The solid lines are fits made with the CONUSS program package [SG94].

The time spectrum of the non-magnetic sample in figure 3.9a shows a straight line which indicates a simple exponential decay. It is modified by thickness effects, resulting in a speed-up of the collective nuclear decay compared to the natural decay (dashed line). For magnetic α-iron with random orientation of the quantization axis, all 6 possible transitions between the 3/2 excited and 1/2 ground state are excited by the broadband (meV) SR pulse. The corresponding decay spectrum in figure 3.9b shows a complex modulation, arising from the superposition of all transition frequencies. It is dominated by the beating of the two intense outer transition lines with an energy difference of 10.7 mm/s (110 Γ_0), corresponding to $T_{qb} = 8\,ns$.

The complex time spectrum of a non-polarized sample can be simplified, when the polarization of the SR is exploited to select certain transition lines in a magnetically aligned absorber. For the nuclear M1 transition in ^{57}Fe the polarization dependence corresponds to a classical dipole oscillator: a linear magnetic dipole oscillation along the quantization axis for $\Delta m = 0$ transitions and a right hand / left hand circular oscillation about the quantization axis for $\Delta m = +1$ / $\Delta m = -1$ transitions (see figure 3.10). For the iron sample measured in figure 3.9c the axis of magnetization is parallel to the $\vec{B}$ vector of the incident SR, and only the two Δm = 0 transitions of the ^{57}Fe resonance contribute to the NFS spectrum. The magnetic hyperfine field can be determined with high accuracy from the periodic sequence of beats (here $B_{hf} = 33\,T$, ΔE = 6 mm/s and $T_{qb} \approx$ 14 ns), modified only by thickness effects (χ = 25/line), resulting in the present case in a Bessel minimum at 85 ns. Since in the case of the magnetically polarized absorber, the two Δm = 0 transitions belong to different ground and excited states (i.e. different nuclei), the beating in the NFS spectrum demonstrates the spatial coherence of the NFS process.

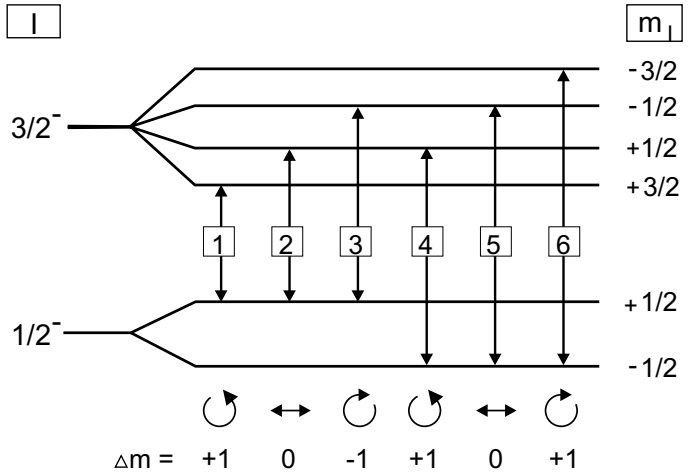

Figure 3.10: M1 transition scheme of ^{57}Fe in the presence of a magnetic field acting on the nucleus. The polarization properties for emission along the quantization axis are marked below. For emission perpendicular to the quantization axis, the $\Delta m = \pm 1$ transitions show linear polarization.

3.2.6 Measurement of Isomer Shifts

It is obvious from the previous sections that only frequency differences can be measured with NFS. In contrast to a conventional Mössbauer source, the SR provides no reference energy, relative to which the center of gravity of a transition line pattern can be determined. However, information about the isomer shift can be obtained with NFS, when an additional reference sample is placed in the beam. In this case, the nuclear scattered photons of reference and investigated sample can interfere and the energy difference of the two components can be extracted from the resulting beat pattern. Consequently, the isomer shift is given relative to the employed reference sample. In order to get simple beat patterns, a reference sample with a single-line transition should be used.

An application of this method using the ^{151}Eu resonance (21.5 keV) is presented in [PLS99] for a pressure-induced valence transition in $EuNi_2Ge_2$.

3.3 Nuclear Inelastic Scattering

In the previous sections we focused on elastic (=recoil-free) scattering of resonant photons ($E = E_\gamma$) by an ensemble of nuclei. The corresponding probability was given by the Lamb-Mössbauer factor f_{LM}. Incident photons with $E \neq E_\gamma$ were only treated with respect to the non-resonant background they produce. However, Nuclear Resonant Scattering is also possible for incident photons with $E \neq E_\gamma$; in this case the interaction necessarily involves the recoil of a ^{57}Fe nucleus with energy transfer from or to the crystal lattice in order to fulfil the resonance condition. This inelastic fraction of nuclear scattering, which was considered as the *lost* part (1 - f_{LM}) in conventional MS and also in NFS, turned out to be the basis of a new spectroscopic tool for the study of lattice dynamics.

The necessary condition for this new pathway is the energy-tunability of SR, which gives the possibility to measure the energy dependence of Nuclear Inelastic Scattering (NIS) over an energy range of ± 100 meV, which is covered by lattice vibrations. In contrast to other methods like inelastic neutron, x-ray and Raman scattering, NIS does not deal with phonon dispersion relations but, complementary to that, gives direct access to the density of phonon states (DOS). This topic will be discussed in the next two subsections.

3.3.1 Basic Features

The first NIS experiments were carried out in 1994 [SYK95, STA95]: The energy E of an incoming SR beam is tuned about ± 100 meV around a nuclear resonance monitoring the time-delayed inelastically scattered radiation. Since the inelastic scattering process is spatially incoherent, the scattered photons are emitted in 4π solid angle and can be detected perpendicular to the incident beam (inset of figure 3.11a). The measured intensity depends on the probability that the energy of a phonon matches the energy $E - E_\gamma$. The three main parts of a NIS spectrum are shown schematically in figure 3.11a. The central peak involves no energy transfer to the lattice and contains mostly fluorescence radiation after elastic absorption at $E = E_\gamma$. Photons with $E < E_\gamma$ can excite the nuclear resonance after annihilation of a phonon. The high-energy sideband for $E > E_\gamma$ corresponds to phonon creation. Figure 3.11b shows the energy spectrum of elastic nuclear scattering, which is measured in forward direction. Here, scattering appears only when the energy of incident radiation coincides with the energy of the nuclear transition. The obtained data provide the instrumental function of the high-resolution monochromator, because the width of the nuclear transition in this scale is negligible. Furthermore, the peak gives a precise reference for the energy position of the nuclear resonance.

As introduced in section 3.1.1 for ^{57}Fe, the scattered photons follow the de-excitation of the nuclei via two different channels: the radiative channel with $\sim$11% probabil-

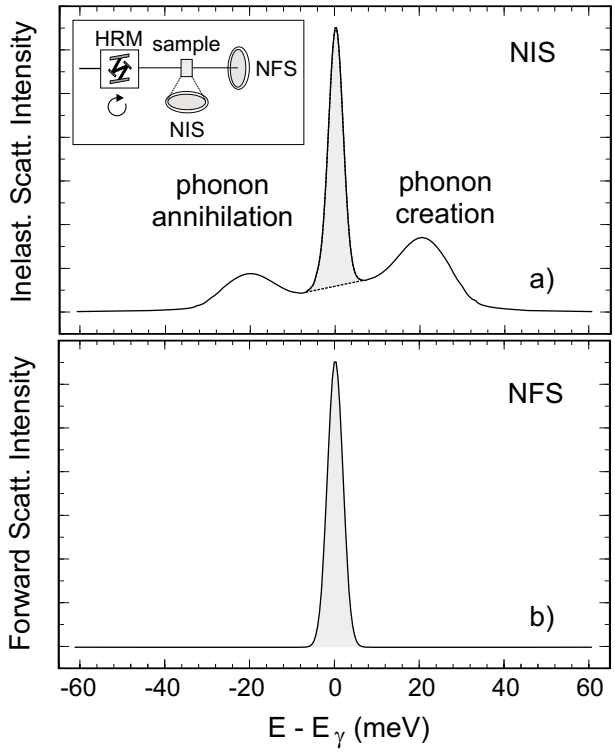

Figure 3.11: a) The inset sketches the measuring geometry for a scattering experiment, where a high-resolution monochromator (HRM) is tuned around the nuclear resonance. The scattered intensity in forward direction (NFS) and perpendicular to the incoming beam (NIS) is monitored as a function of energy relative to E_γ. The plot in a) displays a schematic NIS spectrum with elastic peak at $E = E_\gamma$ and energy sidebands corresponding to phonon creation for $E > E_\gamma$ and phonon annihilation for $E < E_\gamma$. b) shows the intensity of forward scattered radiation calculated for an instrumental function with Gaussian shape and 5 meV FWHM.

ity and the internal conversion channel with 89% probability. Thus, the dominating part of detected photons are products of internal conversion, mostly Fe-K_α x-rays with 6.4 keV. [6] Therefore, the allowed momentum transfer is not specified by the experimental set-up: The exact location of the detector relative to the incident beam does not matter, because the angular distribution of the atomic emission is an entirely atomic property and does not depend on the specific way of nuclear excitation. Phonons with any momentum, which is allowed by the dispersion relations for a particular energy transfer, contribute equally to NIS. Consequently, Nuclear Inelastic Scattering provides an ideal "momentum-integrated" tool for the study of lattice dynamics and does not require single crystalline samples.

[6] In practice, the relative amount of detected fluorescence radiation is even higher, since the detector efficiency is much better for 6.4 keV than for 14.4 keV (see section 4.1.2).

The properties of NIS can be summarized as follows:

- NIS provides direct access to the phonon DOS. In contrast to coherent inelastic neutron scattering [Squ78] no theoretical model has to be used (see also chapter 6.2). The experiments can be done with polycrystalline samples.

- NIS benefits from the large cross section of Nuclear Resonant Scattering, which is in the case of ^{57}Fe about five orders-of-magnitude larger than the relevant neutron cross section ($\sigma_{nuclear} = 2.56 \times 10^{-18}\,cm^2$ and $\sigma_{neutron} = 1.17 \times 10^{-23}\,cm^2$ [Squ78]). In combination with the small size of SR beams, this allows to study very tiny samples ($\leq$1mg).

- NIS has as an intrinsic energy reference. The phonon-related energy transfer is easily determined by the energy of the incident SR relative to the nuclear resonance. An energy analysis of the scattered particle is not necessary.

- Since NIS is only sensitive to lattice vibrations where resonant nuclei are involved, a partial phonon DOS of the sample is measured. This implies certain limitations to the class of accessible materials but leads on the other hand to the useful feature of isotope selectivity, which can simplify the data especially for large molecules [KAO97].

- The background problem of other inelastic scattering techniques can be largely overcome in NIS by the detection of time-delayed photons. Within the limit of the detector background (10 mHz), every detected photon originates from a nuclear scattering process. Like in NFS, this feature is especially valuable in high-pressure experiments.

The extraction of the phonon DOS is discussed in the next subsection following [STA95, CRB96, CS99].

3.3.2 Data Evaluation

The photons monitored in an NIS experiment follow a preceding nuclear absorption process. According to [STA95] the measured intensity $I(E)$ is proportional to the absorption probability $S(E)$ per unit of energy and to the effective number η_{eff} of ^{57}Fe nuclei in the sample[7]:

$$I(E) = const. \cdot \eta_{\text{eff}} \cdot S(E) \quad \text{with} \quad \int_{-\infty}^{\infty} S(E)dE = 1. \tag{3.24}$$

[7] In the following, the energy E is given relative to E_γ.

Assuming a quasi-harmonic lattice with well-defined phonon states, $S(E)$ can be expanded in terms of n-phonon contributions [STA95, SS60]:

$$S(E) = \underbrace{f_{LM}\,\delta(E)}_{S_{el}(E)} + \underbrace{f_{LM}\sum_{n=1}^{\infty} S_n(E)}_{S_{in}(E)}\,, \tag{3.25}$$

with the elastic part $S_{el}(E)$ and the inelastic part $S_{in}(E)$. The relative weight of the inelastic part is (1-f_{LM}). The phonon DOS $g(E)$ is proportional to the single-phonon term in the expansion 3.25 and the multiphonon contributions $S_n(E)$ for $n \geq 2$ are obtained by convolution of $S_{n-1}(E)$ with $S_1(E)$:

$$S_1(E) = \frac{E_R\, g(|E|)}{E\,(1-e^{-E/k_BT})}\,, \tag{3.26}$$

$$S_n(E) = \frac{1}{n}\int_{-\infty}^{\infty} S_{n-1}(E-\varepsilon)\,S_1(\varepsilon)\,d\varepsilon\,, \quad n \geq 2. \tag{3.27}$$

Since the ratio of the integrated n- and (n-1)-phonon terms is given by $-\ln f_{LM}/n$ [CR98], the multiphonon contribution ($n \geq 2$) for metallic iron with $f_{LM} \approx 0.8$ is less than 12% of the total inelastic part.

The different steps in the extraction of $g(E)$ from $I(E)$ are demonstrated in figure 3.12 for the example of a Debye-like DOS (see chapter 6.2.1). The Debye temperature Θ_D was taken as $420\,K$, resulting in a Lamb-Mössbauer factor of 0.8 at room temperature. The spectrometer resolution was included by convolution with a Gaussian of 5 meV FWHM.

1. In general, $S(E)$ can not be calculated from $I(E)$ by a normalization of equation 3.24, since the effective number of resonant nuclei η_{eff} is not constant over the measured energy range. The reason for this is the sharp increase in attenuation of the incident SR at the nuclear resonance. The nuclear part of the attenuation length for iron metal is $0.09\,\mu m$ at E_γ and 0.36 m in the sidebands of a NIS spectrum, whereas the electronic part is constantly $20\,\mu m$ [STA95]. Therefore, η_{eff} strongly decreases at E_γ and the ratio between the elastic peak and the remaining spectrum is not well-defined. A possibility to solve this normalization problem was provided by [STA95]. The procedure makes use of the general property of $S(E)$, that the first moment $\int S(E)\,E\,dE$ is equal to the recoil energy E_R of a free nucleus [Lip60, Lip95]. Since the damped elastic part of $I(E)$ is assumed to be symmetric around $E = 0$, it has no effect on the first moment and hence the inelastic (n-phonon) part of $I(E)$ can be normalized correctly ($\Rightarrow I_{\text{norm}}(E)$ in figure 3.12):

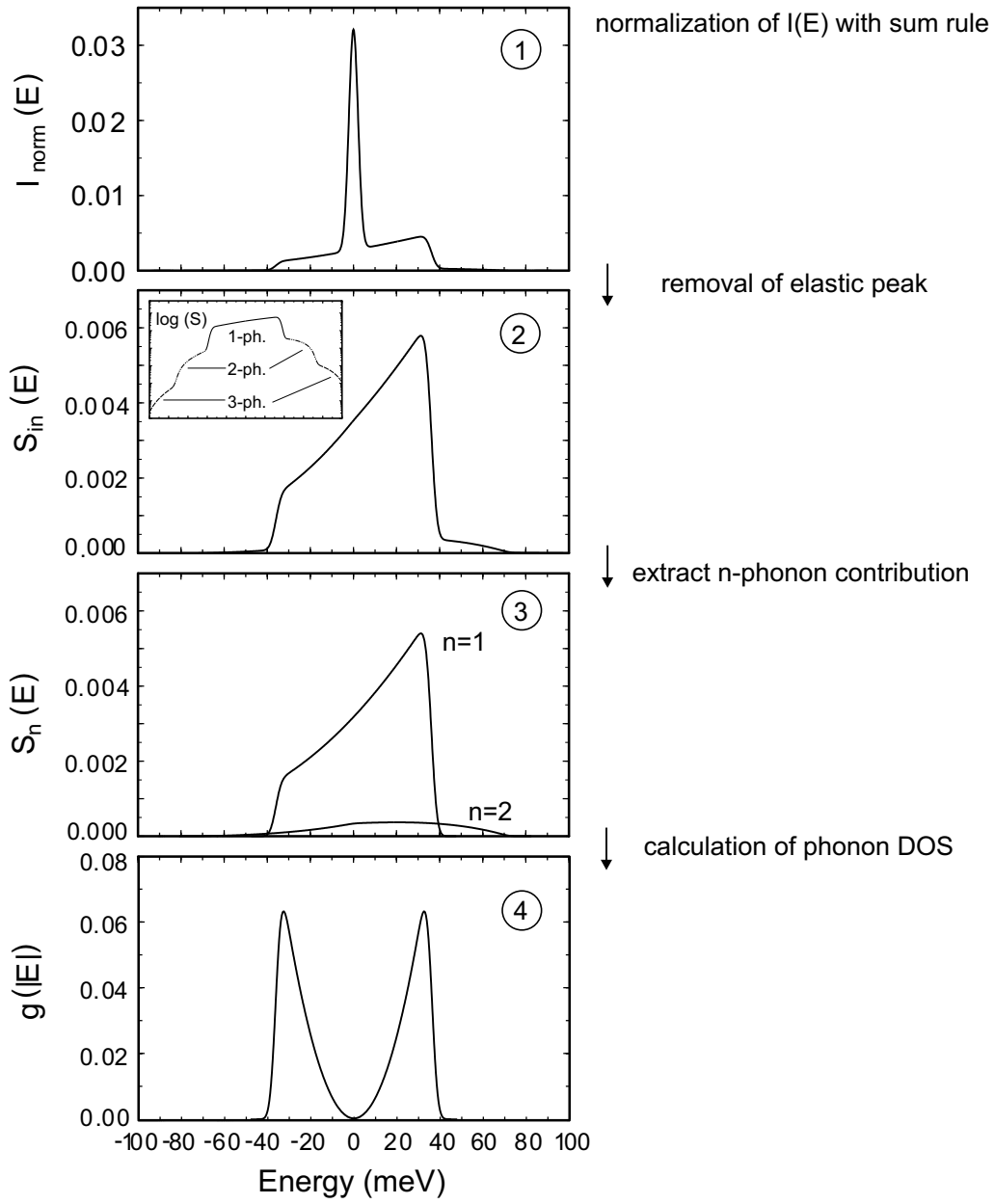

Figure 3.12: 1) Simulated NIS spectrum for an ideal Debye solid with $\Theta_D = 420\,K = 36\,meV/k_B$. The inelastic part is normalized using a sum rule of Lipkin [Lip60, Lip95]. 2) After removal of the elastic peak, the remaining inelastic part is the sum $\sum S_n(E)$ of single- and multi-phonon contributions. Integration of this spectrum gives $1 - f_{LM}$. 3) The multi-phonon contributions $S_n(E)$ for $n \geq 2$ can be separated by a recursive procedure according to equations (3.25) and (3.27). 4) The phonon DOS $g(|E|)$, convoluted with the Gaussian resolution function, can be extracted from $S_1(E)$ with equation (3.26).

$$
\begin{aligned}
\int_{-\infty}^{\infty} I(E)E\,dE &= const.\cdot \int_{-\infty}^{\infty} \eta_{\text{eff}}\, S(E)E\,dE \\
&= const.\cdot \left(\eta_{\text{eff}}^{el} \underbrace{\int_{-\infty}^{\infty} S_{el}(E)E\,dE}_{=0} + \eta_{\text{eff}}^{in} \underbrace{\int_{-\infty}^{\infty} S_{in}(E)E\,dE}_{=E_R} \right) \\
&= const.\cdot \eta_{\text{eff}}^{in} \cdot E_R \\
\Rightarrow \quad I_{\text{norm}}(E) &= \frac{E_R}{\int_{-\infty}^{\infty} I(E)E\,dE}\, I(E) \qquad (3.28)
\end{aligned}
$$

2. After adjusting and removing the elastic peak, the resulting spectrum is equivalent to the n-phonon part $S_{in}(E)$ of the absorption probability. The integration gives directly the recoil fraction $1 - f_{LM}$ (see equation 3.25). Consequently, f_{LM} can be determined without any knowledge about the number of ^{57}Fe nuclei in the sample. In conventional MS and NFS, the recoil-free fraction f_{LM} is contained in the effective thickness χ (see equation 3.11) and can be determined only with specific information about η_{eff}.

3. $S_{in}(E)$ is decomposed into the different n-phonon contributions $S_n(E)$ (n=1,2,...) with an iterative procedure [STA95], shown in the flow diagram in figure 3.13: the iteration is started with a first approximation $S_1' \approx S_{in}/f_{LM}$ using the value for f_{LM} from the above mentioned integration. Then S_2' is calculated with equation 3.27 and subtracted from S_1' to get the next approximation S_1''. This new S_1'' is used to calculate the contributions S_2'' and S_3''. For every further iteration step n, the subtraction of the multi-phonon terms $S_i^{(n-1)}$ from the initial approximation S_1' leads to a new set of $S^{(n)}$. This procedure has to be repeated until $S_{n+1}^{(n)}$ gets negligible small.

4. Finally, the phonon DOS $g(E)$ can be calculated from the obtained $S_1(E)$ with equation 3.26.

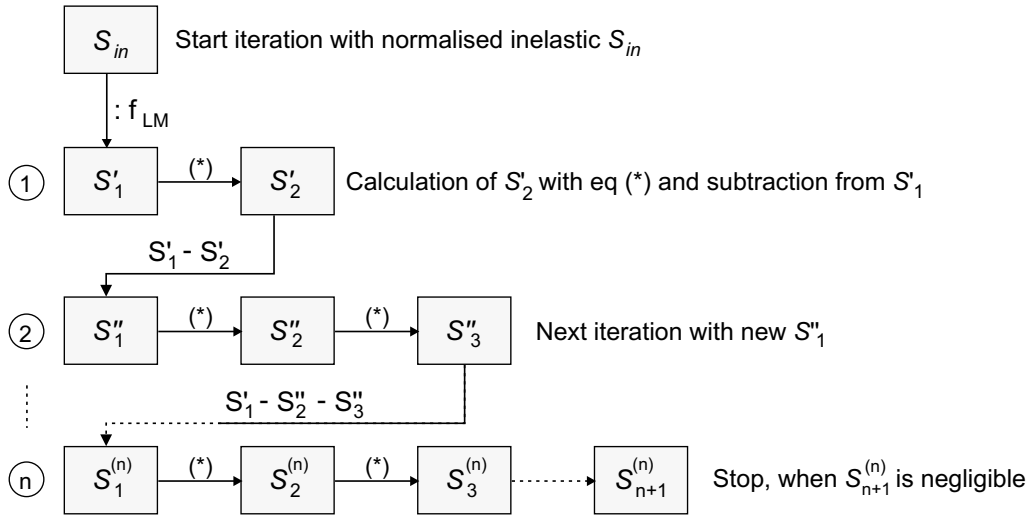

Figure 3.13: Flow diagram of the recursive procedure to extract the different multi-phonon contributions from the normalize inelastic spectrum S_{in}. The procedure is finished, when the last multi-phonon part $S_{n+1}^{(n)}$ becomes negligible. The "(*)" sign stands for the application of equation 3.27.

Using the Bose occupation factor $n_B(E,T) = 1/(\exp(E/k_B T) - 1)$, equation 3.26 for the single-phonon term $S_1(E)$ can be rewritten:

$$E < 0: \quad S_1(E) = E_R \frac{g(|E|)}{|E|} n_B(E,T) \qquad \text{phonon annihilation,} \quad (3.29)$$

$$E > 0: \quad S_1(E) = E_R \frac{g(|E|)}{|E|} (n_B(E,T)+1) \quad \text{phonon creation.} \quad (3.30)$$

Thus, the annihilation part of the NIS spectrum is proportional to the occupation of the phonon states $n_B(E,T)$ and vanishes at low temperatures. The creation part is proportional to $(n_B(E,T)+1)$ and remains finite even at $T = 0$ leading to a recoilless fraction $f_{LM}(T=0) \neq 1$. An incident x-ray photon can gain energy only from an existing phonon, whereas an energy loss is possible via two ways: increasing the energy of an existing phonon or creating a new one. The intensity ratio between the high- and low-energy sideband of an NIS spectrum is

$$\frac{n_B(E,T)+1}{n_B(E,T)} = e^{|E|/k_B T}. \quad (3.31)$$

Chapter 4

Experimental Details

This chapter presents some experimental and technical details about Nuclear Resonant Scattering under pressure. The first section introduces the Nuclear Resonance Beamline at ESRF including a short description of its main components. The second section gives a detailed presentation of the high-pressure technique, which was developed as a part of this thesis.

4.1 Nuclear Resonance Beamline at ESRF

The principle set-up of the Nuclear Resonance Beamline ID18 at ESRF is shown in figure 4.1. For experiments with the ^{57}Feresonance, the 6 GeV electron storage ring was operated in 16-bunch mode providing a time window of 176 ns between the bunches. The bunch purity, defined as the relative amount of photons from spurious bunches, is better than 10^{-9}. The synchrotron radiation (SR) from an undulator is tuned with its first harmonic to 14.4 keV. The radiation bandwidth of 300 eV is monochromatized by a high-heat-load Si(1 1 1) double crystal monochromator (PM) down to a bandwidth of 3 eV and then further to about 5 meV by a "nested" high-resolution monochromator (HRM, see subsection 4.1.1). During these monochromatization steps the total flux is reduced from 10^{14} Hz to about 10^{9} Hz. This beam was used to excite the 14.413 keV levels of the ^{57}Fe nuclei in the absorber, schematically shown in figure 4.1 within a diamond-anvil cell (DAC).

In a NFS experiment the detector, an avalanche photo diode (APD, see subsection 4.1.2) behind the sample measures the nuclear scattered intensity of SR as a function of time after excitation. The time-mode detection allows an easy discrimination against electronically scattered radiation, which exceeds the nuclear scattering by a factor of 10^{5} but occurs almost instantaneously within the width of the SR bunches (100 ps).

For a NIS experiment the HRM is tuned around the nuclear resonance monitoring the intensity of Fe-K_α x-ray fluorescence (6.4 keV) following the de-excitation of nu-

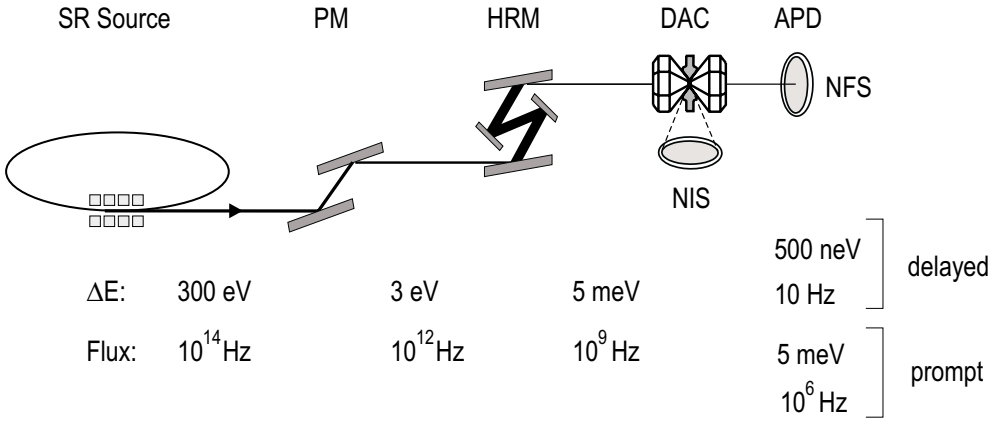

Figure 4.1: Schematic set-up of the Nuclear Resonance Beamline ID18 at ESRF. SR source with storage ring and undulator, PM: pre-monochromator, HRM: high-resolution monochromator, DAC: diamond-anvil cell, APD: avalanche photo diode as fast detector for NFS and NIS. The corresponding energy bands and estimated SR flux are denoted below. Downstream of the sample these specifications are given separately for prompt and delayed (i.e. nuclear scattered) photons.

clei after internal conversion. The corresponding APD is placed perpendicular to the incident beam and close to the sample in order to cover a large solid angle. After feasibility studies with NIS under high pressure at the Nuclear Resonance Beamline ID18, the data with highest quality was obtained at the ESRF beamline ID22. This beamline can be used as a second station for nuclear scattering experiments since 1998.[1] The principle set-up is the same as at ID18 in figure 4.1. During our experiments at ID22, a second 1.5 m undulator was operated at 14.4 keV. However, the main step from the stage of feasibility studies to accurate measurements on a 0.5 μg sample up to 42 GPa was made possible by the use of focusing elements in the beamline optics to concentrate the incident flux on the small sample dimensions.

The key components of the set-up: the high-resolution monochromator, the fast detectors and the focusing elements are discussed in the next subsections.

[1]The operation of ID22 for nuclear scattering experiments is limited to periods with special timing modes like 16-bunch mode. For most time of the year it is used for experiments with micro-focusing, -imaging and -diffraction [ESR97].

4.1.1 High-Resolution Monochromator

The task of the HRM is to reduce the energy resolution of the incoming SR to a small bandwidth of $\sim$5 meV around the nuclear resonance. This can be achieved with a large Bragg angle Θ_B of a crystal reflection (h k l). According to Bragg's law

$$2\,d\,\sin\Theta_B \;=\; n\lambda\,, \tag{4.1}$$

a given variation $\Delta\Theta$ around a large value of Θ_B leads to a minimum variation $\Delta\lambda$ in energy. For $d \;=\; a\,/\,\sqrt{h^2+k^2+l^2}$ with silicon (a = 5.43 Å) and ^{57}Fe (λ = 0.86 Å), the largest possible value is $\Theta_B = 80.4^\circ$ for the Si(9 7 5) reflection. Usually, such high-index reflections have a small angular acceptance. This small acceptance can be adapted to the divergence of the incoming beam by an additional asymmetric reflection. The corresponding "nested" set-up of a HRM was first proposed by Ishikawa et al. [IYI92] and is shown in figure 4.2 for a HRM used at ESRF. The combination of two Si(9 7 5) and two Si(4 2 2) reflections leads to an energy resolution of 4.4 meV. A second nested HRM at ESRF is operated with the combination Si(12 2 2)/Si(4 2 2) and has an energy resolution of about 6.4 meV.

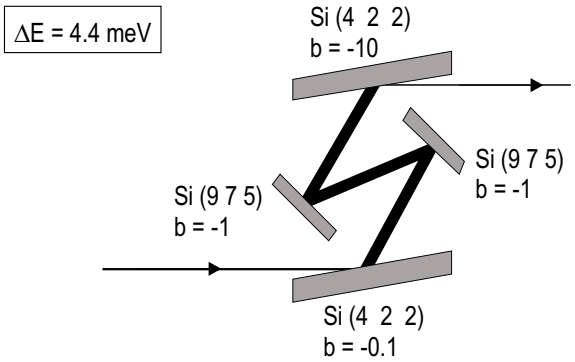

Figure 4.2: Set-up of a high-resolution monochromator with "nested" design. The two high-resolution Si (9 7 5) crystals are placed between two asymmetric Si(4 2 2) crystals, which adapt the emittance of the incident SR beam to the small angular acceptance of the inner crystals. The asymmetry parameter b is defined as $b = -\sin\Theta_{in}/\sin\Theta_{out}$ with the angle Θ_{in} (Θ_{out}) between the incoming (outgoing) beam and the crystal surface.

4.1.2 Fast Detectors

The detector system in a nuclear scattering experiment has to meet severe demands. Even with a HRM, the total flux in a high-pressure NFS experiment is in the MHz range, whereas the delayed count rate may be as low as 1 Hz or less. The detector needs to have a good time resolution (nanoseconds) and quantum efficiency, low noise and a high dynamic range. The first NFS measurements were performed with scintillating crystals [HSB91] but since 1994 silicon-based avalanche photodiodes (APD's) are

most commonly used. The reason for their success is the high dynamic range (>10^6) at very low background rates of 0.01 Hz. The time resolution is better than 1 ns. With an active area of $10x10\,mm^2$ the quantum efficiency is about 12% at 14.4 keV and 90% at 6.4 keV. More details can be found in [Kis91, BR94, Bar95].

4.1.3 Focusing Elements

The two kinds of focusing elements which were used for the NIS experiments are briefly discussed in the next two subsections. With the combined use of these elements a flux of 3×10^9 Hz on a spot size of $100\mu m \times 100\mu m$ was achieved.

Compound Refractive Lens (CRL)

In general, lenses for electromagnetic radiation in the x-ray regime ($E > 10$ keV) are difficult to realize, since the index of refraction $n = 1 - \delta$ for these energies varies not much from unity. Consequently, the achievable focal length f for a single refracting device is rather large. A new approach [SKS96] is to stack several single lenses to a so-called compound refractive lens (CRL) to obtain focal lengths in a reasonable range of 1-10 m. The principle set-up of a CRL is shown in figure 4.3. Since n is smaller than unity, one has to use a concave shape of the lens to obtain a focusing property.[2] For a single lens (upper part of the figure), the focal length is $f_1 = R/2\delta$, when R denotes the radius of curvature. For typical values of $R = 0.2$ mm and $\delta = 1.63 \times 10^{-6}$ (Be at 14.4 keV) the focal length is $f_1 \approx 60$ m. When N lenses are stacked behind each other (N=number of holes in the lower part of the figure), the focal length is reduced to $f_N = R/2\delta N$; a typical value is $f_{30} = 2\ m$ for $N = 30$.

Since the focusing of SR is equivalent to the imaging of a SR source, it is governed by the well-known Gaussian lens formula $1/f = 1/d_s + 1/d_i$, where d_s and d_i are the distances from the lens (focal length f) to the source and to the image, respectively. The geometrical demagnification $m = d_i/d_s$ is determined by d_s and f: $m = f/(d_s - f)$.

Besides the focal length, an important and inherent property of CRL's is the photoabsorption of SR by the lens material. Since CRL's with typical thicknesses in the order of mm show very high absorption, the use of a low-Z material is mandatory. Beryllium (Z=4) is the most often used material which has in addition appropriate mechanical properties for high-precision machining. The large spherical aberration in the above mentioned example of cylindrical holes is reduced in recent developments by the machining of holes with parabolic shape [Ric98b]. It should be mentioned that the presented CRL's lead only to focusing in one dimension. A two-dimensional focusing could be obtained with two crossed refractive lenses. However, the typical acceptance

[2] Or in a reciprocal view, one uses a convex lens of air as the refractive medium.

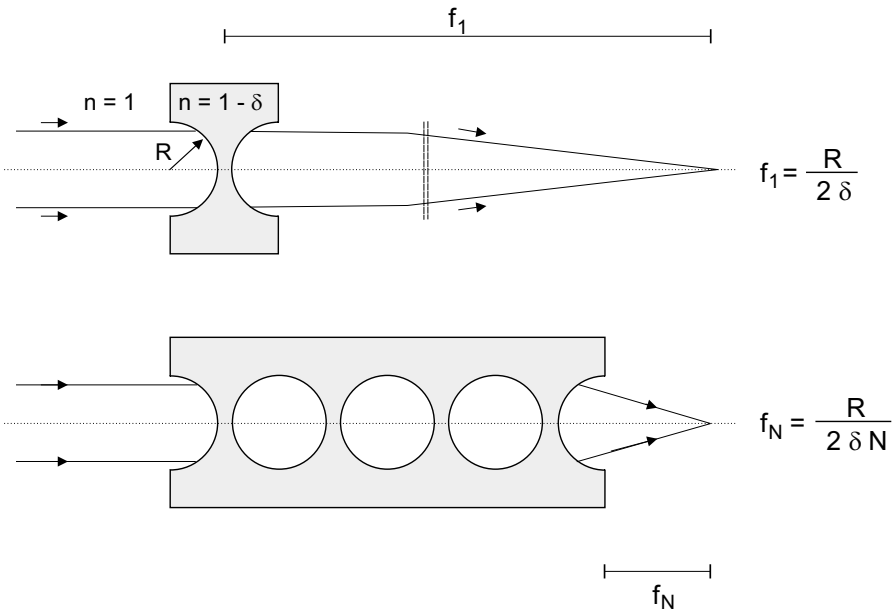

Figure 4.3: Schematic view of a compound refractive lens (CRL) for x-rays. The upper part shows the principle of a single concave lens with cylindrical shape, the radius of curvature R, the refractive index $1-\delta$ and the focal length f_1. The lower part shows the example of N stacked lenses with focal length f_N.

of a CRL (0.2 mm) is much smaller than the horizontal beam size (1 mm). For an optimal performance, a CRL for vertical focusing can be combined with a focusing monochromator for the horizontal direction.

Focusing Monochromator

The schematic set-up of a focusing monochromator (FM) is depicted in figure 4.4. Usually, a FM consists of a conventional Si(1 1 1) crystal (A) and a bent Si(1 1 1) crystal (B). Whereas the first crystal preserves the incident beam direction of the complete FM, the focusing property is due to the second crystal. For this purpose, the thin second crystal is mounted on a "U-shaped" profile, which can induce a well-defined curvature of the Si crystal by a spread of the two legs.

The relation between the bending radius R_b of the curved crystal and the focusing properties is given by [FCH98]

$$R_b \;=\; \frac{2\,d_s\,d_i\sin\Theta_B}{d_s+d_i} \;=\; \frac{2\,d_s\,m\sin\Theta_B}{1+m}\;, \tag{4.2}$$

where d_s, d_i and m are defined as above for CRL's; Θ_B is the Bragg angle.

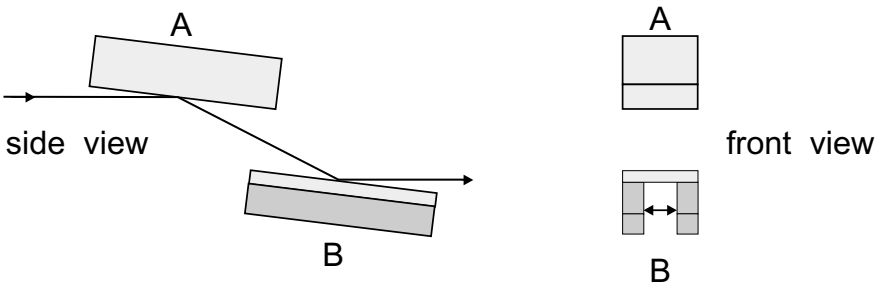

Figure 4.4: Schematic sketch of a focusing monochromator with a conventional Si crystal (A) and a bent Si crystal (B).

In practice, the minimum bending radius is determined by the fracture limit of the crystal material. For typical conditions of a nuclear scattering experiment with an incident energy of 14.4 keV, $\Theta_B = 7.88^\circ$, $d_s = 30\,m$ and $d_i = 3\,m$, the FM is operated with R_b values of about 750 mm.

4.2 High-Pressure Technique for NFS

Diamond-anvil cells (DAC's) have been successfully used in conventional MS for almost two decades [CTW82]. A general overview over DAC's was provided by Jayaraman [Jay83]; various applications for MS are reviewed in [PT89, TP90, PT96]. The Mbar borderline for conventional MS was reached recently by M.P. Pasternak et al. [PTJ97].

Since MS experiments are performed in the same transmission geometry as NFS, DAC's for conventional MS can also be used for NFS experiments. In order to fully exploit the possibilities of nuclear scattering, a new DAC was developed on the basis of previously used cells (see e.g. [Hes97]).

This DAC (called DAC #1 in the following) is shown in figure 4.5. The central part is a pair of diamonds contained in a cylindrical press consisting of a piston (A in figure 4.5) and a cylinder (B). The diamond flats are aligned and adjusted with a half sphere (C) and an xy-stage (E), respectively. The force is generated by 8 screws (G) and balanced by a backing plate (F). The inner part of the cell with the sample (K) contained in a hole in the gasket (I) together with ruby chips (J) and pressure-transmitting medium (L) is shown on the right. The powder samples were grinded under inert atmosphere (N_2 or Ar) and mixed with epoxy as the pressure transmitting medium. Depending on the envisaged pressure range, the sample diameter within the $Ta_{90}W_{10}$ gasket varied from 250 μm (50 GPa) to 80 μm (100 GPa). The pressure was monitored before and after each measurement using the ruby fluorescence method [FPB72] with the non-linear calibration formula given in [MBS78].

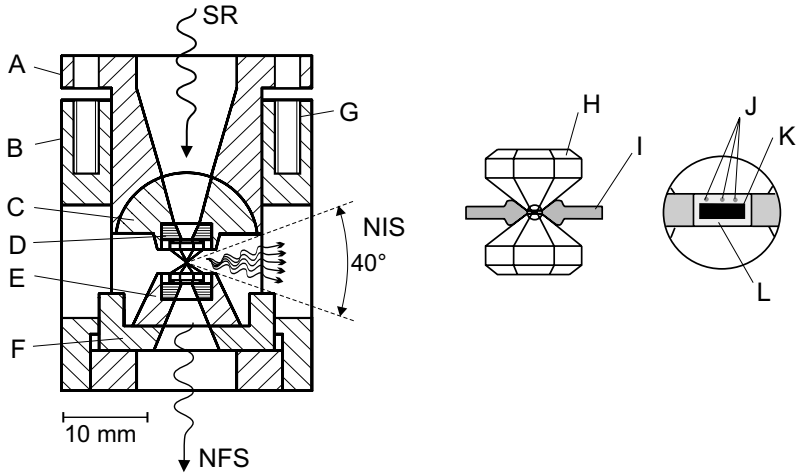

Figure 4.5: Sketch of the diamond anvil cell DAC #1 made of $Cu_{0.98}Be_{0.02}$ and employed for NFS in transmission geometry and for NIS. The two large openings in the cylinder are 17 mm x 10 mm (h x v). The resulting opening angle perpendicular to the beam is 40° and can be used for the insertion of two magnetic arrays (see figure 4.6) or for the detection of NIS. A: piston, B: cylinder, C: half sphere, D: diamond seats (also made of $Cu_{0.98}Be_{0.02}$), E: xy-stage, F: backing plate, G: 8 threads, H: diamonds, I: gasket, J: ruby chips, K: sample, L: pressure-transmitting medium.

The special features of DAC #1 for NFS are:

- Use of a nonmagnetic $Cu_{0.98}Be_{0.02}$ alloy which allows the application of an external magnetic field. Good mechanical stability for the alignment of diamonds with small flat sizes down to 0.2 mm was achieved by electroplating the piston (A) with a thin layer of hard chromium. The resulting surface is very stable and could be machined with high precision to a mechanical tolerance of $5-10\,\mu m$ relative to the cylinder (B).

- In order to apply an external field by an array of permanent magnets, the cylinder (B) of the DAC has two large openings (17 mm x 10 mm, h x v) as shown in figure 4.6. Each side of the magnetic array consists of two $Nd_2Fe_{14}B$ magnets and one iron pole piece. With a distance of 10 mm between the iron poles, homogenous fields up to 0.75 T were obtained.

The nuclear resonant count rates for high-pressure NFS experiments depend on the sample size (i.e. the pressure), the degree of enrichment in ^{57}Fe and the electronic absorption factor of the sample. At ESRF we achieved between 1 Hz for $GdFe_2$ at 105 GPa and 40 Hz for YFe_2 at 10 GPa (both enriched to 30% with ^{57}Fe). This leads to accumulation times for one spectrum between 120 min and 15 min, respectively.[3]

[3]The values were obtained without focusing optical elements. The beamsize was $\approx 1mm^2$.

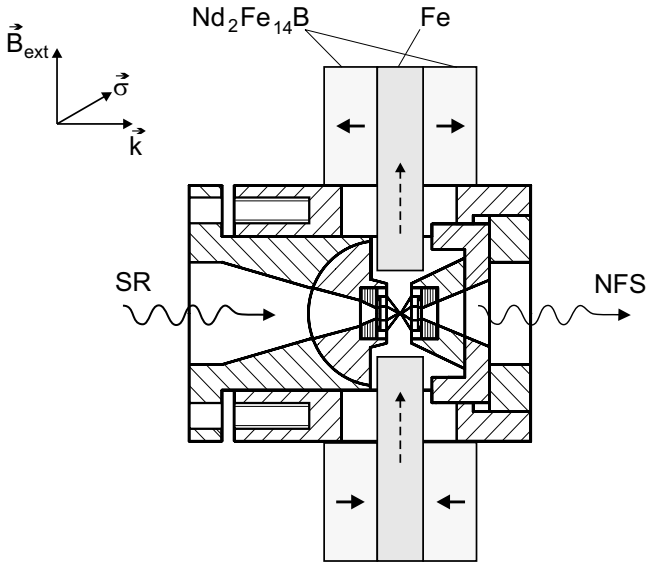

Figure 4.6: Schematic view of the experimental set-up with DAC #1 and an array of $Nd_2Fe_{14}B$ magnets and iron pole pieces which "guide" the magnetic flux to the sample. The magnetization directions are marked by arrows. The distance between the iron poles is 10 mm and homogenous fields up to 0.75 T were obtained.

For a pure ^{57}Fe-foil at ambient conditions, the countrate is in the range of kHz and a NFS spectrum can be taken within a few seconds.

After every run of NFS measurements at ESRF, the DAC's remained at the highest pressures (105 GPa for YFe_2 and $GdFe_2$, 51 GPa for $ScFe_2$) and additional experiments with conventional MS were carried out in Paderborn [Lu00]. Since DAC #1 has an opening angle of 25° in the direction of the beam, energy-dispersive XRD experiments are possible on the same sample. These measurements were conducted at beamline F3 at HASYLAB [Rei00] and yield important information on the crystal structure and the lattice parameter.

4.3 High-Pressure Technique for NIS

Since inelastically scattered radiation is emitted in 4π solid angle, an NIS experiment can not be performed in a simple transmission geometry[4]. For ^{57}Fe, the radiation consists with 89% probability of x-ray fluorescence photons with 6.4 keV.

The detection of low-energy photons with 6.4 keV in a high-pressure experiment is extremely hampered by the surrounding parts of the DAC. This is illustrated in figure 4.7

[4]Actually, the very first NIS experiment [SYK95] was performed in forward direction, where both NFS and NIS events were counted.

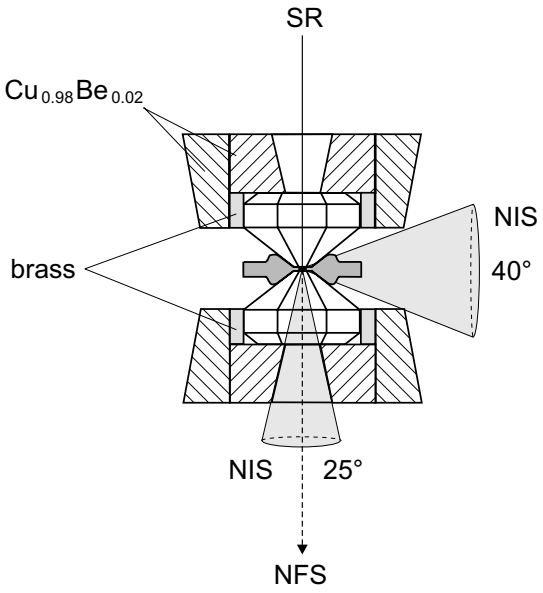

Figure 4.7: Possibilities for the detection of NIS in a high-pressure experiment with a standard setting of the diamond anvils. The scattered radiation in the forward cone (25°) is strongly absorbed by the diamond anvil and superimposed by NFS. A detection of x-rays perpendicular to the beam requires a low-Z gasket material.

where a diamond pair is shown together with its setting: (i) The emitted radiation in the forward opening cone of a DAC is strongly absorbed in a standard diamond anvil of 2.5 mm height (transmission below 0.01% for 6.4 keV and 50% for 14.4 keV; see figure 4.8) and superimposed by elastic forward scattering. (ii) The scattering perpendicular to the incoming beam is completely blocked by conventional gasket materials like $Ta_{90}W_{10}$, Inconel or steel. However, the transmission of x-rays through the gasket can be significantly enhanced, when gasket materials with low atomic number Z are chosen. This approach is well-known from XRD [KB76] and x-ray absorption spectroscopy (XAS) [IGS78] and requires large radial openings of the employed DAC. The most commonly used low-Z gasket materials are lithium hydride, beryllium and boron powder mixed into epoxy. Among these materials, beryllium (bulk modulus 110 GPa [You91]) allows for the highest pressures. The transmission of 6.4 keV photons through a typical Be gasket with 1 mm radius is about 70% (see bottom of figure 4.8). XAS experiments using Be in a DAC are reported by the Paderborn group up to 26 GPa at the L_{III}-edge (5.9 keV) of Praseodym [RL94, RL95]. In recent XRD experiments with a high-strength Be gasket, Hemley et al. reached pressures above 200 GPa [HMS97].

An experimental set-up for the high-pressure NIS experiments in this thesis was developed in three main steps:

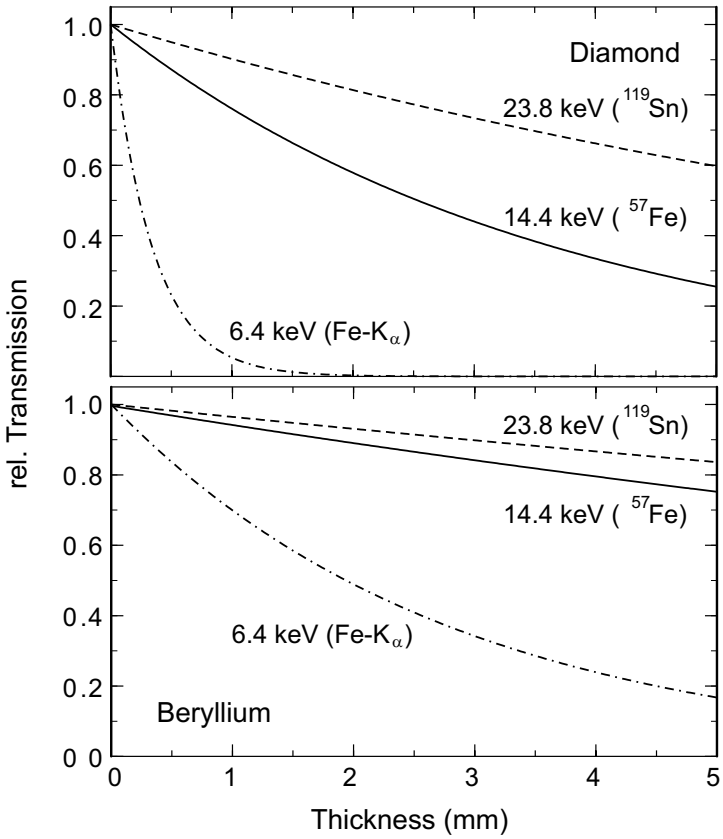

Figure 4.8: Relative transmission of x-rays through diamond (top) and beryllium (bottom) for different photon energies, calculated with absorption cross sections from [MMH69].

NIS on α-iron up to 10 GPa

The first NIS experiments (June 1997) under high pressure were performed with DAC #1 and two APD detectors perpendicular to the incoming beam. Since the detector boxes were larger than the openings in the DAC cylinder, they were placed outside the DAC. With an active area of 10 x 10 mm^2, 15 mm apart from the sample, each APD covered an opening angle of 37°. The flat size of the diamonds was 1.0 mm. The gasket was made of pure epoxy, hardened at 100° C. This gasket material, however, became unstable above 10 GPa. In several test experiments with a 150 μm thick Be foil, the gasket broke, beginning with cracks in the outer part, due to the brittleness of metallic Be.

After the NIS experiment at 10 GPa, it turned out that the mechanical control of the high-resolution monochromator had been defective: a reliable determination of the energy position was not possible and the data could not be used for further evaluation.

NIS on ε-iron at 24 GPa

For a second run of NIS experiments (June 1998) on ^{57}Fe, an optimized DAC (DAC #2) was developed. This cell is shown in figure 4.9a. The principle set-up is similar to DAC #1, but DAC #2 is bigger and has a larger opening (26 x 23 mm^2, h x v) perpendicular to the cell axis. The detectors can now be mounted inside the DAC, 5 mm apart from the sample. In order to fully exploit this detector acceptance, the lateral diamond setting (brass ring in DAC #1) was completely omitted. Instead, the diamonds were fixed with epoxy. This configuration allows an opening angle of 85°, as shown in figure 4.9b. However, for opening angles > 60° the opening cone includes transmission through up to ∼2 mm of diamond. This leads to an almost complete absorption of 6.4 keV photons and to 40% absorption of 14.4 keV photons.

In this run, diamonds with 0.5 mm flat were used and a cylindrical Be disk with 2 mm diameter and 250 μm initial thickness served as the gasket. In order to avoid a breaking of the Be, the disk was annealed at 800° C to reduce the brittleness. In addition, the disk had to be radially supported by an aluminium ring of 0.5 mm thickness. The maximum pressure was 24 GPa, enough to obtain the pure ε-phase of iron. However, this run suffered from a very low countrate of inelastically scattered photons and the statistical accuracy was not sufficient for data evaluation.

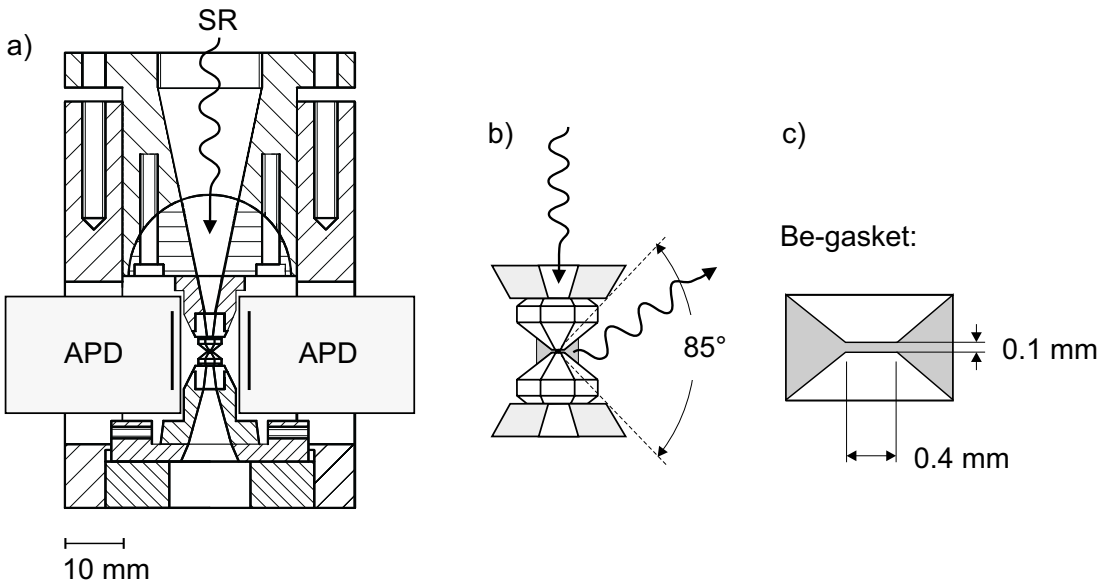

Figure 4.9: a) Sketch of DAC #2 with mounted detector boxes for the detection of NIS. b) Optimized diamond setting without radial support. The diamonds are fixed with epoxy which allows an opening angle of 85°. c) Sketch of the Be gasket with two conical drillings adapted to the dimensions of the diamonds.

NIS on α- and ε-iron up to 42 GPa

After these two attempts, which showed the principle feasibility of the present high-pressure techniques, a successful experiment was conducted in April 1999 at ESRF. NIS spectra were measured of α-Fe and ε-Fe at pressures up to 42 GPa. Two high-pressure cells of type DAC #2 were used for the whole series, utilizing diamonds with flat diameter of 1 mm for α-Fe and beveled diamonds with outer diameter of 0.4 mm (bevel 7°, inner diameter 0.3 mm) for ε-Fe.

A reasonable nuclear count rate of $\sim$ 4 Hz in the phonon wings of the NIS spectra at 42 GPa was made possible by the use of focusing optical elements (section 4.1.3) and a new Be gasket without an additional radial support and capable of higher pressures than previously achieved. The modified gasket is shown in figure 4.9c. It has a cylindrical shape with two conical drillings adapted to the dimensions of the diamonds [She98]. The thickness of the central part is $\sim$0.1 mm and was manufactured by acid etching [5]. When the gasket is pressed between the diamond anvils, the much thicker outer part remains unaffected and acts as a radial support for the inner part. A hole of 90 μm was drilled [6] into the gasket after prepressing to 40-50 μm. The iron foil (95% ^{57}Fe) was placed in the hole together with ruby chips and an ethanol/methanol/water mixture (13:4:1) as pressure transmitting medium.

For pressures up to 11 GPa a different approach for the gasket shape was made. It turned out that cracks at the edge of the Be gasket do not occur, when thin cylindrical Be disks are used, which have the same diameter as the diamond flat (thickness 0.15 mm, diameter 1 mm). In this case, the stress differences between outer and inner parts are minimized and the drilled gasket hole remains stable under pressure. Due to the larger sample volume (diameter 0.25 mm), the count rate for pressures up to 11 GPa was $\sim$ 7 Hz. However, this approach is not applicable for smaller diamond flats.

[5] Phoenix Precision, Hudson, MA (USA)

[6] Elemental beryllium and BeO are extremely toxic, when incorporated. Every machining has to be done with appropriate safety precautions. For the drilling procedure, the gaskets were fixed with adhesive and covered with mineral oil.

Chapter 5

NFS in RFe_2 Laves Phases

The investigation of RFe_2 compounds in this thesis is part of a series of Diploma- and Ph.D.-theses using x-ray diffraction (XRD) [Web95, Rei00], x-ray absorption spectroscopy (XAS) [Nes98, SGG98], x-ray magnetic circular dichroism (XMCD) [GSW98], Mössbauer spectroscopy (MS) [Rup99a, Lu00, Str00, SW99] and resistivity measurements [Str00] for the structural, electronic and magnetic characterization of RM_2 Laves phases under pressure. From the introduction of Nuclear Resonant Scattering in chapter 3 it is obvious that, disregarding all methodical differences, NFS and MS give in principle the same kind of information on the physical properties of a sample. Consequently, the present work – actually the first systematic NFS study of samples with complex (magnetic + electric) hyperfine interactions – was performed in close collaboration with the accompanying Mössbauer studies.

We start with a brief introduction of the basic properties of RFe_2 Laves phases followed by the main topic of this chapter: the NFS experiments for the investigation of magnetism in RFe_2 (R=Y, Gd, Sc, Ti) up to the Mbar range. Special emphasis is devoted in section 5.2 to the particular properties of the data evaluation in NFS. A comparison with the MS studies will be given throughout the presentation of the experimental results in section 5.3.

5.1 Structure and Magnetism of RFe_2 Laves Phases

5.1.1 Crystal Structure

The Laves phase structures C15 and C14 are adopted by a large number of binary intermetallic compounds of composition RM_2. Depending on the ratio of the ionic radii of R and M as well as on the averaged conduction electron number the C15 or C14 structure appears [BCK90] (see figure 5.1). The cubic C15 phase ($MgCu_2$, Pearson symbol cF24) is a common structure for RM_2 intermetallics with *R* as the

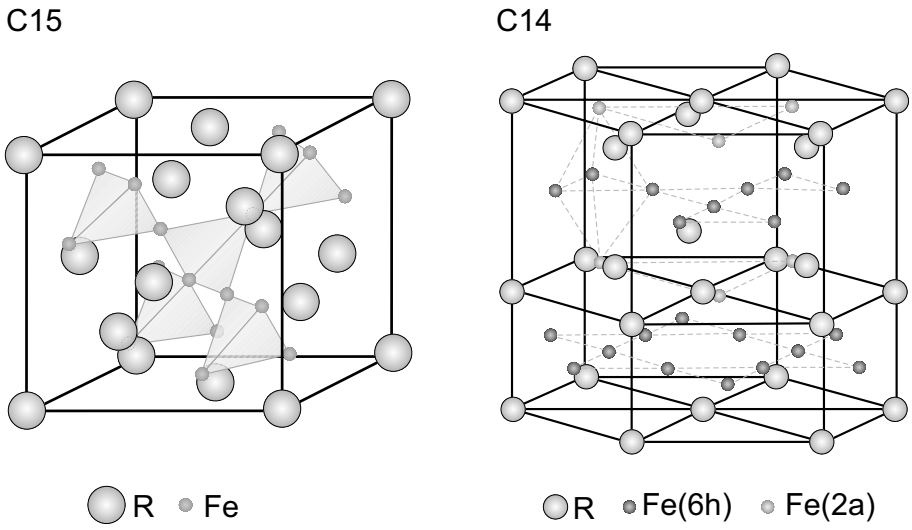

Figure 5.1: C15 and C14 structures of RFe_2 Laves phases.

larger metal ion like trivalent Y and *Ln* (lanthanide) metals and M = 3d metals like Mn, Fe, Co, Ni, and also simple metals like Al. The hexagonal C14 phase ($MgZn_2$, Pearson symbol hP12) is formed, for instance, with R as a trivalent, tetravalent or pentavalent d-metal like Sc, Ti, Hf, Ta.

In the C15 structure, all R and all M sites are crystallographically equivalent. The R sites build up a diamond lattice, whereas the M atoms form tetrahedra connected via their corners to fill up the empty interstices. The R sites have local cubic symmetry, whereas the M sites have local C3 symmetry. In the C14 structure, the R sites form a hexagonal lattice, resembling in some aspects a hcp lattice. The interstices are filled again by M tetrahedra, sharing now common planes and corners. The two M sites, 6h and 2a, are crystallographically and magnetically different.

For both C15 and C14 structures the R and M sites are similarly coordinated: the M sites have 6 M and 6 R nearest neighbours and the R sites have 12 M nearest neighbours. This (joint) coordination number of 12 makes the C15 and C14 structure similar to the fcc and hcp lattice of monoatomic metals, e.g. to γ-Fe and ε-Fe, the fcc and hcp allotropes of iron. Due to their simple structure, the RFe_2 Laves phases are considered as model systems for Fe magnetism in intermetallic compounds. [1]

[1]For comparison, the technological relevant compound $Nd_2Fe_{14}B$ has a tetragonal structure with 68 atoms per unit cell. The 6 crystallographically different Fe sites have 8-12 nearest Fe neighbours with mean Fe-Fe distances ranging from 2.54 to 2.70 [Dep87].

5.1.2 Magnetism in R-Fe Compounds

The electronic structure and magnetism of R-Fe compounds is governed by three kinds of electronic states [Ric98a]:

- R 4f states forming a subsystem of localized magnetic moments,
- Fe 3d band states which both participate in metallic bonding and magnetic order,
- nearly free conduction electron states responsible for metallic bonding and coupling of the two different magnetic subsystems (R 5d and Fe 4s).

The relevant energies for the electronic and magnetic interactions [2] within the two subsystems are the on-site Coulomb correlation energy U and the bandwidth W, representing the *intra*- and *inter*atomic interaction between electron states, respectively. The balance between these energies decides whether the electrons remain localized or whether itinerant band states are formed. In the extreme cases we have a system with well-defined local moments in the strong correlation limit ($U/W \gg 1$) and a Pauli paramagnet in the weak correlation limit ($U/W \ll 1$). The localization threshold is about $U/W \approx 5-10$ for almost empty or almost completely filled shells, and $U/W \approx 1$ for half-filling [Ric98a].

For rare earth 4f states with negligible overlap between neighbouring atoms, $W_{4f} \approx 0.5$-0.2 eV is small and decreases from Ce to Lu, whereas U_{4f} varies between 5 and 10 eV. Consequently, all rare earth metals at ambient conditions have localized 4f states. This property is prevailed in R-Fe intermetallics with the exception of Ce compounds, where 4f contributions to the chemical bonding have been found for example in $CeFe_2$ [BCK90]. The magnetism of localized moments is usually described within the Heisenberg model, assuming an interaction Hamiltonian which is proportional to the dot product of the spins:

$$H_{ex} = -2\,J_{ij}\,\vec{S}_i \cdot \vec{S}_j. \tag{5.1}$$

The so-called exchange parameter J_{ij} represents the coupling strength between the moments of two different atoms labelled i and j. Due to the absence of direct exchange the coupling between atomic rare earth moments is mediated by conduction electrons. When considering a solid it is necessary to sum the exchange over all pairs of atoms which contribute to the interaction. In many cases one is only interested in nearest-neighbour interactions and the Heisenberg Hamiltonian is simplified to $H_{ex} = -2\,J\sum \vec{S}_i \cdot \vec{S}_j$ where the sum is only over nearest neighbours with the corresponding value of J. Obviously, $J > 0$ provides ferromagnetic and $J < 0$ antiferromagnetic ordering.

[2] Unless not mentioned explicitely, these interactions are considered at low temperatures.

A contrasting picture to the 4f states holds for transition metals with incompletely filled 3d shells. The wave functions are spatially more extended than those of R 4f states. Thus, $U_{3d} \approx$ 1-3 eV is considerably smaller than U_{4f}. Even more important is the absence of closed shells outside the 3d shell. This leads to a large overlap of neighbouring 3d wave functions. Consequently, $W_{3d} \approx 8-5$ eV is much larger than the related 4f value and 3d band states are formed. Even within the band picture the degree of localization varies depending on U/W. The spatial extension of the electron states and possible magnetic moments increases with decreasing U/W.

A precondition for a net magnetic band moment is the imbalance of spins caused by the intraatomic exchange interaction between the electrons. The larger the exchange energy the greater the exchange splitting Δ ($\approx 1.8\,$eV for Fe) between the spin up and spin down half bands. The schematic band structure density of states $D(E)$ with an exchange splitting Δ of the half bands is shown in figure 5.2. It is easily seen that the magnetic 3d moment μ_{3d} depends on both, the exchange splitting Δ and the density of states at the Fermi level $D(E_F)$. The Stoner criterion $I \cdot D(E_F) > 1$ for the stability of a ferromagnetic phase combines these two parameters: the strength of the intraatomic exchange interaction, described by the Stoner parameter I, and a high density of states $D(E_F)$.

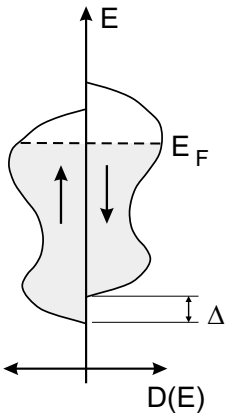

Figure 5.2: Schematic band structure density of states $D(E)$, showing exchange splitting Δ of the spin up and spin down half bands.

Sublattice Coupling

In RFe_2 systems the two types of magnetic sublattices are "pasted" together by interatomic 3d-5d coupling which appears to be antiferromagnetic and originates from the interplay of hybridization and spin polarization between a nearly filled 3d shell (Fe) and a nearly empty 5d shell (R) [Ric98a]. It can produce significant conduction electron and spin density at the R sites, even when they possess no 4f moment. This is demonstrated in YFe_2 with an induced moment of -0.45 μ_B at the Y site [ADM86].

However, for R=Y the magnetic moment is due to 4d polarization and 3d-4d coupling which is completely analogous to the above mentioned 3d-5d coupling for the Lanthanides where band structure calculations [LBC94] yield a Gd 5d moment of -0.54 μ_B in $GdFe_2$.

The connecting link for the magnetic exchange between the 3d and 4f subsystems is the intraatomic 4f-5d interaction in the R atoms. Hereby, the 4f *spin* moments polarize locally the 5d electrons via ferromagnetic exchange interaction. However, the direction of the 4f *total* moment depends on the size and direction of the orbital moment. According to Hund's third rule this gives (with the above antiferromagnetic 3d-5d coupling) ferromagnetic ordering of Fe and R moments for the light rare earth (J=L-S) and ferrimagnetic ordering for the heavy rare earth (J=L+S). The alignment of the two spin moments leads to an energy reduction of $E_{4f5d} \approx$ 10-100 meV, depending on the size of the 4f spin moment [BNJ91]. Canted spin structures can occur when the crystal field energy is larger than E_{4f5d}.

A measure for the R-Fe interaction is the coupling constant J_{RFe} appearing in the nearest-neighbour Heisenberg-type Hamiltonian $H_{ex} = -\sum 2J_{RFe}S_R S_{Fe}$ with R and Fe spins S_R and S_{Fe}, respectively. It can be obtained with high-field magnetization experiments. For $GdFe_2$ a value of $J_{RFe} = -22\,K/k_B = 1.9\,meV$ is found [LBC94]. However, despite the high spin moment at the R sites, the driving force of magnetic order in RFe_2 compounds is the 3d spin polarization. This is reflected by the much larger coupling constant J_{FeFe}, which was determined with spin waves in inelastic neutron scattering for YFe_2 to be 24.4 meV [PCR99]. Since this value is very close to that of α-Fe (24.0 meV), and trivalent Y has no open d or f shells, the authors of [PCR99] consider YFe_2 as "diluted iron in the cubic C15 structure". The $R-R$ coupling J_{RR} is small compared to J_{FeFe}. This was shown by resistivity measurements in $GdFe_2$, which revealed an ordering temperature of 140 K for the Gd sublattice [SW99].

5.1.3 Magnetic Phase Diagram

The impact of different constituents R with different size and coupling to the Fe system on the magnetic properties of RFe_2 compounds is shown in figure 5.3. The figure presents the ordering temperature T_m and the magnetic hyperfine field B_{hf}; the latter related for RFe_2 systems to the magnetic moment μ_{Fe} by $\mu_{Fe}/\mu_B = B_{hf}/14.7\,T$ [BCK90]. In order to compare materials with different crystal structure, the $Fe-Fe$ distance d_{Fe-Fe} is chosen as the common parameter for the x-axis. For C15 systems, this parameter depends in a simple way upon the lattice constant a according to $d_{Fe-Fe} = \sqrt{2}\,a/4$. For the C14 structure, the distances between iron atoms in 6h and 2a sites are slightly different [3] and the average is taken for representation in figure 5.3.

[3] The Fe(2a) atoms have 6 nearest Fe(6h) neighbours with equal distance whereas the Fe(6h) atoms have 4 nearest Fe(6h) neighbours and 2 Fe(2a) neighbours with different distances ($\Delta d_{Fe-Fe} \approx 0.04$ Å for $TiFe_2$).

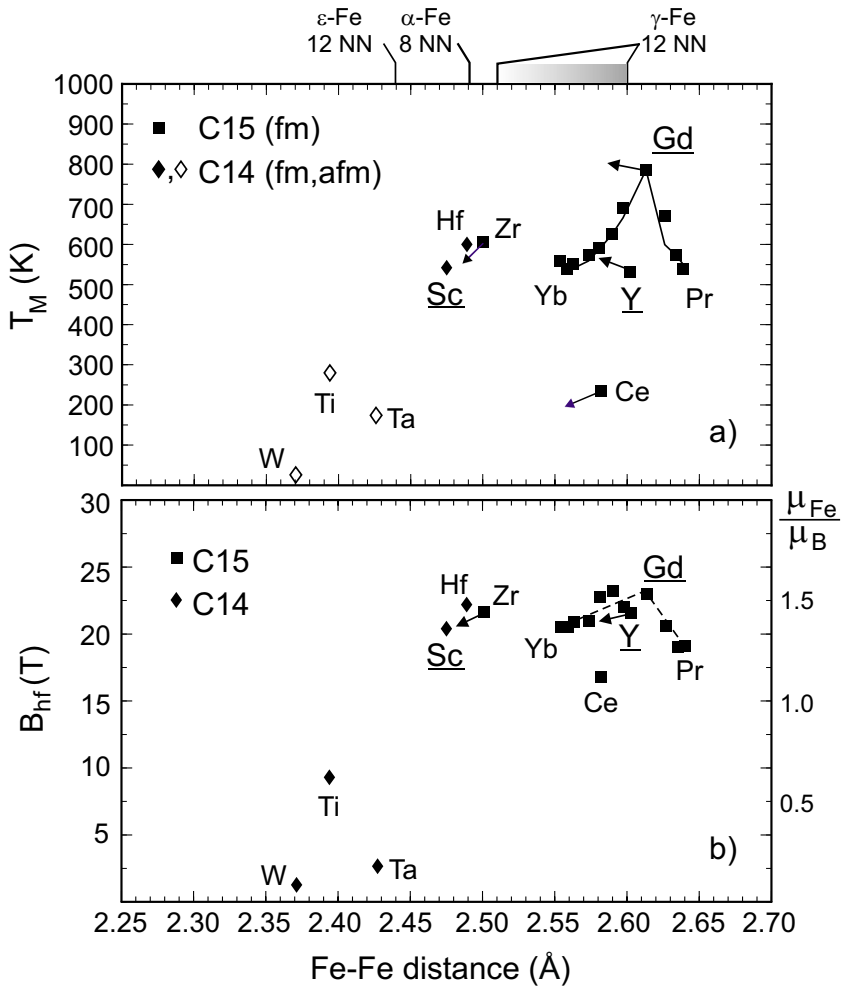

Figure 5.3: Magnetic ordering temperatures (a) and hyperfine fields at 4.2 K (b) versus Fe-Fe distance for different RFe_2 Laves phase compounds; compiled from [BCK90]. Full symbols are for fm ordering and open symbols for afm ordering. The solid line represents calculated values for T_m according to equation 5.2. The arrows indicate the low-pressure behaviour of T_m, derived from resistivity studies [BB73] and of B_{hf} derived from NMR studies [DRM86]. The proportional behaviour of B_{hf} and the iron moment μ_{Fe}, marked on the right axis of (b), is given in [BCK90].

Magnetic Ordering Temperatures

All RFe_2 C15 compounds order ferro- or ferrimagnetically (see right part of figure 5.3a). The influence of the $R-Fe$ coupling is reflected by the increase of T_C from 535 K for Y without intrinsic moment to a maximum of 790 K for Gd with J = S = 7/2. In analogy to a similar compilation of T_C values in $R_2Fe_{14}B$ compounds [SRF84], the increase of

T_C in RFe_2 can be described by a mean-field approach

$$\begin{aligned} 3\,k_B\,T_C &= a_{FeFe} + a_{RR} + \left[(a_{FeFe} - a_{RR})^2 + 4\,a_{RFe}\,a_{FeR}\right]^{1/2} , \qquad (5.2) \\ a_{FeFe} &= Z_{FeFe}\,A_{FeFe}\,S_{Fe}\,(S_{Fe}+1) , \\ a_{RR} &= Z_{RR}\,A_{RR}\,G , \\ a_{RFe}\,a_{FeR} &= Z_{RFe}\,Z_{FeR}\,S_{Fe}\,(S_{Fe}+1)\,G\,A_{RFe}^2 \end{aligned}$$

with the iron spin S_{Fe}, the de Gennes factor $G = (g-1)^2 J(J+1)$ for the R spin and the number of nearest neighbours $Z_{FeFe} = 6$, $Z_{RR} = 6$, $Z_{RFe} = 12$ and $Z_{FeR} = 6$. The variables a_{xy} represent the magnetic interaction energy between the x and y spins. The respective coupling parameters A_{xy} are related to the above mentioned exchange parameters J_{xy} but are usually treated as empirical. They are assumed to be identical for all R and can be estimated from

- the value of $T_C = 535\,\mathrm{K}$ in YFe_2 with $G = 0 \rightarrow A_{FeFe} = 8.8\,\mathrm{meV}$,
- the ordering temperature 140 K of the Gd sublattice in $GdFe_2$ with $G = 15.75$ $\rightarrow A_{RR} = 0.19\,\mathrm{meV}$,
- the ordering temperature $T_C = 790\,\mathrm{K}$ in $GdFe_2 \rightarrow A_{RFe} = 1.37\,\mathrm{meV}$,

using $S_{Fe} = \mu_{Fe}/2\mu_B \approx 0.75$. The calculated values for the other rare earths from equation 5.2 are indicated by the solid line in the right part of figure 5.3a, connecting the T_C values of C15 type RFe_2 systems. As mentioned above, the $CeFe_2$ compound has non-systematic magnetic properties with respect to the remaining RFe_2 series.

The C14 structure is preferred for smaller constituents R (see left part of figure 5.3a). $ScFe_2$ is ferromagnetically ordered with the Fe moments of both 6h and 2a sites directed along the c-axis. Going from $ScFe_2$ to $TiFe_2$, the ordering temperature decreases drastically from 542 K to 283 K and $TiFe_2$ shows an interesting antiferromagnetic structure: The 6h sites are ferromagnetically ordered within the planes, the moments oriented along the c-axis; the 6h planes, however, couple antiferromagnetically, leaving the 2a sites in a non-magnetic position [BCK90].

Magnetic Hyperfine Fields

The behaviour of the magnetic hyperfine fields for C15 compounds in figure 5.3b indicates that also the Fe moment itself is affected by different R neighbours. Although the qualitative dependence on the R spin moment is similar to T_m, the effect is much smaller. Magnetization measurements in the $Y_xGd_{1-x}Fe_2$ series yield a continuous increase of μ_{Fe} from 1.45 μ_B in YFe_2 to 1.6 μ_B in $GdFe_2$ [BU79]. Consequently, the effect

of transferred hyperfine fields from the *R* sites can be neglected at ambient pressure. Similar to the volume-dependence of T_m, also the hyperfine fields show a considerable decrease for smaller Fe-Fe distances reaching a "low-moment" state with $\mu_{Fe} = 0.7\,\mu_B$ in $TiFe_2$.

The direction of the hyperfine fields relative to the crystal lattice and hence to the electric field gradient (EFG) is governed by the structural properties of the Laves phases and by the direction of magnetization $\vec{M}$. As elaborated in detail by Genin et al. [GBB81] for the C15 structure, the direction of the main axis of the EFG is determined by the angle β between $\vec{M}$ and the particular trigonal axis of the iron atoms at the four tetrahedra corners ([1 1 1],[$\bar{1}$ 1 1],[1 $\bar{1}$ 1],[1 1 $\bar{1}$]). This leads to four magnetically ineqivalent Fe sites for an arbitrary direction of $\vec{M}$. The number of different Fe sites can be less than four, if one considers directions of $\vec{M}$ with certain symmetries. Since the effect on the energy levels is given by $f(\beta) = (3\cos^2\beta - 1)/2$ the simplest case is given for a magnetization along the [1 0 0] direction, as in the case of *R* ions like *Dy* and *Er* with large 4f orbital moments. Then all Fe sites remain magnetically equivalent and the magnetic hyperfine field and the EFG form the "magic" angle, $\beta = 54.7°$ ($f(54.7°) = 0$). When the magnetization is along the [1 1 1] direction, which is the case in RFe_2 C15-phases with non-magnetic *R* metals like Y and *Lu* [BCK90], there are two magnetically non-equivalent Fe sites in the ratio 3:1; the majority site with an angle $\beta_1 = 70.5°$, the minority site with $\beta_2 = 0°$. $GdFe_2$ with a large S = 7/2 spin moment has no simple axis of magnetization. Genin et al. propose that $\vec{M}$ lies between the [1 1 1] and [1 1 0] direction [GBB81]. This case of a not well-known or well-defined magnetization direction is approached by 4 sublattices with varying angles β. Since the dipolar contribution to the hyperfine field shows the same angular dependence of the angle β, there is usually a clear correspondence between $f(\beta)$ and the magnitude of the hyperfine field [GBB81, BCK90].

The magnetic properties of the hexagonal C14 RFe_2 compounds are also strongly influenced by their crystal structure with two inequivalent Fe sites 6h and 2a in a ratio 3:1. For the 2a sites the main axis of the EFG is oriented parallel to the magnetization which points in the [0 0 1] direction ($\rightarrow \beta = 0°$). The Fe atoms on the 6h sites experience an EFG which is perpendicular to the c-axis ($\rightarrow \beta = 90°$).

Regarding figure 5.3, the overall variation of magnetic properties in RFe_2 Laves phases with decreasing d_{Fe-Fe} can be summarized as follows:

1. Suppression of the Fe moment from a relatively localized high band-moment via a more itinerant low-moment to a non-magnetic state.

2. Decrease of the magnetic exchange coupling reflected by the decreasing ordering temperatures.

3. Change of the magnetic ordering type from ferro- to antiferromagnetism.

4. Preference of the hexagonal C14 structure for smaller volumes.

The features described in 1.-3. are analogous to the behaviour of γ-Fe on CuAu substrates, where the lattice parameter can be adjusted by a varying Au-concentration [KSF95] (indicated on the top of figure 5.3).

Following this argumentation the motivation for high-pressure experiments is obvious: Is the decrease of the $Fe-Fe$ distance the main reason for the strong variation of magnetic properties in RFe_2 i.e. is d_{Fe-Fe} a "universal" parameter for the description of iron magnetism in these compounds? The application of high pressure gives the unique possibility to answer this question for particular samples without influence of a changing number of conduction electrons due to different constituents *R*.

For the present NFS high-pressure studies, the samples YFe_2, $GdFe_2$ and $ScFe_2$ were chosen. YFe_2 is representing the case of a non-magnetic *R* atom in the C15 systems. The influence of a magnetic 4f sublattice can be studied by comparison with $GdFe_2$. Furthermore, these two compounds have similar lattice constants at ambient pressure and also the electron concentration does not change when replacing yttrium by gadolinium. The bulk moduli are 133 GPa (YFe_2) and 104 GPa ($GdFe_2$) [Rei00]. The low-pressure behaviour of T_m (from resistivity experiments [BB73]) and B_{hf} (from NMR [DRM86]) are indicated by arrows in figure 5.3. For the envisaged pressure range of 100 GPa (=1Mbar) the reduction of d_{Fe-Fe} is as large as 10% covering the whole range of Fe-Fe distances shown in the figure.

The possible occurrence of a pressure-induced structural transition from C15 to C14 is subject of a close collaboration with XRD experiments of G. Reiss [Rei00].

The compounds $ScFe_2$ and $TiFe_2$ are studied as C14 reference systems, the latter only at ambient pressure. In the $Sc_{1-x}Ti_xFe_2$ alloy series, a transition from ferro- to antiferromagnetism can be reached at x = 0.65 [NY85, NY86]. Since the substitution of Sc by Ti is accompanied, beside a change in the averaged conduction electron number, by a decrease of the lattice parameters, we expected that this magnetic transition can be also induced in pure $ScFe_2$ by the application of pressure.

5.2 Special Features of NFS Spectra

Before presenting the high-pressure spectra of RFe_2 (R=Y,Gd,Sc) Laves phases we discuss typical features of the NFS for systems with (i) texture effects (magnetic + crystallographic, section 5.2.1), (ii) a combination of magnetic and electric hyperfine interactions (section 5.2.2) and (iii) thickness distributions (section 5.2.3).

5.2.1 Texture Effects

Texture effects in NFS spectra are due to the interplay between preferred orientations of magnetic and/or crystallographic axes in the sample and the polarization of the SR. They are inevitable in a high-pressure cell and we show, as the simplest case, the impact of a magnetic texture on the NFS spectrum of an ^{57}Fe foil, as used for calibration purposes in conventional MS and NFS. Figure 5.4 shows the NFS spectrum of this foil assuming (a) no texture and (b) a magnetic texture for the fit done with the CONUSS program package [SG94]. It is evident that the fit without texture is only a poor representation of the data, whereas the fit including texture delivers a much better adjustment.

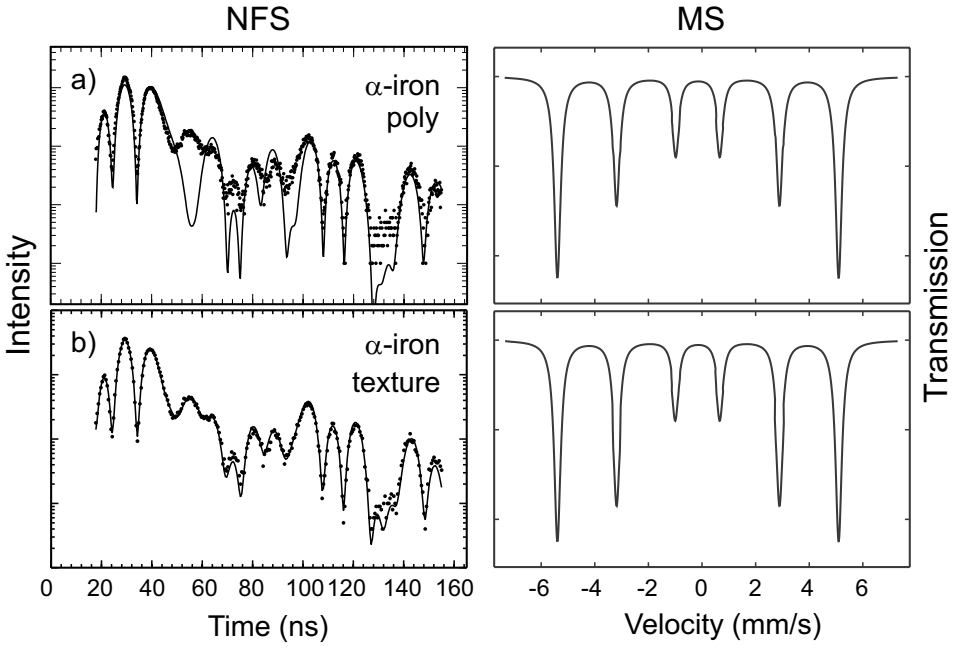

Figure 5.4: NFS spectrum of magnetic α-iron shown together with a fit assuming (a) a random orientation of the magnetic hyperfine axis and (b) a magnetic texture (30%) within the sample plane. The corresponding spectra (schematic) for conventional MS are shown in the right panel.

In conventional MS, the texture can be considered by one additional parameter, describing the deviation of the averaged magnetization in the absorber plane from the magic angle 54.7°. In the case of a magnetic iron foil, the direction of preferred magnetization normally lies predominantly in the plane of the foil, which results in an averaged polarization angle larger than 54.7°.

The situation in NFS is different due to the well-defined polarization vector $\vec{\sigma}$ of the SR. For a polycrystalline sample with different orientations of domains with magnetization $\vec{M}$, the averaging procedure for all combinations of $\vec{M}$ and $\vec{\sigma}$ is done by the evaluation software. Deviations from a completely random orientation can be accounted for by a texture coefficient C_{tex}, describing the percentage of Fe atoms with a certain preferred magnetization direction $\vec{M}_{tex}$. In general, the orientation of $\vec{M}_{tex}$ with respect to $\vec{\sigma}$ is defined by another two parameters. For the above mentioned iron foil, the number of free parameters is reduced to one, namely C_{tex}, by the assumption of a random distribution of $\vec{M}_{tex}$ within the sample plane. The fit analysis in figure 5.4b yields a percentage of 30% polarization.

5.2.2 Complex Hyperfine Interactions / External Field

So far, we considered the simple case of pure magnetic hyperfine interactions in a ^{57}Fe-foil. However, all investigated compounds in this thesis exhibit a combination of magnetic and electric interactions leading to more complicated spectra. The related features are presented in the following example for NFS spectra of YFe_2 measured at ambient pressure at the BW4 Beamline of HASYLAB in 2-bunch mode, providing a time window of 480 ns (figure 5.5). The sample with 30% enrichment in ^{57}Fe was prepared by mixing the grinded material with paraffin. The area density of 12 mg/cm^2 leads to an effective thickness of $\chi \approx 40$. The spectra were recorded at 300 K without external field and at 77 K with a polarizing field of 3 T, provided by a superconducting solenoid.

The NFS spectrum of YFe_2 without a polarizing field was fitted, according to section 5.1, with two sites in the ratio 3:1 with $B_{hf,1}$ = 18.6 T and $B_{hf,2}$ = 17.9 T and a quadrupole splitting $\Delta E_Q = eQV_{zz}/2 = (-)0.35\ mm/s$ ($\beta_1 = 70.5^\circ$ and $\beta_2 = 0^\circ$).[4] Similar to the case of α-Fe without external field, a small magnetic texture ($C_{tex} = 20\%$) has to be taken into account. This texture is actually not expected for a powdered sample of a cubic compound embedded in paraffin, but may be due to a remaining magnetization from previous experiments in external fields.

With the application of an external field B_{ext} = 3 T at 77 K, the magnetization in the polycrystalline YFe_2 sample is fully aligned in the same configuration as in the case

[4] Since an inversion of the energy scale for hyperfine interactions has no effect on the time spectrum, the sign of the electric quadrupole splitting can not be determined with this NFS spectrum. For the Laves phase compounds the negative sign is well established (e.g. [BCK90],[Rup99a]) and therefore indicated here in brackets for consistency. For the sign determination with NFS see section 5.3.5.

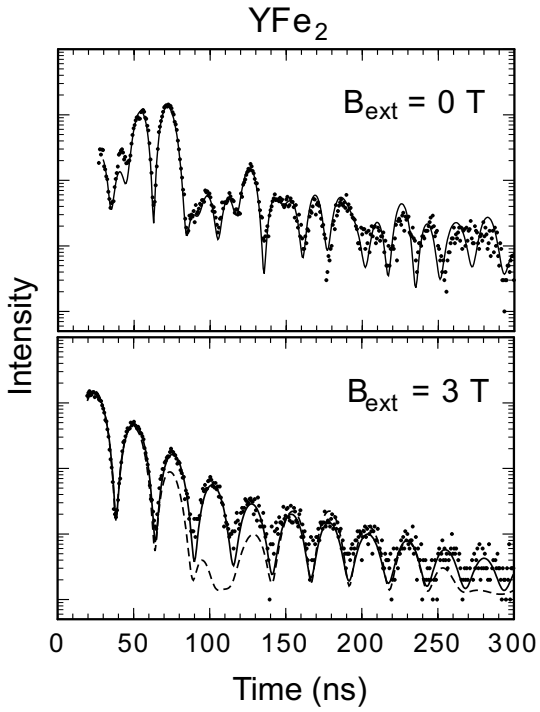

Figure 5.5: NFS spectra of YFe_2, measured at BW4 (HASYLAB) without (300 K) and with (77 K) external field of 3 T. The solid lines are fits assuming a magnetic texture with $C_{tex} = 20\%$ for the upper and 100% polarization for the lower spectrum. The dashed line at the bottom indicates the calculated spectrum for uniform effective thickness of $\chi = 40$.

of α-Fe in figure 3.9c: $\vec{B}_{\text{ext}}$ is perpendicular to the direction $\vec{k}$ and polarization $\vec{E}$ of the SR. A similar "simple" periodic beat structure appeared, now with a modulation frequency corresponding to the smaller splitting of the $\Delta m = 0$ transitions in YFe_2.

Since the direction of the EFG is determined only by the orientation of the crystal axes, the angle between quadrupole interaction and hyperfine field is now randomly distributed. This situation is adopted in the CONUSS program package by the adjustment with one value B_{eff} for the magnetic field and a grid of 48 subspectra with varying angles β. The fitted value of B_{eff} = 18.0 T leads to $B_{hf} = B_{\text{eff}} - B_{\text{ext}}$ = -21.0 T at 77 K. The external field lowers the hyperfine field at the nucleus because the hyperfine field is antiparallel to the Fe band moment which is aligned by the external field.

According to the estimated effective thickness of $\chi \approx 40$ ($\chi = 20$ per resonance line) a Bessel beat minimum should appear in the polarized NFS spectrum at 105 ns as indicated by the calculated dashed line in figure 5.5. However, this calculation is only valid for samples with homogeneous thickness such as properly rolled metallic foils. The absence of a Bessel beat can be explained by a variation of the local thickness in a powder sample. In this case the superposition of scattering intensities (see also the coherence aspects in chapter 3.2.4) with minima at different places leads to a blurring

of the Bessel beats. For the actual fit of the YFe_2 data a variation of $15 \pm 7\,\mu m$ has to be assumed where ± 7 denotes half the width of a Gaussian distribution. Thus, the final fit consists of subspectra with Bessel minima ranging from 70 ns (22 μm) to 200 ns (8 μm). The impact of this effect is much less pronounced for the unpolarized case since the effective thickness per resonance line is smaller and varies for the different hyperfine transitions.

From the experience with grinded powder samples in paraffin, e.g. from X-ray absorption spectroscopy, such a huge thickness distribution of $15 \pm 7\,\mu m$ was unexpected and thought to be unrealistic. However, as will be shown in the next section, the distribution of different thicknesses depends strongly on the spatial resolution of the observation method.

5.2.3 Thickness Distributions

With respect to the homogeneity of a sample, rolled foils with well-defined uniform thickness are perfectly suited for many kinds of experiments with transmission geometry. When such foils are not available the grinding of powder materials is the usual way of sample preparation. In order to avoid effects of severe milling on the structural and magnetic properties of a sample (studied for YFe_2 in [LAB95]) typical grain sizes are in the range of about 1-5 microns as revealed by a microscopical inspection of the present YFe_2 sample.

The resulting thickness distribution depends on the spatial resolution of the observation since integration over large (compared to the grain size) sample areas leads to an averaging. This effect is demonstrated by a computer simulation of an artificial sample obtained by random distribution of spherical grains in a virtual "paraffin volume" of $250\,\mu m \times 250\,\mu m \times 250\,\mu m$ (see figure 5.6). The number of different spheres with diameters 1-5 μm (see table 5.1) is chosen in a way that every species of spheres occupies 1/5 of the total volume. In order to match the area density of the real sample (12 mg/cm^2, average thickness of YFe_2 15 μm) a total number of 453838 spheres was used.

sphere diameter (μm)	number	ratio
1	360000	1
2	72000	2^{-3}
3	13333	3^{-3}
4	5625	4^{-3}
5	2880	5^{-3}

Table 5.1: Distribution of different sphere diameters for the computer simulation of an artificial sample in figure 5.6.

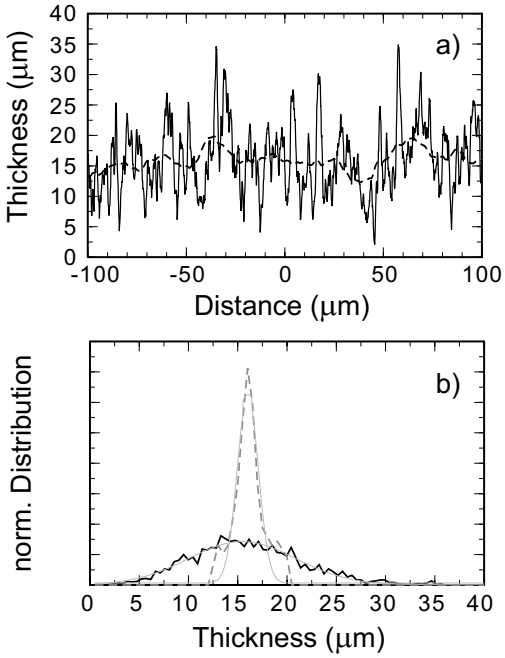

Figure 5.6: (a) Thickness of an artificial sample (mean thickness 15 μm) "seen" with a spatial resolution of 0.1 μm (solid line) and 25 μm (dashed line). The sample was obtained by random distribution of 453838 spheres in a volume of $(250\,\mu m)^3$. The used sphere diameters are listed in table 5.1. (b) Normalized thickness distributions for the corresponding curves in (a). The thin lines represent Gaussian fits with a FWHM of 13 μm and 2.5 μm, respectively.

The resulting thicknesses are calculated with 0.1 μm resolution for a linear chain (length 200 μm) in the central part of the artificial sample (solid line in figure 5.6a). Within this small spatial resolution the corresponding thickness distribution (figure 5.6b) is very broad. It can be approximated by a Gaussian with FWHM of 13 μm. When the thickness is averaged with a resolution of 25 μm (dashed line in figure 5.6) the sample appears much more homogenous and the width of the distribution decreases drastically to a FWHM of 2.5 μm.

According to chapter 3.2.4 the spatial resolution of NFS is given by the transverse coherence length L_{tr}. Since this value is in the order of 10-100 nm for usual experimental conditions, the large thickness distribution, necessary to explain the blurring of Bessel beats, can be made plausible by the above simulation.

Although thickness distributions can be accounted for in the analysing software, they render the data evaluation more difficult and tend to mask the influence of hyperfine interactions. They could be reduced in powder samples with a larger thickness compared to the grain size, keeping the effective thickness constant by the use of non-enriched material. However, this pathway will reduce the available count rates in a NFS experiment and is not desirable for high-pressure experiments.

5.3 Results

The high-pressure NFS investigations, presented in the following, were carried out at room temperature (294 K) using the experimental set-up described in chapter 4. Hereby, the magnetic properties of YFe_2 and $GdFe_2$ were studied up to a maximum pressure of 105 GPa (=1.05 Mbar). As explained in the previous section 5.2.2, the sophisticated influence of an arbitrary magnetic texture can be overcome by inducing a well-defined polarization in an external magnetic field. On the other hand, the averaging procedure for the angle β in the polarized case destroys the information on the relative orientation of hyperfine field and electric field gradient. Therefore, the NFS spectra were recorded as often as possible *with* and *without* an external field. In special cases ($GdFe_2$) this provides additional information on the magnetic ordering type.

5.3.1 YFe_2

Fig. 5.7 shows NFS spectra of YFe_2 at various pressures with a polarizing field in the same configuration as explained above. The simple beat pattern at ambient pressure, now measured at 294 K with B_{ext} = 0.75 T, is similar to that measured at 77 K with B_{ext} = 3.0 T (see figure 5.5) and can be analysed in the same way. The fit reveals a hyperfine field of 18.6 T and a quadrupole splitting of (-)0.35 mm/s. With increasing pressure we observe a decrease of the magnetic hyperfine fields, which can be tracked by the increase of the beat period in the time spectra. The damping of the beat structures can be explained by a concomitant increase of the quadrupole interaction since the random orientation of the two hyperfine interactions leads to a broadening of the $\Delta m = 0$ transition lines. This is best demonstrated in the spectrum at 50 GPa, where the simple magnetic beat pattern is already strongly modified. Going further up with pressure, there is a drastic change in the spectrum at 71 GPa, being now dominated by a quadrupole interaction with a period of 120 ns, corresponding to (-)0.74 mm/s splitting, and slightly modified by a magnetic site with a hyperfine field of about 10 T. The spectrum at 105 GPa arises solely from a quadrupole interaction with a beat period of 100 ns, corresponding to (-)0.87 mm/s splitting.

The non-magnetic origin of the beat pattern above 70 GPa is confirmed by NFS measurements without external field (see figure 5.8): the spectra up to 43 GPa show a complicated magnetic pattern whereas at 92 GPa and 105 GPa they have the same simple shape than with polarizing field. Additional studies with this pressure cell cooled down at 105 GPa in a closed-cycle He cryostat revealed the complete absence of magnetic interactions down to temperatures as low as 15 K. This NFS spectrum is shown at the bottom of figure 5.8 and indicated with a pressure of 115 GPa*. The pressure-increase at low temperatures depends on the special properties of the pressure cell (such as manufactured material, force generating mechanism or size). For this type of DAC and pressure range it was found to be about 10% [Rup99a] leading to an estimated

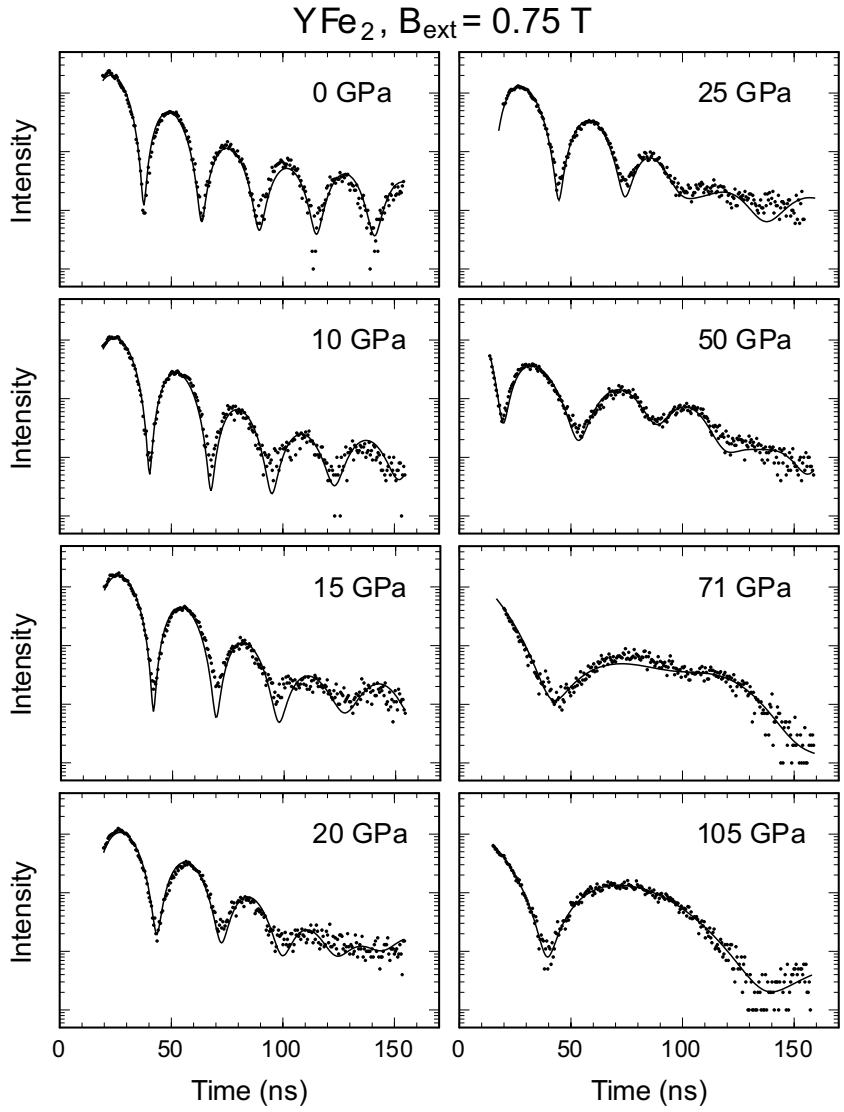

Figure 5.7: NFS spectra of YFe_2 at various pressures, measured at 294 K with an external field of 0.75 T. The solid lines are fits which are explained in the text.

pressure of 115 GPa at 15 K.

The numerical evaluation of the series of NFS spectra was made along the guidelines given in section 5.2, namely assuming a

1. small magnetic texture for the "unpolarized" spectra,
2. a random orientation of the quadrupole interaction with respect to the oriented magnetic hyperfine field for the polarized case,
3. a large thickness distribution of typically $d = 15 \pm 8$ μm.

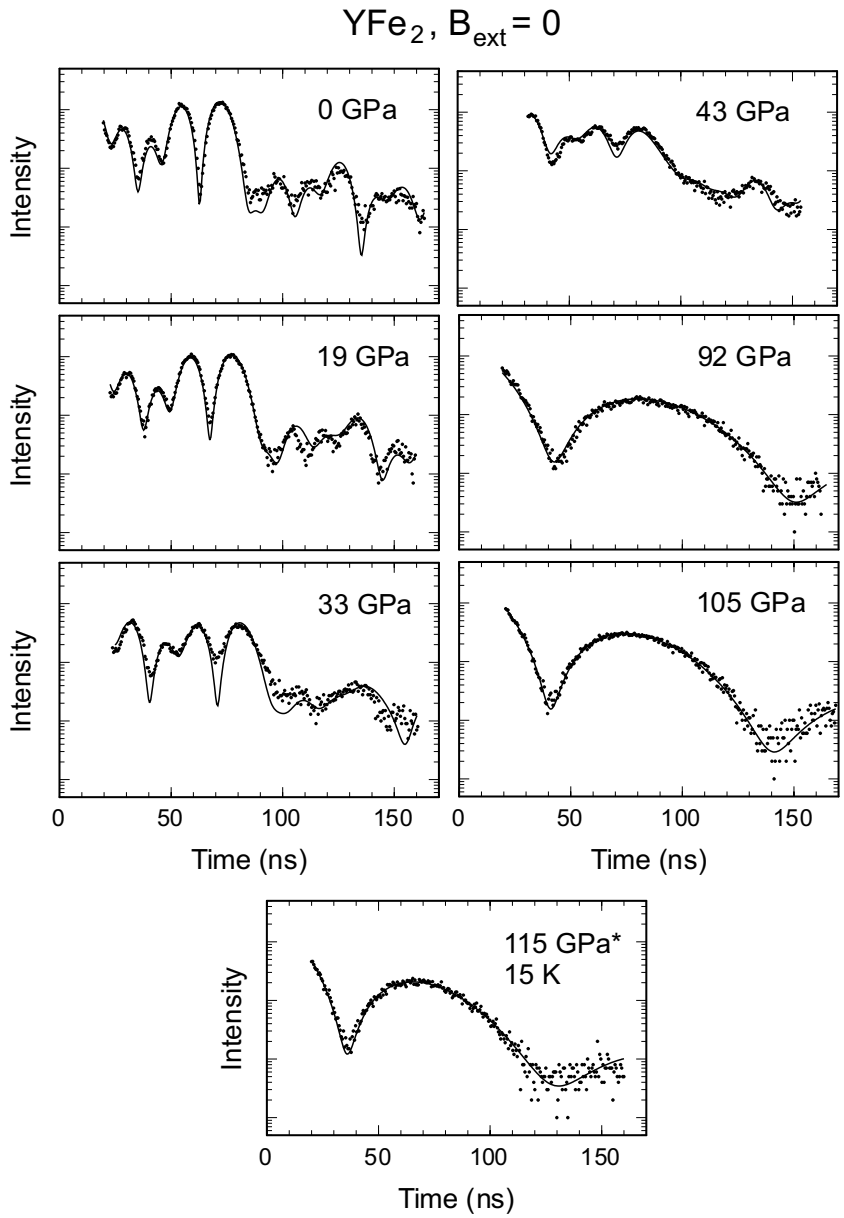

Figure 5.8: NFS spectra of YFe_2 at various pressures, measured without external field. The spectrum at 115 GPa* was measured in a cryostat system at 15 K. The corresponding pressure value is estimated from earlier experiments [Rup99a]. The solid lines are fits which are explained in the text.

4. At higher pressures the effects of a pressure gradient are adapted by the use of up to three magnetic sites with slightly different hyperfine fields B_{hf} and angles β.

5. For all subspectra the same isomer shift and quadrupole splitting was assumed.

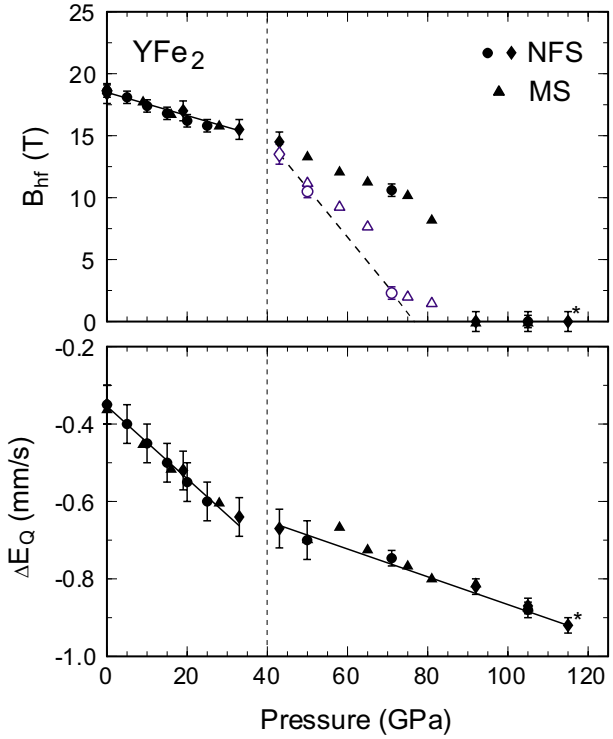

Figure 5.9: Experimental results for the magnetic hyperfine field (top) and quadrupole splitting (bottom) in YFe_2 obtained from the NFS spectra with (circles) and without (diamonds) external field. Full symbols for B_{hf} represent average values for all magnetic sites whereas open symbols stand for the total average, including also the non-magnetic sites. The "*" indicates the results for an estimated pressure of 115 GPa obtained at 15 K. For comparison the values from a Mössbauer study [Rup99a] are also given. The solid lines represent linear fits to the data in different pressure regimes divided by the vertical dashed line at 40 GPa.

The resulting values for the hyperfine fields B_{hf} and the quadrupole splitting ΔE_Q are shown in figure 5.9 together with corresponding results from a Mössbauer study [Rup99a]. Both data sets are in very good agreement.

The pressure dependence of B_{hf} exhibits a different behaviour in the range below and above 40 GPa. Below this point, B_{hf} shows a small linear pressure derivative of $-0.086(5)$ T/GPa ($d \ln B_{hf}/dp = -0.0046(5)\,GPa^{-1}$) which agrees with NMR studies at 4.2 K up to 1 GPa [DRM86] ($d \ln B_{hf}/dp = -0.0042(2)\,GPa^{-1}$). This slope increases drastically to -0.43(5) T/GPa at higher pressures as indicated by the dashed line in figure 5.9. This increase is induced by the appearance of a non-magnetic site in the NFS spectrum at 43 GPa (15%) which becomes dominant at 71 GPa (80%). However, the NFS spectrum at 50 GPa with external field could not be analysed with the occurrence of a non-magnetic site. Most probably, the influence of a non-magnetic site is hidden by the averaging procedure for the angle β and the thickness. The external

field may also induce a defined transferred hyperfine field at the non-magnetic site. Nevertheless, the mean value B_{av} agrees well with the corresponding value from MS at 50 GPa which is obtained in the same way including also the non-magnetic site. By extrapolating the pressure dependence to B_{av} = 0, a pressure of about 75 GPa is found where the magnetic ordering temperature is suppressed to room temperature.

The behaviour of the quadrupole interaction ΔE_Q shows also a change at 40 GPa. The linear decrease with $d\Delta E_Q/dP$ = -0.009(1) mm/s GPa in the low-pressure regime is reduced to -0.004(1) mm/s GPa at higher pressures.

Having in mind that the intermetallic compounds RFe_2 tend to prefer the hexagonal C14 structure at smaller volumes (see section 5.1), the above mentioned results suggest the occurrence of a structural phase transition C15 $\rightarrow$ C14 in YFe_2. Especially the appearance of a non-magnetic site above 40 GPa can be hardly explained in the framework of the cubic C15 structure with only one species of equivalent Fe sites. Indeed the XRD experiments by G. Reiss show additional lines in the diffraction pattern above 20 GPa which belong to the hexagonal C14 phase [Rei00].

5.3.2 $GdFe_2$

Two similar series of NFS spectra up to 105 GPa were taken for $GdFe_2$ with and without external field (see figures 5.10 and 5.11).

At a first glance, the spectra at low pressure are similar to those of YFe_2 and show a relatively simple beat pattern in the polarized case and a complicated pattern without external field. However, in contrast to YFe_2, the effective hyperfine field at the Fe nuclei is obtained by *adding* the external field of 0.75 T to the hyperfine field for the unpolarized case. This finding indicates that the Fe moment ($\mu_{Fe} = 1.6\,\mu_B$) is aligned antiparallel to the external field whereas the much larger Gd moment is aligned parallel to minimize the potential energy. Hence, the applied field confirms the ferrimagnetic ordering type in $GdFe_2$.

For higher pressures up to 53 GPa one observes an increased damping of the magnetic beat pattern similar to YFe_2. Going further to pressures above 71 GPa, the NFS spectra show a more pronounced pattern again. Since this pattern, especially at 105 GPa, has no longer the uniform shape as at low pressures, a principle change of the magnetic behaviour can be deduced. Unambiguously, the sequence of NFS spectra demonstrates that $GdFe_2$ remains magnetically ordered well above 300 K in the whole pressure range.

The evaluation of the NFS spectra was performed in analogy to YFe_2, but considering the differences due to the ferrimagnetic ordering and an unknown easy magnetization direction in the unpolarized sample (see section 5.1.2) by the following constraints:

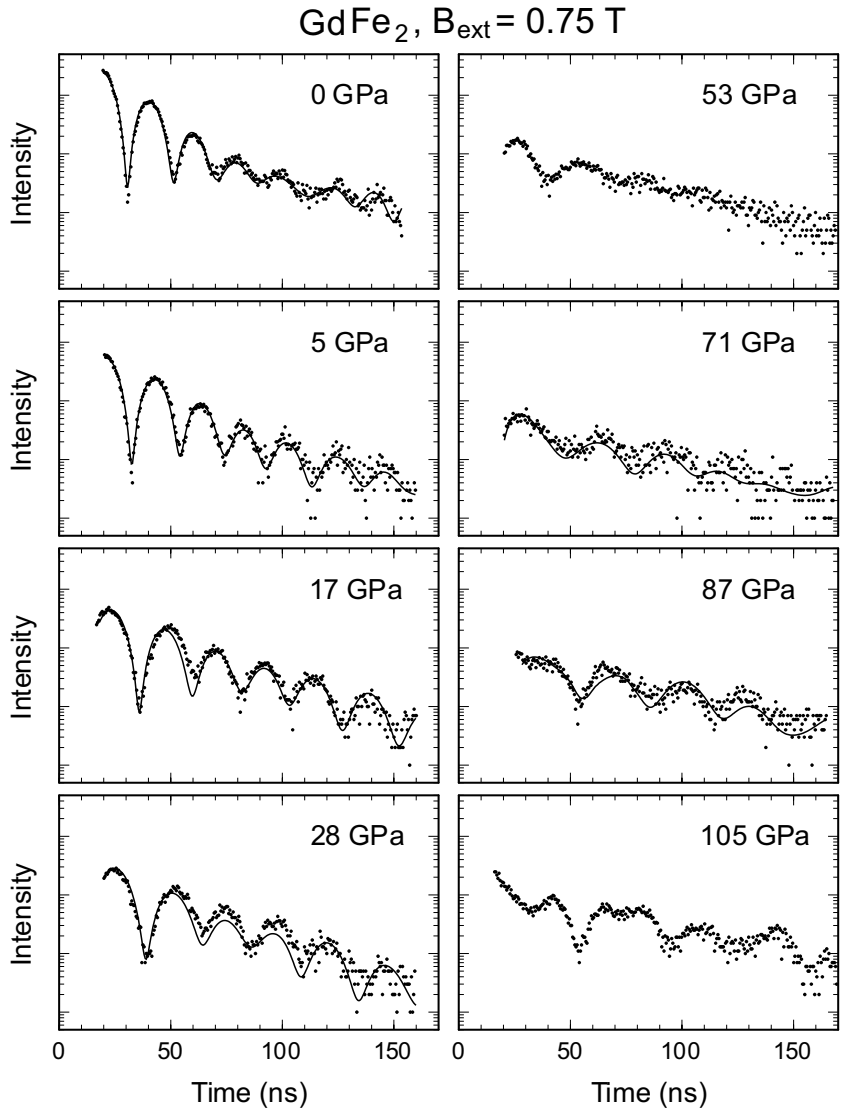

Figure 5.10: NFS spectra of $GdFe_2$ at various pressures, measured at 294 K with an external field of 0.75 T. The solid lines are fits which are explained in the text.

1. Since the magnitude of the external field is weak, it is supposed not to disturb the ferrimagnetic ordering type throughout the high-pressure series. Therefore, the value of B_{ext} is always subtracted from the measured effective hyperfine fields.

2. The unpolarized spectra are fitted with 4 magnetic sublattices having different angles β between hyperfine field and main axis of the EFG in the range 25 – 80°. Free parameters are the relative weight of the sublattice and the respective hyperfine field B_{hf}.

3. Due to the lack of a defined direction of the magnetization axis and the large

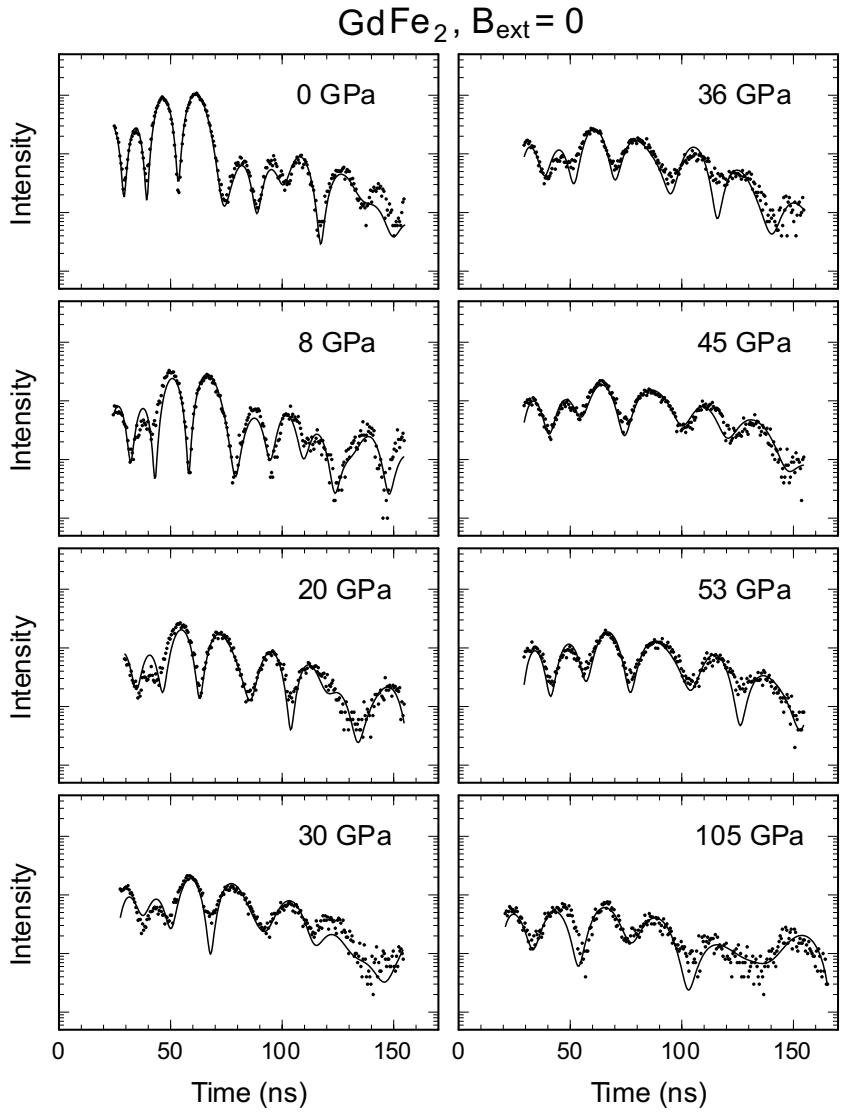

Figure 5.11: NFS spectra of $GdFe_2$ at various pressures, measured without external field. The solid lines are fits which are explained in the text.

number of free parameters introduced in the previous point, the spectra are fitted without the assumption of a magnetic texture.

The numerical results for B_{av} and ΔE_Q are plotted in figure 5.12. Again, both hyperfine parameters indicate a drastic change of the magnetic and/or structural properties at a certain transition pressure, here 53 GPa. The low-pressure region up to 20 GPa is characterized by a linear decrease of B_{av} with $dB_{av}/dP = -0.175(10)$ T/GPa. Between 20 and 53 GPa, the slope is slightly smaller before the value of B_{av} drops from 14.7 T at 53 GPa to 11.1 T at 71 GPa. Beyond this jump a modest linear decrease is observed with $dB_{av}/dP = -0.035(10)$ T/GPa reaching 9.9 T at 105 GPa.

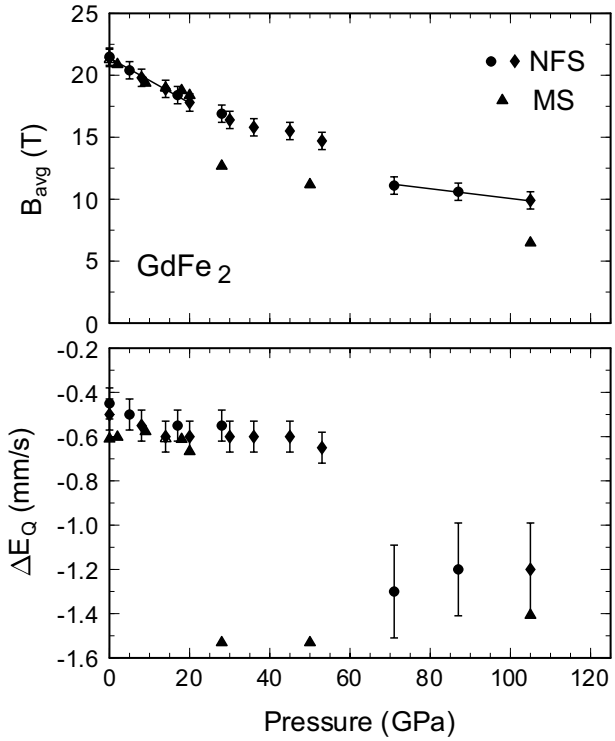

Figure 5.12: Experimental results for the averaged magnetic hyperfine field B_{av} (top) and quadrupole splitting ΔE_Q (bottom) in $GdFe_2$ obtained from the NFS spectra with (circles) and without (diamonds) external field. For comparison the values from a Mössbauer study [Lu00] are also presented (triangles), including preliminary results above 20 GPa. The solid lines represent linear fits to the data of B_{av} in different pressure regimes.

The quadrupole splitting ΔE_Q shows no pronounced pressure dependence up to 53 GPa. Above 53 GPa, however, the spectra can only be modeled with a drastically increased electric field gradient with ΔE_Q = -1.3(2) mm/s at 71 GPa.

The agreement with results from MS [Lu00] is very good for pressures below 20 GPa. At higher pressures the MS results indicate also a drastic change of the magnetic properties: a drop of the average hyperfine field and a sharp increase of the EFG. However, the transition pressure lies between 20 and 28 GPa whereas for NFS it is above 50 GPa. This discrepancy is not due to uncertainties in the pressure determination, because the experiments at 28 GPa, 50 GPa and 105 GPa were performed on the same sample for MS and NFS. The differences could be explained when the observed transition shows a time-dependence: The NFS experiments were carried out within 1-2 hours after the adjustment and calibration of a new pressure while the MS experiments were performed within 1-2 months afterwards.

In analogy to YFe_2 the drastic changes of the hyperfine parameters may be caused by a structural transformation from the C15 to the C14 phase. Complementary XRD experiments revealed diffraction patterns with hexagonal classification at high pressure, here again above 50 GPa [Rei00], as found also in the NFS studies. This structural transition was observed in a completely independent high-pressure run. The XRD experiments were carried out in a 30-60 min time scale, which is comparable to the NFS studies. Comparison of XRD and NFS with the MS results demonstrates that the C15 $\rightarrow$ C14 transition is slow, at least at 300 K.

5.3.3 $TiFe_2$

The effect of pressure and temperature on the magnetic properties of hexagonal $TiFe_2$ (C14) was studied with conventional MS up to 20 GPa [LHZ96]. For the series of NFS experiments $TiFe_2$ was measured at ambient pressure and various temperatures as a reference sample for antiferromagnetic ordering with a non-magnetic 2a site. According to the ordering temperature $T_N \leq 285\ K$ [LHZ96] the NFS spectrum at 294 K shows no magnetic beat pattern (figure 5.13). The evaluation of the magnetic spectrum at 20 K revealed the same set of parameters as the mentioned MS experiments: (i) a magnetic (6h) and a non-magnetic (2a) site in the ratio 3:1, (ii) a hyperfine field of 9.4 T for the 6h sites, (iii) a quadrupole splitting ΔE_Q = -0.4 mm/s, (iv) two angles $\beta_{6h} = 90°$ and $\beta_{2a} = 0°$ and (v) an asymmetry parameter $\eta = 0.4$ for the 6h sites.

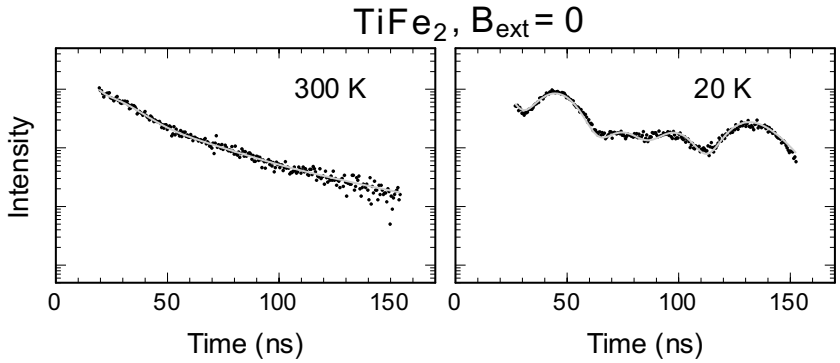

Figure 5.13: NFS spectra of $TiFe_2$ at ambient pressure for 294 K and 20 K measured without external field. The solid lines are fits which are explained in the text.

5.3.4 $ScFe_2$

In $ScFe_2$ with hexagonal C14 structure a series of NFS spectra was measured up to 51 GPa. Since the magnetization in $ScFe_2$ does not saturate up to about 4 T [NY86] the sample could not be fully polarized with the available external field of 0.75 T and

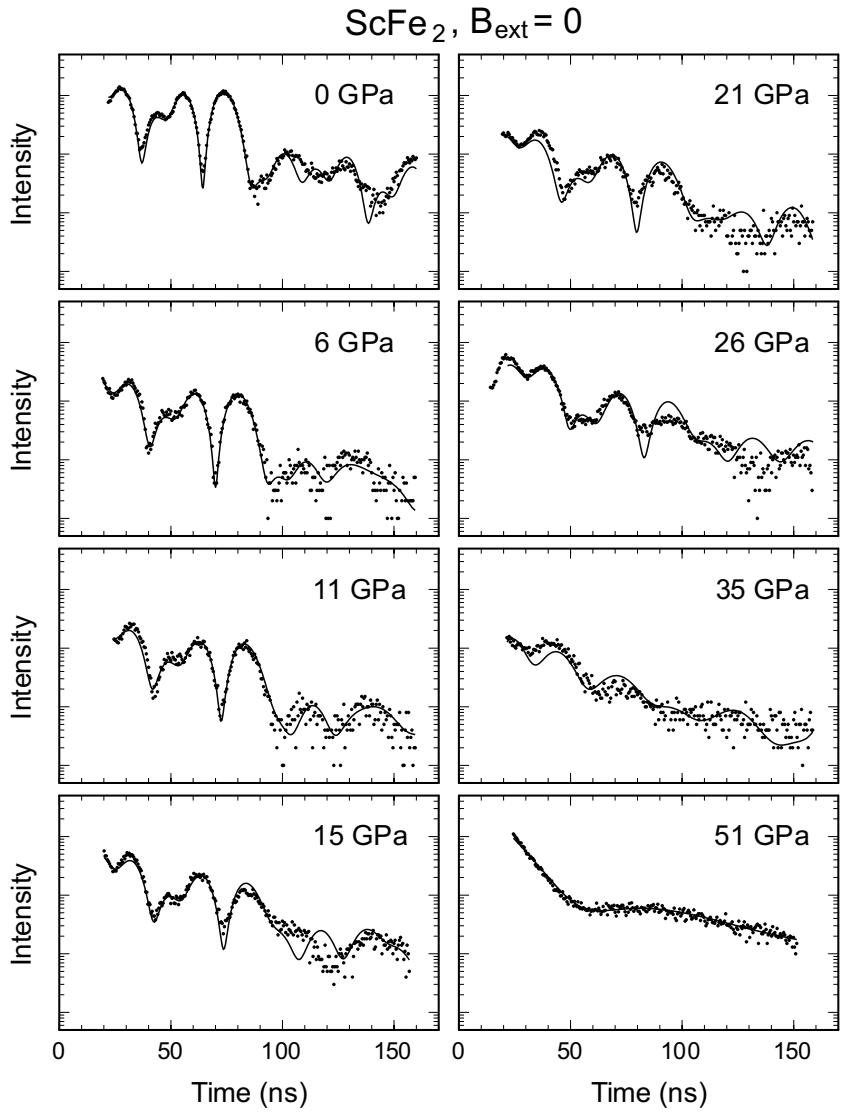

Figure 5.14: NFS spectra of $ScFe_2$ at various pressures, measured at 294 K without external field. The solid lines are fits which are explained in the text.

the NFS spectra are recorded only without external field (figure 5.14). The spectrum at ambient pressure exhibits the familiar shape with two pronounced beatings around 50-80 ns, indicating a well-defined hyperfine field at all Fe sites. At higher pressures a strong decrease of the magnetic hyperfine fields is observed. Above 26 GPa the beat pattern changes drastically and the spectrum at 51 GPa indicates the absence of magnetic order at 294 K. The minimum is caused by thickness effects.

The spectra are fitted according to the hexagonal structure of $ScFe_2$ with two subspectra in a ratio 3:1 representing the 6h and 2a sites with $\beta_{6h} = 90^\circ$ and $\beta_{2a} = 0^\circ$ (see section 5.1.2). Due to the small influence of the quadrupole interaction ΔE_Q on the

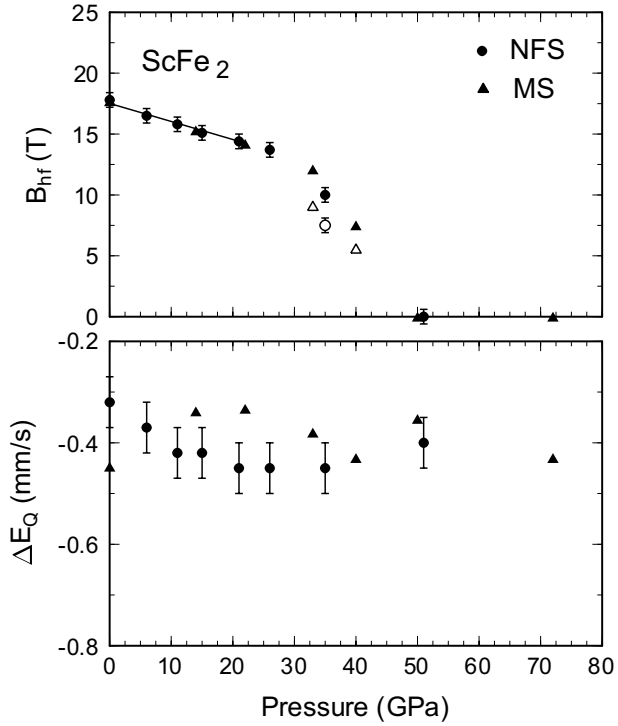

Figure 5.15: Experimental results for the magnetic hyperfine fields B_{hf} (top) and quadrupole splitting ΔE_Q (bottom) in $ScFe_2$ obtained from the NFS spectra at 294 K. Full symbols for B_{hf} represent average values for all magnetic sites. The open symbols stand for the total average, including also the non-magnetic 2a sites. For comparison the values from Mössbauer studies [Lu00, Rup99a] are also given (triangles). The solid line represents a linear fit to the data in the low pressure regime.

NFS spectra, this parameter was chosen to be identical for both sites. In order to obtain a reasonable modeling of the data, a relatively strong magnetic texture has to be considered (35%). For pressures above 21 GPa a distribution of hyperfine fields with a width of 2% (21 GPa) to 5% (35 GPa) of the mean value was assumed. The results for ΔE_Q and the magnetic hyperfine fields B_{hf} are plotted in figure 5.15.

At ambient pressure, the 6a and 2a sites show the same hyperfine field B_{hf} of 17.7 T. The low-pressure region up to about 20 GPa is characterized by a linear decrease of B_{hf} following $dB_{hf}/dP = -0.160(10)\,T/GPa$, identical for both sites. At 35 GPa the hyperfine field of the 2a sites drops to zero whereas the field at the 6h sites is reduced to about 10 T. This behaviour is similar to the situation in $TiFe_2$ and indicates a pressure-induced transition of the ordering type in $ScFe_2$ from ferro- to antiferromagnetism exhibiting a reduced hyperfine field at the 6h sites and a non-magnetic 2a site.

This decrease of the magnetic hyperfine fields is not simply due to a decrease of the ordering temperature T_m, i.e. an increase of T/T_m. This is proved by additional experiments at high pressure *and* low temperature, which reflect a decrease of the magnetic

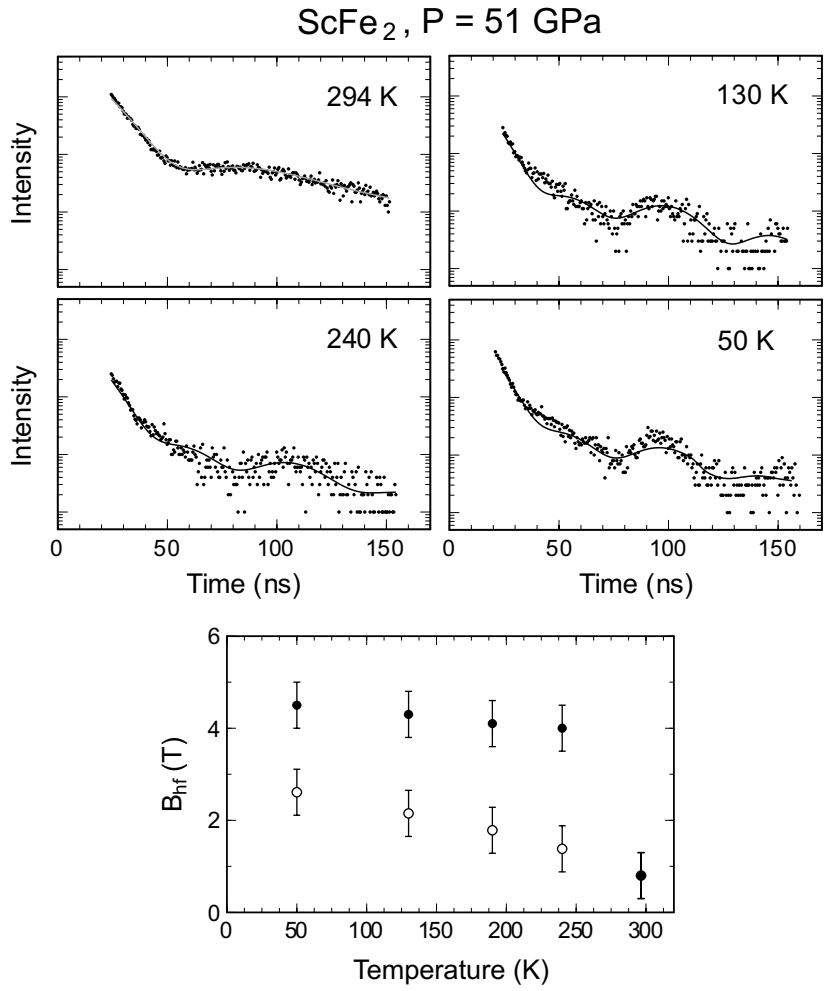

Figure 5.16: (top) NFS spectra of $ScFe_2$ at 51 GPa* and various temperatures, measured without external field. The solid lines are fits which are explained in the text. (bottom) Corresponding results for the magnetic hyperfine fields $B_{\rm hf}$. Full symbols represent average values for all magnetic sites. The open symbols stand for the total average, including also the non-magnetic 2a sites.

Fe moment. [5] Figure 5.16 shows NFS spectra at 51 GPa* and various temperatures down to 50 K. [6] The "slow" beat pattern at 50 K reveals a value of $B_{\rm hf}$ = 4.5 T. Following the linear relation between $B_{\rm hf}$ and μ_{Fe} in [BCK90], this hyperfine field corresponds to $\mu_{Fe} = 0.3\mu_B$. The evaluation could not be performed with a fixed ratio of 3:1 for the two subspectra, but revealed a coexistence (ratio about 1:1) of a magnetic and a non-magnetic site (as observed in $TiFe_2$).

[5] Mössbauer studies at 77 K indicate a reduction of $B_{\rm hf}$ from 19.7 T at 0 GPa to 10.4 T at 40 GPa [Rup99a]. This corresponds to a moment reduction from 1.3 μ_B to 0.7 μ_B.

[6] The pressure of 51 GPa* was measured at 294 K. Similar to the experiments with YFe_2 at 15 K, the "*" indicates the occurence of a pressure increase at low temperatures, estimated to be 10% at 50 K.

5.3.5 Measurement of Isomer Shifts

The objective of this section is to demonstrate the feasibility of measuring isomer shifts S with the ^{57}Fe resonance using a reference sample as introduced in chapter 5.3.5. The knowledge of S gives information on the electronic charge density at the nucleus, a higher charge density leads to a smaller S. An ideal reference sample should exhibit a relatively sharp single nuclear resonance and an effective thickness comparable to the effective thickness per resonance line of the sample.

During the different runs of NFS experiments several attempts have been made to measure the isomer shift of YFe_2 at different pressures with an enriched $K_4Fe(CN)_6$ reference (powder) sample, embedded in paraffin. Although this reference provides a sharp single resonance line and an adjustable thickness, the NFS spectra of the combined samples could not be analysed: the random thickness distribution of both sample *and* reference leads to undefined experimental conditions.

Stainless steel foils with uniform geometrical thickness were available for us only in non-enriched form and their use as a reference sample is therefore hampered by the strong electronic absorption; for instance a 50 μm (25 μm) thick foil has an effective thickness of $\chi = 15$ (7.5) and an absorption of more than 90% (70%) at 14.4 keV.

Three examples of isomer shift measurements are shown in figure 5.17a for YFe_2 at 0 GPa, 25 GPa and 92 GPa measured together with stainless steel absorbers ($B_{ext} = 0.75\ T$ for 0 and 25 GPa). The spectrum at 92 GPa was obtained in the last run at ESRF (April 1999) using focusing optics (see 4.1.3) and an already prepared DAC from MS studies performed in Paderborn [Rup99a]. For the fits of the NFS spectra the results from accompanying measurements of the pure YFe_2 sample and the stainless steel foils are combined with the isomer shift as the only free parameter. The fitted values for the isomer shift of YFe_2 relative to stainless steel are 0.03(4) mm/s, -0.21(4) mm/s and -0.51(4) mm/s for 0, 25 and 92 GPa. It should be mentioned that the sign of S can not be determined definitely from NFS alone. For YFe_2 at 0 GPa the positive sign was confirmed by conventional MS whereas the negative sign at 25 and 92 GPa follows from the well-known negative pressure derivative of S (describing an increase of the s-electron density with reduced volume).

Once the sign of S is fixed, the combined spectrum of YFe_2 at 25 GPa and the stainless steel absorber provides the possibility to determine the (negative) sign of the EFG with NFS. This special case is due to the fact that the asymmetry of the energy spectrum at 25 GPa (see right panel of figure 5.17a) is governed by the sign of the EFG providing a clear distinction between positive and negative values. Furthermore, this energy spectrum at 25 GPa demonstrates, when compared with the spectrum at 0 GPa, the increase of ΔE_Q and the decrease of B_{hf} (see figure 5.9).

The results for S are plotted in figure 5.17b relative to the isomer shift at ambient pressure; they agree quite well with values from MS [Rup99a]. The accuracy for the measurement of isomer shifts with NFS depends very much on the specific combination of

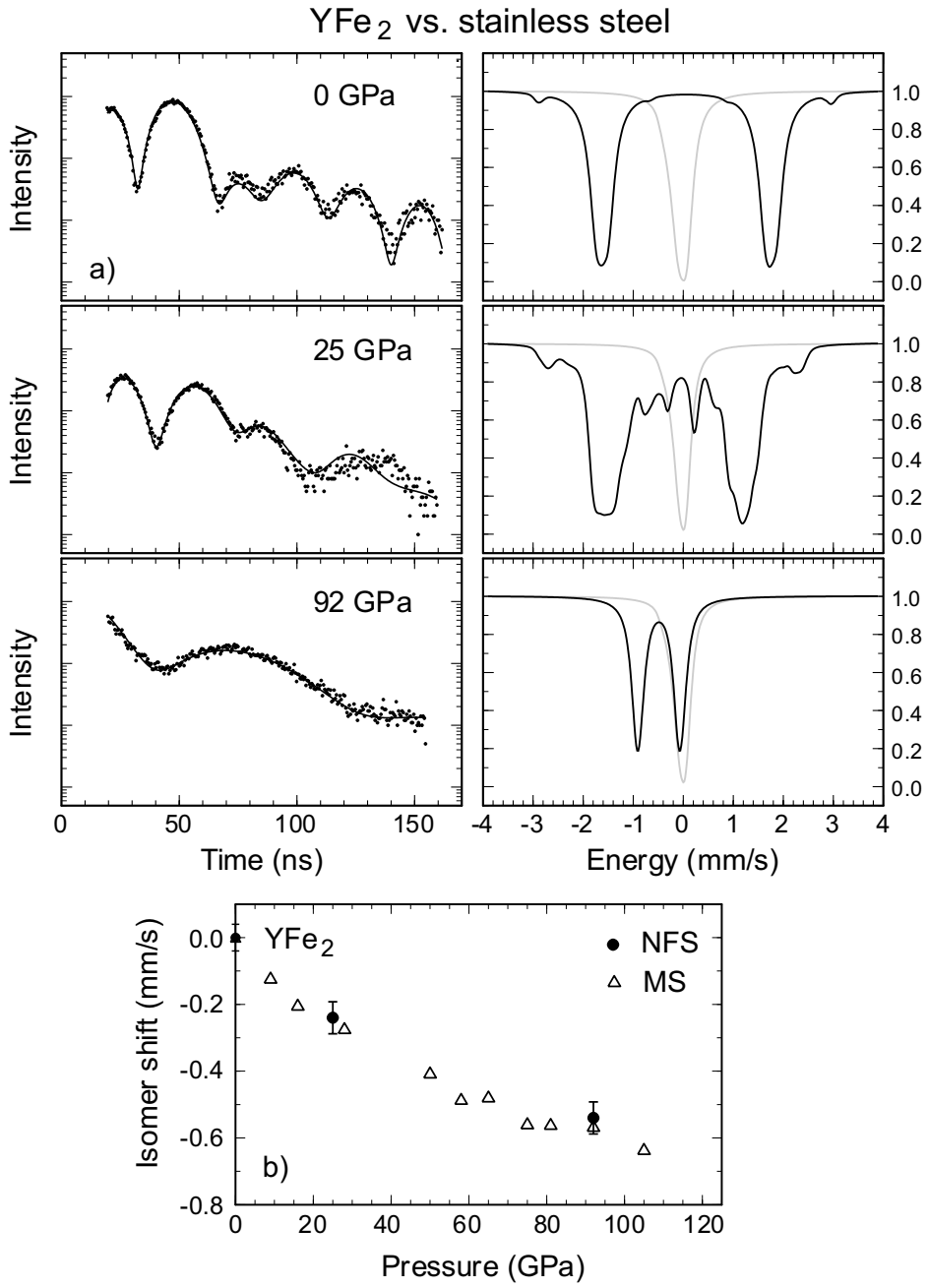

Figure 5.17: (a) NFS spectra of YFe_2 measured together with stainless steel (SS) as reference sample. For details of the fits, see text. The corresponding energy spectra are shown in the right panel with stainless steel (grey line) set to zero. (b) Results for the isomer shift of YFe_2 from these NFS spectra (circles). For comparison with the results from MS [Rup99a] (triangles) the values for both series are given relative to the respective isomer shift at ambient pressure. The uncertainty of the MS results is estimated to 0.01 mm/s [Rup99b].

sample and reference. It improves significantly with the number of beating periods in the time spectrum caused by the energy difference of the nuclear resonances in sample and reference. This is strikingly demonstrated by experiments with the ^{151}Eu resonance, where a large difference of about 10 mm/s between the two valence states Eu^{2+} and Eu^{3+} and a corresponding beating period of 6 ns in the time window of 100 ns allows a precise determination of isomer shifts [PLS99]. For the case of ^{57}Fe with rather small differences in *S*, the precision could be enhanced by NFS measurements in a longer time window.

5.4 Discussion

In this section we discuss the pressure-induced changes of the magnetic ordering behaviour and Fe moment formation in the investigated Laves phases. Figure 5.18 summarizes, as a function of the Fe-Fe distance d_{Fe-Fe}, the NFS results for the magnetic ordering temperatures T_m and the averaged hyperfine fields B_{av} of YFe_2, $GdFe_2$, and $ScFe_2$. In addition, T_m values for YFe_2 from a XRD study of the magnetovolume anomaly [Rei00], and T_m and B_{hf} values from MS on $TiFe_2$ [LHZ96] are presented. The structural transformations from C15 to C14 are indicated by vertical dashed (YFe_2) and dashed-dotted ($GdFe_2$) lines [Rei00].

All the present RFe_2 systems show a considerable decrease of the magnetic hyperfine fields and, concomitantly, of the magnetic Fe moments.[7] In table 5.2 the volume coefficients $\Gamma_{B_{hf}} := -d\ln B_{hf}/d\ln V$ at low pressure are listed for the present RFe_2 compounds[8], indicating that the initial moment reduction becomes more pronounced at smaller d_{Fe-Fe} spacings going from YFe_2 to $ScFe_2$ and $TiFe_2$. For YFe_2 and $ScFe_2$ the moment reduction is accelerated at higher pressures reaching a coexistence of a low-moment and a non-magnetic state. The latter properties are very similar to those of $TiFe_2$ at ambient pressure and low temperatures [LHZ96] and can be attributed to the hexagonal C14 structure with antiferromagnetic ordering between Fe atoms in neighbouring 6h planes and non-magnetic Fe atoms in the intermediate 2a sites.

The volume coefficients $\Gamma_{T_m} := -d\ln T_m/d\ln V$ of the magnetic ordering temperature at ambient pressure are presented in the last column of table 5.2.[9] Regarding the behaviour at higher pressures in figure 5.18, the continuous variation of T_m in YFe_2 is of particular interest: T_m increases, despite the moment reduction, from $T_C = 535\,K$ at ambient pressure (d_{Fe-Fe} = 2.60 Å) to 660 K at 15 GPa (2.52 Å) and then drops to 294 K around 75 GPa (2.34 Å) and finally to below 15 K at 115 GPa (2.27 Å). This pressure dependence is illustrated in figure 5.18a by a dashed line.

Similar volume effects on T_C and μ_{Fe} are observed for "negative pressure" in hydrogenated YFe_2 [BD76]. In isostructural YFe_2H_4 with an 8% increase of the lattice parameter, the ordering temperature is lowered to 308 K, whereas the iron moment is enhanced by 25% from $1.45\,\mu_B$ to $1.83\,\mu_B$. This topic is discussed in more detail in the next subsection.

Among the studied RFe_2 systems, $ScFe_2$ represents the link between YFe_2 and $TiFe_2$. The properties of $ScFe_2$ at ambient conditions, hexagonal structure and ferromagnetic ordering, are approached by YFe_2 at pressures of about 20 GPa (2.50 Å). With further decreasing $Fe-Fe$ distance both YFe_2 and $ScFe_2$ become antiferromagnetic ($d_{Fe-Fe} =$

[7] Precise values for the moment reduction were obtained from additional MS studies at low temperatures [Rup99a].

[8] The negative sign in the definition of $\Gamma_{B_{hf}}$ (and later Γ_{T_m}) provides the same sign of pressure and volume coefficients

[9] Γ_{T_m} is also called the *magnetic Grüneisen parameter*.

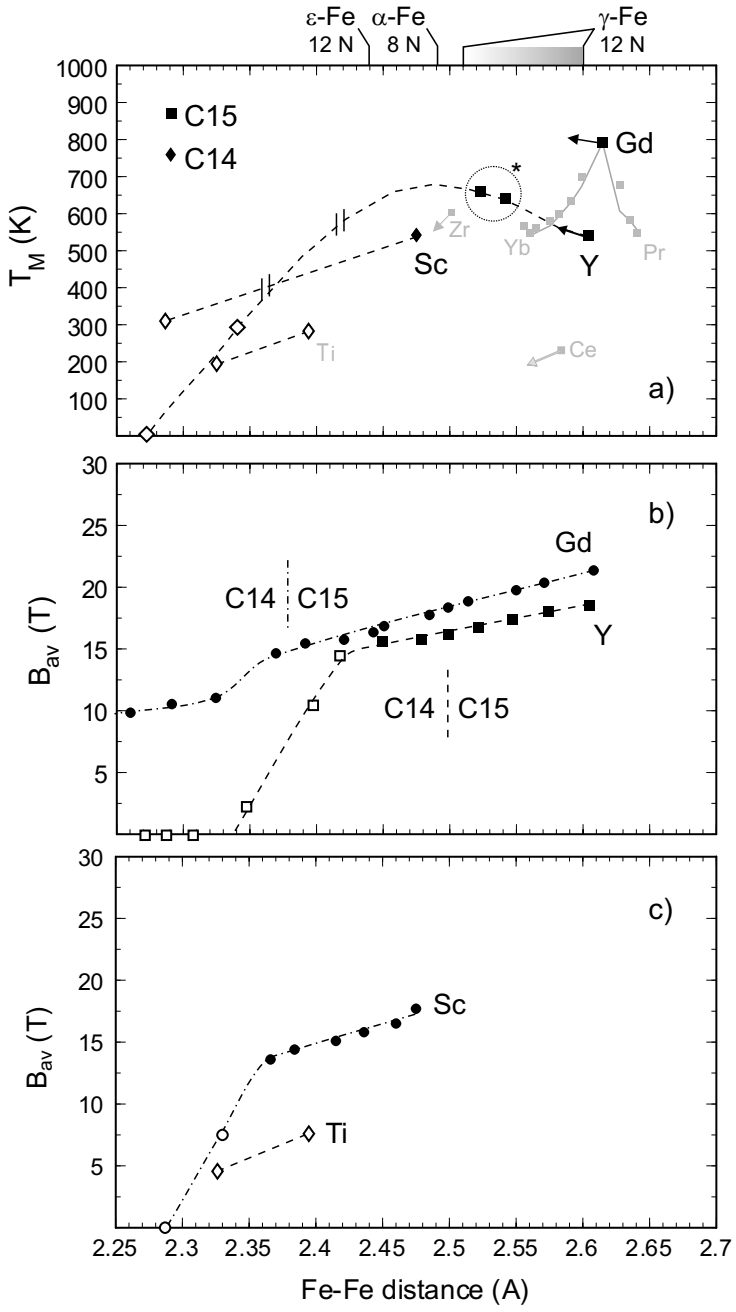

Figure 5.18: Summary of NFS results for the magnetic ordering temperature T_m and averaged hyperfine fields B_{av} at 294 K ($TiFe_2$ at 78 K) as presented in the previous sections. Full symbols are for fm ordering and open symbols for afm ordering. The two T_C values for YFe_2 marked with "*" were obtained from XRD experiments measuring the magneto-volume anomaly [Rei00]. All compressibilites and the C15 $\rightarrow$ C14 phase transition for YFe_2 and $GdFe_2$ (vertical dashed and dashed-dotted lines in (b), respectively) were provided by G. Reiss [Rei00].

	d_{Fe-Fe} (Å)	μ_{Fe} (μ_B)	T_m (K)	K_0 (GPa)	dB_{hf}/dp (T/GPa)	$\Gamma_{B_{hf}}$	dT_m/dp (K/GPa)	Γ_{T_m}
YFe_2	2.60	1.45	535	133	-0.086(5)	-0.61(3)	6^a	1.5
$GdFe_2$	2.61	1.6	790	104	-0.175(10)	-0.84(3)	3^a	0.4
$ScFe_2$	2.48	1.4	542	153	-0.160(10)	-1.38(3)	-	-
$TiFe_2$	2.39	0.7	285	193	-0.258^b	-5.30	-3^b	-2.0
α-Fe	2.49	2.2	1043	168	-0.055^c	-0.3	0^c	0

Table 5.2: Magnetic properties of *RFe* compounds and α-Fe at ambient pressure; $\Gamma_{B_{hf}} := -d\ln B_{hf}/d\ln V$, $\Gamma_{T_m} := -d\ln T_m/d\ln V$. The pressure and volume coefficients of B_{hf} are for room temperature, except $TiFe_2$ (78 K). References: d_{Fe-Fe} and K_0 are from [Rei00], μ_{Fe} and T_m from [BCK90], ^{a} from [BBM74], ^{b} from [LHZ96], ^{c} from [WBI72].

2.35 – 2.40 Å) and are finally transformed to a non-magnetic state at $d_{Fe-Fe} \approx 2.30 -$ 2.35 Å. For YFe_2 the latter finding is verified by low-temperature experiments at 115 GPa.

Thus, the complete variety of magnetic properties in RFe_2 systems with non-magnetic constituents *R* can be reproduced in a single compound, namely YFe_2, by the application of external pressure. This means that the $Fe-Fe$ distance d_{Fe-Fe} is a universal parameter for the iron magnetism in RFe_2. This even holds for the structural phase transformation C15 → C14 with decreasing d_{Fe-Fe}.

A different behaviour is observed in $GdFe_2$ which also exhibits the C15 → C14 transition but remains magnetically ordered well above room temperature up to the highest pressures. This is clearly caused by the magnetic Gd sublattice; details are discussed in section 5.4.2.

5.4.1 Volume Dependence of Magnetic Ordering Temperatures T_m

According to a survey on band structure theory of magnetism in 3d-4f compounds by M. Richter [Ric98a], the theoretical treatment of Curie temperatures is one of the most demanding tasks in the field of *first principles* theories of magnetic properties.[10] Beside the principal problems of electronic band structure calculations delivering only ground state properties at T = 0 K, physical intuition is needed to parameterize the relevant excitations at elevated temperatures: (i) single-particle spin-flip Stoner excitations and (ii) collective spin fluctuations, which are of many-particle nature. The importance of spin fluctuations is reflected by the fact that the energy of a Stoner excitation is equal to the exchange splitting Δ. In pure Fe, however, this splitting (1.8 eV) is far too large

[10] A recent theoretical study of Y-Fe compounds revealed a T_C of 650 K for YFe_2 at ambient pressure [SJ98] which is about 20% higher than the experimental value of 535 K.

to explain the measured Curie temperature of 1043 K. Whereas the Stoner theory with the parameter I explicitely includes only intraatomic exchange (which leads to the exchange splitting Δ), the energy spectrum of collective spin fluctuations depends mainly on interatomic interaction between neighbouring spins.

In this section the main pressure effects on the intra- and interatomic interactions and their influence on the magnetic ordering temperatures are discussed. Two "classical" models are presented, which describe these effects on magnetic ordering temperatures in magnetic 3d systems.

The most obvious pressure effect in transition metal compounds is the enhanced overlap of neighbouring 3d wave functions. Following Heine's band structure calculations [Hei67], this leads to an increased 3d bandwidth

$$W \propto d^{-5} \ , \tag{5.3}$$

where d is the interatomic distance. Furthermore, the concomitant lowering of $D(E_F)$ induces a reduction and, finally, a suppression of the magnetic moment μ_{Fe}. For RFe_2 systems, this effect is directly reflected by the decrease of the magnetic hyperfine fields with decreasing volume (see table 5.2 and figure 5.18b). Since the energy gain due to the spin polarization of the Fe 3d band is proportional to μ_{Fe}^2 (see equation 5.1), the moment reduction should destabilize the magnetically ordered phase and, therefore, result in a decrease of T_C. This is also suggested by the mean-field approach in equation 5.2, which simplifies for pure Fe magnetism to

$$3\,k_B\,T_C \;=\; 2\,a_{FeFe} = 6\,A_{FeFe}\,S_{Fe}\,(S_{Fe}+1) \tag{5.4}$$

$$\Rightarrow \quad T_C \;\propto\; A_{FeFe}\,\mu_{Fe}^2 \ . \tag{5.5}$$

Interestingly, the opposite behaviour is observed for YFe_2, namely an increase of T_C from 535 K at 0 GPa to 660 K at 15 GPa. This result can be explained by a pressure-induced increase of the interatomic coupling A_{FeFe} between the Fe moments, which overcompensates the effect of moment reduction. Using the simple formula 5.5 and assuming the same volume dependence for μ_{Fe} and B_{hf} (table 5.2) one obtains a rough estimation for the increase of A_{FeFe} in YFe_2 at ambient pressure:

$$\Gamma_{T_C} \;=\; -\,\frac{d\,\ln A_{FeFe}}{d\,\ln V} \;-\; 2\,\frac{d\,\ln \mu_{Fe}}{d\,\ln V} \tag{5.6}$$

$$\Rightarrow \quad -\,\frac{d\,\ln A_{FeFe}}{d\,\ln V} \;=\; \Gamma_{T_C} \;-\; 2\,\Gamma_{B_{hf}} \;\approx\; 2.7 \tag{5.7}$$

For higher pressures, one has to take into account that the magnetic 3d moments couple via direct exchange with overlapping electronic orbitals. From the Pauli exclusion principle, it is obvious that parallel alignment of neighbouring spins must become unfavourable at high compression. Consequently, the exchange energy and T_C tend to decrease at higher pressures leading to an antiferromagnetic state.

Bethe-Slater Curve

A qualitative discussion of the pressure effect on the exchange coupling and T_C is given in the literature in terms of the Bethe-Slater curve (figure 5.19). Here, an interatomic exchange interaction between two *localized moments* is expressed by the interaction parameter J as a function of $d_{Fe-Fe} - 2r_{3d}$, where r_{3d} is the mean 3d-shell radius at ambient pressure. Barbara et al. [BGG73] interpreted their results on dT_C/dp in YFe_2 (5 K/GPa), Y_6Fe_{23} (0.1 K/GPa) and R_2Fe_{17} (-9.8 K/GPa) by the distance dependence of the exchange interaction along this curve.

The similarity between the shape of the Bethe-Slater curve and the T_C dependence of YFe_2 in figure 5.18a suggests that this intuitive interpretation can be extended to the present results which are obtained for YFe_2 just by the application of external pressure. Since the Bethe-Slater curve is based on the presence of localized magnetic moments, this implies that the Fe band moment in YFe_2 at low pressures exhibits a high degree of localization. With increasing interatomic interaction at high pressures, reflected by the suppression of μ_{Fe}, the picture of localized moments is not valid any more. The following model takes the band character of the 3d moment into account.

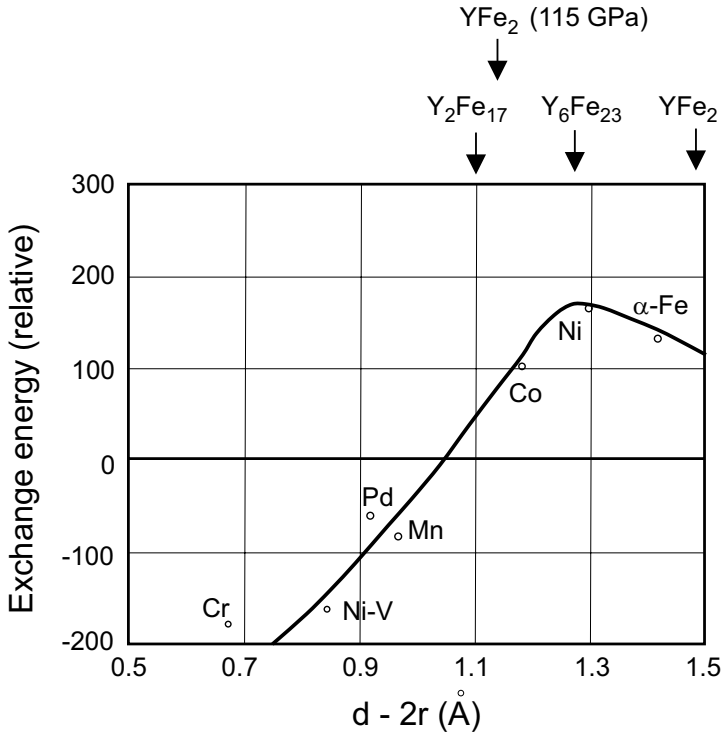

Figure 5.19: Bethe-Slater curve describing the distance dependence of the exchange interaction with Fe-Fe distance d_{Fe-Fe} and $r_{3d} = 0.55$ following [BGG73]. The position of various iron compounds is marked by arrows. Further information on the Bethe-Slater curve can be found in [Jil91, BCK90].

Wohlfahrt Model

A more quantitative description of the pressure effect on T_C was introduced by Wohlfahrt [Woh81, WW81, BBM74] based on the Stoner-Wohlfahrt theory of *itinerant ferromagnetism*. Neglecting the influence of the sp-band, T_C is assumed to be proportional to the so-called degeneracy temperature T_F which depends on the shape of the electron density of states $D(E)$ at the Fermi energy:

$$T_C^2 = T_F^2 \, (\bar{I} - 1). \tag{5.8}$$

With the abbreviation $\bar{I} = I \cdot D(E_F)$, including I and $D(E_F)$ from the Stoner criterion, $\bar{I} > 1$ leads again to ferromagnetism.

As elaborated in [Woh81] the following pressure dependence can be derived from equation 5.8 using the compressibility κ:

$$\frac{d\,T_C}{d\,p} \;=\; \frac{5}{3}\,\kappa\,T_C \;-\; \kappa\,\frac{\alpha}{T_C} \tag{5.9}$$

$$\text{where} \quad \alpha \;=\; \frac{5}{6}\,\frac{I}{I_b}\,T_F^2\,. \tag{5.10}$$

or in terms of volume:

$$\Gamma_{T_C} \;=\; \frac{5}{3} \;-\; \frac{\alpha}{T_C^2}, \tag{5.11}$$

Here, I is the effective and I_b the bare intraatomic interaction between the itinerant electrons ($I/I_b < 1$). The main assumptions for the derivation of equation 5.9 are a proportional relationship of T_F and bandwidth W under pressure as well as an electron density of states $D(E_F) \propto 1/W$.

The first term on the right-hand side in equation 5.9 is proportional to T_C and hence dominant for ferromagnets with high T_C. This is the case for YFe_2 at ambient pressure, where $5/3\,\kappa T_C = 6.7\,\text{K/GPa}$ is close to the experimental value of $d\,T_C/d\,p = 6\,\text{K/GPa}$ [BB73]. The corresponding value for α is about $(220\,\text{K})^2$. However, the overall pressure dependence for YFe_2 (with negative Γ_{T_C} for relative volumes $V/V_0 \leq 0.85$) can not be described with a constant value for α. According to equation 5.11, the volume coefficient Γ_{T_C} changes its sign, when α approaches a critical value

$$\alpha_c \;=\; \frac{5}{3}\,T_C^2\,. \tag{5.12}$$

A rough estimation of $T_C \approx 700\,\text{K}$ at the reversal of the ordering temperature in YFe_2 can be obtained from the inspection of figure 5.18a (dashed line), leading to $\alpha_c \approx (900\,\text{K})^2$. Neglecting the weaker volume dependence of intraatomic correlations I/I_b [Woh81], the necessary increase of α must be attributed to a fourfold increase of T_F.

Taking into account the above assumption $T_F \propto W$, this enormous increase of T_F and α is not predicted in the framework of equation 5.9.

Hence, the Wohlfahrt theory can model the volume dependence of T_C in YFe_2 only at low pressures. Considering the underlying simplifications, a real quantitative description can not be expected. This holds especially for the electron density of states $D(E)$, which is by far more complex than assumed in the Wohlfahrt model. This is demonstrated in a band structure calculations of YFe_2 [MS85, ADM86], which also reveals an induced moment of 0.45 μ_B at the Y site, in accordance with NMR studies [DRM86].

5.4.2 Intersublattice Coupling Under Pressure

In contrast to YFe_2, the behaviour of $GdFe_2$ is governed by the interplay of two separate magnetic sublattices (3d band magnetism and localized 4f moments). In $GdFe_2$ at ambient pressure, the Fe sublattice contributes dominantly to the ordering temperature of 790 K, reflecting a large coupling parameter J_{FeFe}. The higher T_C in comparison to YFe_2 (535 K) is due to the exchange J_{FeGd} between 3d and 4f moments. The coupling parameter J_{GdGd} is smaller and can be estimated from the ordering temperature $T_{Gd} = 140\,\mathrm{K}$ of the Gd sublattice [SW99] (see also the discussion on pages 54-56).

Identifying the behaviour of YFe_2 as the pressure dependence of pure iron magnetism in RFe_2 compounds, one must conclude from the results presented in figure 5.18 that in $GdFe_2$ the Gd sublattice takes over the leading role in the Fe moment formation above 50 GPa.

Since the Gd 4f moment can be regarded as pressure-independent, this statement has implications on the two coupling constants J_{GdGd} and J_{FeGd} above 50 GPa: J_{GdGd} must be large enough for a magnetically ordered Gd sublattice at room temperature and the intersublattice coupling J_{FeGd} must be strong enough to induce a magnetic moment at the Fe sites. The observed average hyperfine field of about 10 T in $GdFe_2$ at 105 GPa is too large to be simply transferred from the 6 neighbouring Gd atoms [BCK90].

For $GdFe_2$ under pressure, resistivity measurements revealed a strong increase of T_{Gd} to about 180 K at 7 GPa [Str00]. The corresponding volume coefficient $d\,T_{Gd}/d\,\ln V = -1040(300)\,\mathrm{K}$ can be used for an extrapolation to 50 GPa ($\sim 25\%$ volume reduction), indicating that T_{Gd} reaches room temperature at that pressure.[11]

As mentioned in section 5.1.2 the interaction between the Gd and Fe sublattices is mediated by a hybridization between Fe 3d and Gd 5d states, where the latter are spin polarized by the 4f moments. When pressure is applied, the 3d-5d overlap will

[11] Another example for a pressure-induced increase of 4f-4f spin coupling was given in a recent NFS study by the Paderborn group. Here, the magnetic ordering temperature in EuTe was found to increase from 10 K at ambient pressure (NaCl phase) to almost 100 K at 22 GPa (CsCl phase) [LPH99, RW99, LRW00].

strongly increase leading to an enhanced coupling constant J_{FeGd}. This qualitative volume dependence was experimentally verified by Liu et al. for a variety of Er-Fe compounds with different molar volumes [LBC94]. This study was also accompanied by theoretical calculations of a hypothetical $GdFe_2$ with the lattice parameters of $ErFe_2$, corresponding to a reduction of the $GdFe_2$ lattice parameter by 1.5%. The coupling parameter J_{FeGd} was found to be almost 10% larger than for the uncompressed lattice. Hence, also J_{FeGd} can be considered to increase strongly in the investigated pressure range.

Summarizing, the observations for pure iron magnetism in YFe_2 and the pressure-induced increase of the coupling parameters J_{GdGd} and J_{FeGd} support the conclusion that the magnetic strength of the Gd sublattice surpasses that of the Fe sublattice above 50 GPa and becomes the driving force for the Fe moment formation. A more quantitative discussion requires the determination of ordering temperatures in $GdFe_2$ at high pressures, a demanding task for future NFS experiments. It should be further remembered that we are concerned, above 50 GPa, with $GdFe_2$ in the C14 structure.

Chapter 6

Lattice Dynamics in Iron Under Pressure

This chapter is concerned with the study of lattice dynamics in the bcc and hcp phase of iron at pressures up to 42 GPa. For this challenging task the new technique of Nuclear Inelastic Scattering of synchrotron radiation is employed, which has been introduced in chapter 3.3. In the first part (chapter 6.1), the general high-pressure behaviour of elemental iron is discussed considering also its geophysical relevance. Some principle features and equations of lattice dynamics which are necessary for later discussion are summarized in the second part. The rest of the chapter is devoted to the experimental results and their discussion.

6.1 Iron Under Pressure

The inner core of the Earth consists almost entirely of iron or an iron-rich alloy. This geophysical aspect is one of the many motivations to study the phase diagram of iron with its various allotropes in a wide pressure and temperature range (see figure 6.1). This holds especially for the hcp high-pressure phase of iron (ε-Fe), which is considered to be the most relevant phase for the inner core [YAC95] with pressures of 300-400 GPa and temperatures between 4000 K and 8000 K. At ambient pressure and temperature, iron is ferromagnetic and crystallizes in the bcc structure (α-Fe). The phase transformation from α-Fe to ε-Fe around 13 GPa was first reported by Bancroft et al. [BPM56]. As evidenced later, ε-Fe is nonmagnetic down to 30 mK [CTW82]. Depending on the employed pressure-transmitting medium, the α-ε transformation exhibits a broad coexistence range of both phases [BB90, TPJ91]. The transition interval (the pressure range between onset and completion of the transition) increases with the shear strength of the pressure medium from less than 0.2 GPa in helium to 15 GPa in Al_2O_3.

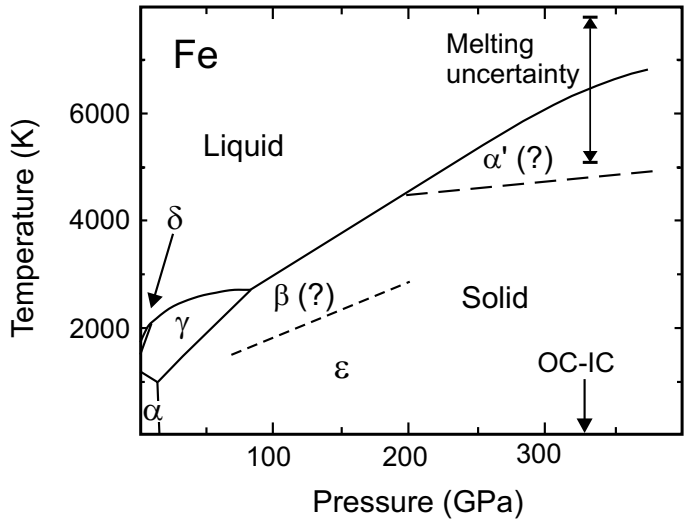

Figure 6.1: High-pressure phase diagram of iron, modified from [SMW96], including established phases α (magnetic bcc), γ (fcc), δ (nonmagnetic bcc), and ε (hcp) as well as two new phases β (proposed dhcp) and α' (proposed bcc), not yet established. For a review on recent experimental work and the discussion about the new phases see [And97]. The arrow ("OC-IC") at ∼330 GPa indicates the pressure at the inner-core/outer-core boundary.

Beside an enormous amount of experimental work related directly to the α-ε phase transformation, e.g. with x-ray diffraction [MBT67], shock-waves [BH74] and x-ray absorption [WI98], there is also recent theoretical work on this martensitic phase transition [MJ96, BW97, EEB98].

While a considerable amount of crystallographic data on the pressure/temperature phase diagram of Fe is available, there is, due to the difficult access, less experimental information on the lattice dynamics of iron under pressure, especially in the hcp phase.

6.2 Lattice Dynamics

In general, the lattice dynamics of solids are described by phonons, which are characterized by their dispersion relations $\omega_j(\vec{k})$ for different branches j and by their density of states (DOS) $g(E)$. The dispersion relations are usually measured with single-crystalline samples using inelastic neutron scattering (see e.g. [AM76]). Corresponding spectra for α-Fe at ambient conditions and for γ-Fe at ambient pressure and 1428 K can be found in [MSN67] and [ZS87], respectively. The phonon DOS $g(E)$ can be calculated from nearest-neighbour force constants [GR66], which are obtained by fitting the experimental results with a Born-von-Karman model [MSN67] (see figure 6.2).

However, experimental work with inelastic neutron scattering under pressure is diffi-

cult due to the requirement of large sample volumes (> 10 mm^3) and the limited flux of existing neutron sources [KBS95]. Exploratory measurements at pressures up to 7 GPa are reported for Fe_3Pt using a sample volume of 25 mm^3 [KBS95]. A set of transverse acoustic phonon frequencies has been measured for *Ge* up to 9.7 GPa [KBB97]. Information on the phonon dispersion is also accessible from the rapidly developing field of inelastic x-ray scattering with synchrotron radiation. Here, first high-pressure studies are performed for *CdTe* at 7.5 GPa [KMM97]. Optical vibrational modes at the zone-center (Γ point) can be investigated with Raman spectroscopy. Corresponding pressure experiments are reported by Olijnyk et al. for Zr metal up to 16 GPa [OJ97].

In contrast to inelastic scattering with neutrons and x-rays, Nuclear Inelastic Scattering (NIS) gives direct access to the phonon DOS without the necessity of measuring the full dispersion relations. Since NIS requires only polycrystalline samples, the experi-

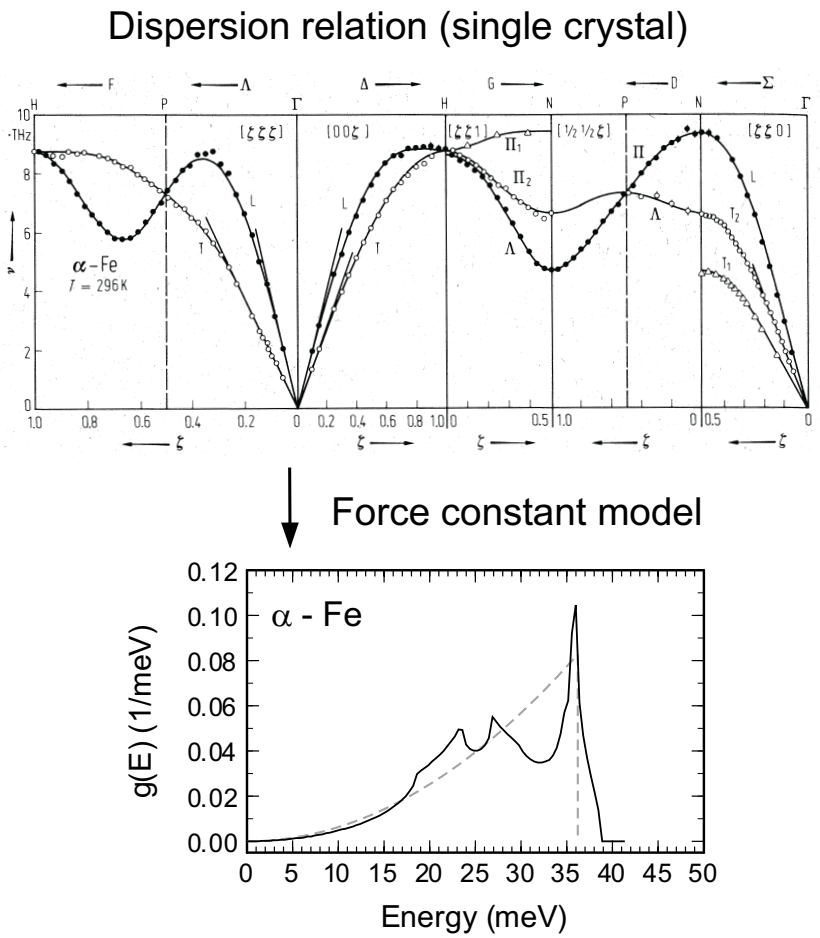

Figure 6.2: (top) Dispersion relation for α-Fe at ambient conditions from inelastic neutron scattering [MSN67]. (bottom) The solid line represents the derived phonon DOS. The dashed line shows the Debye approximation, calculated from equation 6.5 with $\Theta_D = E_D/k_B = 420$ K.

ments are not hampered by pressure-induced structural phase transformations, which limit neutron or x-ray scattering studies, requiring single crystals.

The principles and terminology of particular aspects of lattice dynamics are discussed below:

6.2.1 Debye Model

According to [AM76] the normalized phonon DOS $g(E)$ can be expressed in the general form as

$$g(E) = \frac{V}{(2\pi)^3} \sum_j \int \delta(E - \hbar\omega_j(\vec{k}))\, d\vec{k} \quad , \tag{6.1}$$

where V is the volume of the unit cell and the integral is taken within the first Brillouin zone. Similar to the case of the electronic DOS, this equation can be written in an alternative form [AM76]:

$$g(E) = \frac{V}{(2\pi)^3 \hbar} \frac{1}{3} \sum_j \int \frac{dS}{|\nabla \omega_j(\vec{k})|} \quad , \tag{6.2}$$

where the integration is now taken over that surface in the first Brillouin zone on which $\hbar\omega_j(\vec{k}) \equiv E$. Due to the periodicity of $\omega_j(\vec{k})$, there will be a series of discontinuities in $g(E)$, reflecting the fact that the group velocity appearing in the denominator of equation 6.2 must vanish at some frequencies. As in the electronic case, the discontinuities are related to van Hove singularities.

In the Debye approximation $g_D(E)$ of the phonon DOS, the same linear dispersion relation $\omega = \bar{v}\, k$ is assumed for the three acoustic branches of $\omega_j(\vec{k})$ with an average sound velocity $\bar{v}$. In addition, the integral in equation 6.1 is replaced by an integral over a sphere of radius k_D, chosen to fulfil the normalization condition for $g_D(E)$:

$$g_D(E) = \frac{V}{(2\pi)^3} \int\limits_{k<k_D} \delta(E - \hbar\bar{v}k)\, d\vec{k} \tag{6.3}$$

$$= \frac{V}{2\pi^2} \int\limits_0^{k_D} k^2\, \delta(E - \hbar\bar{v}k)\, dk \tag{6.4}$$

$$= \begin{cases} \alpha E^2, & E \le E_D \\ 0\ , & E > E_D \end{cases} \tag{6.5}$$

$$\text{with} \quad E_D = \hbar\bar{v}k_D \quad \text{and} \quad \alpha = \frac{V}{2\pi^2\hbar^3\bar{v}^3}. \tag{6.6}$$

For the above transformations the relations $\int d\vec{k} = 4\pi \int k^2\, dk$, $E = \hbar\bar{\nu}k$ and $dk = dE\,/\hbar\bar{\nu}$ have been used. The cut-off energy E_D is determined by the normalization $\int g_D(E)\, dE = 1$:

$$E_D = (\alpha/3)^{-1/3} = \left(\frac{V}{6\,\pi^2 \hbar^3\, \bar{\nu}^3} \right)^{-1/3} . \tag{6.7}$$

Consequently, the complete phonon DOS $g_D(E)$ is determined by a single parameter, namely E_D. It is often convenient to define a Debye temperature $\Theta_D = E_D/k_B$ as a measure of the temperature, above which all phonon modes begin to be excited and below which modes begin to be "frozen out". Both, E_D and Θ_D, can be also regarded as measures of the rigidity of the crystal. For iron at ambient conditions a value of Θ_D = 420 K can be derived from high-temperature specific heat data [AM76]. The Debye approximation for the phonon DOS of α-Fe is shown in figure 6.2 together with the experimental data derived from neutron scattering. Under pressure, the phonon energies and hence the Debye temperature Θ_D should increase, since a normal solid becomes more rigid under compression. The pressure dependence of Θ_D is usually given in terms of the Debye-Grüneisen parameter γ_D, which is discussed in the next subsection.

6.2.2 Grüneisen Parameter

The theory of harmonic lattice vibrations fails in the description of important physical phenomena such as thermal expansion and the volume dependence of elastic coefficients. It is evident that these effects of anharmonicity in the interaction energy should have a decisive impact on the equations of state of condensed matter under strong compression.

Usually, the harmonic theory is expanded for a *quasi-harmonic* lattice by taking into account anharmonicities only through mode Grüneisen parameters

$$\gamma_i = -\,d\,\ln\omega_i / d\,\ln V \tag{6.8}$$

for the volume dependence of the lattice mode frequencies ω_i. In most cases, the Mie-Grüneisen approximation is used which implies that all mode Grüneisen parameters γ_i can be replaced by one common average value γ, which depends only on the volume (see [AM76, Hol96]). In the Debye model, where all mode frequencies scale linearly with the cut-off energy, one obtains

$$\gamma_D = -\,d\,\ln\Theta_D / d\,\ln V\ . \tag{6.9}$$

Within the Debye approximation, the parameter γ_D becomes identical to the *thermodynamic* Grüneisen parameter

$$\gamma_{th} = \alpha_V\, K_T\, V\,/\,c_V\ , \tag{6.10}$$

with the volume expansion coefficient α_V, the isothermal bulk modulus K_T, the volume V and the isochoric heat capacity c_V. Thus γ_{th} is composed of individual measurable physical quantities, each of them varying significantly with temperature. However, the ratio of these properties is almost independent of temperature. Usually one observes $1 < \gamma_{th} < 2$, and generally γ_{th} decreases as the volume decreases.

Important geophysical significance of γ_D in the case of iron results from the Lindemann law in the form

$$\frac{d \ln T_m}{d \ln \rho} = 2 \left(\gamma_D - \frac{1}{3} \right) , \tag{6.11}$$

which relates the melting temperature T_m to the density ρ. [1] Equation 6.11 can be used to extrapolate existing melting data up to 200 GPa [Boe93] to the pressure of the outer-inner core boundary at 330 GPa. Furthermore, γ is needed for the evaluation of shock-wave data up to 240 GPa [BM86] and their extrapolation to 330 GPa.

Estimates on the temperature profile of the Earth's core rely on the assumption that the boundary between the solid inner core and the liquid outer core is at the melting temperature of the core material. Given that the core is composed of an iron-nickel alloy with small amounts (< 10%) of lighter elements, and accounting for the fact that impurities tend to lower melting temperatures, the T_m value for pure iron at or near 330 GPa would place an upper limit to the boundary temperature [Buk99].

A further important aspect of γ is connected with the heat of crystallization at the solid-liquid core boundary which depends on γ [AD97]. This continuously generated thermal energy is the driving force for the Earth's magnetic field, which is produced by convection in the electrically conducting outer core [Ols97]. Furthermore, the core provides sufficient heat to influence even mantle convection and hence tectonic motions, earthquakes and volcanism [Buk99].

6.2.3 Elastic Coefficients and Aggregate Velocities

Another significant aspect of lattice dynamics is the propagation of sound waves in matter. In the case of iron, the geophysical relevance of sound waves under pressure is obvious since seismic waves are the most important probes for the internal structure of the Earth (see figure 6.3). Of actual interest are the sound velocities in the ε-phase of iron, since seismic wave experiments indicate an anisotropy of the sound velocities in the Earth´s inner core [Cre92] and a differential rotation of the inner core with respect to the adjacent liquid outer core [SR96].

[1] The representation 6.11 of the Lindemann law is developed for example in [And95] assuming a Debye-like solid and a Grüneisen parameter γ_D following equation 6.9. In its original form (see e.g. [Gsc64]), the Lindemann law includes a special "melting Debye temperature" Θ_D^m and thus a special Grüneisen parameter γ_m. However, as shown in [Gsc64], the approximation $\gamma_m \approx \gamma_D$ is valid for a large number of elements.

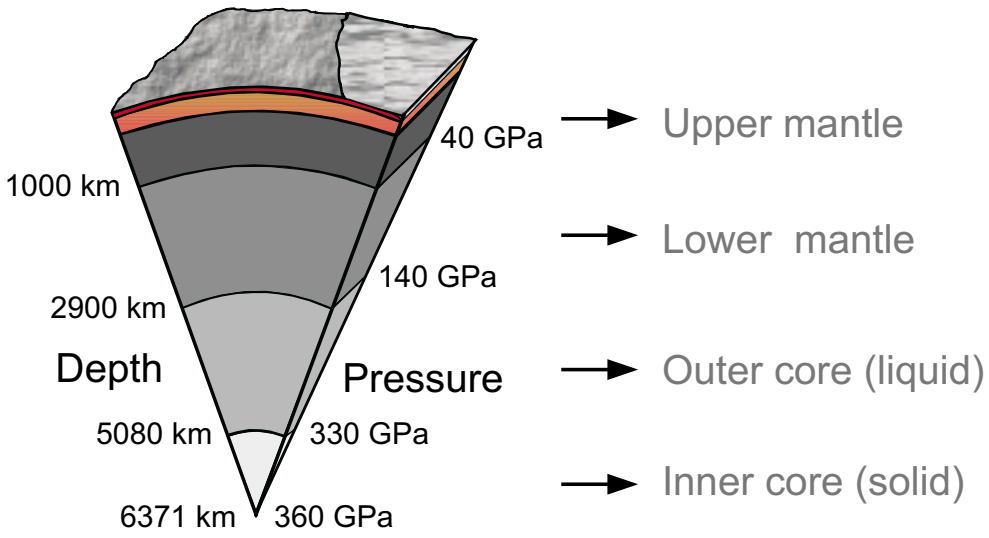

Figure 6.3: Schematic structure of the Earth's interior with different layers as derived from seismological observations (adapted from [Hol98b]). Whereas the mantle is made up of minerals and rock, the liquid outer core and solid inner core consist mainly of iron. An estimation for the boundary temperature between outer and inner core is provided by the melting temperature of iron.

Sound waves are intimately related to the elastic properties of solid materials. In order to compare studies of sound velocities and elastic coefficients, this relationship is briefly discussed in the next paragraphs following [SAS73].

Elastic coefficients are defined in terms of the response of a crystal to an applied stress. In the most general case, a 6x6 matrix C with 36 elastic stiffness coefficients c_{ij} is used. Its inverse is called elastic compliance S. In the absence of body torques both matrices are symmetric and the number of independent elastic coefficients reduces to 21 in the lowest-symmetry case of a triclinic crystal. For higher crystal symmetry, this number is further reduced: for a hexagonal system to five and for a cubic system down to three.

The bulk modulus K and the shear modulus G of polycrystalline solids can be calculated from C and S with various averaging schemes. The Voigt approximation is based on the assumption that the *stress* is uniform throughout the sample and gives:

$$K_V = \frac{1}{9}(c_{11}+c_{22}+c_{33}) + \frac{2}{9}(c_{23}+c_{13}+c_{12}),$$

$$G_V = \frac{1}{15}(c_{11}+c_{22}+c_{33}) - \frac{1}{15}(c_{23}+c_{13}+c_{12}) + \frac{1}{5}(c_{44}+c_{55}+c_{66}),$$

whereas the Reuss scheme assumes an uniform *strain* providing:

$$\frac{1}{K_R} = (s_{11}+s_{22}+s_{33})+2\,(s_{23}+s_{13}+s_{12})\,,$$

$$\frac{1}{G_R} = 4\,(s_{11}+s_{22}+s_{33})-4\,(s_{23}+s_{13}+s_{12})+3\,(s_{44}+s_{55}+s_{66})\,.$$

The Voigt and Reuss averaging schemes determine upper and lower limits for the polycrystalline moduli. Their arithmetic mean is usually used as the most probable values for K and G.

For cubic systems, symmetry aspects lead to $c_{11}=c_{22}=c_{33}$, $c_{12}=c_{23}=c_{31}$, $c_{44}=c_{55}=c_{66}$. For hexagonal systems one obtains $c_{11}=c_{22}$, $c_{13}=c_{23}$, $c_{44}=c_{55}$, $c_{66}=(c_{11}-c_{12})/2$.

The so-called aggregate velocities can be calculated from K, G and the density ρ for

$$\text{longitudinal or compressional waves:}\quad v_p^2 = \left(K+\frac{4}{3}G\right)/\rho\ , \tag{6.12}$$

$$\text{and for transversal or shear waves:}\quad v_s^2 = G/\rho\ . \tag{6.13}$$

The commonly used notation with subscripts p for "primary" and s for "secondary" originates from seismology because the longitudinal waves are faster and detected earlier than the shear waves.

The velocities v_p and v_s are simply related to the mean sound velocity $\overline{v}$ in the Debye model (equation 6.5), because the sum over three acoustic branches in equation 6.1 with a mean sound velocity $\overline{v}$ can be replaced by the sum over one longitudinal branch with sound velocity v_p and two transverse branches with sound velocity v_s:

$$\frac{3}{\overline{v}^3} = \frac{1}{v_p^3}+\frac{2}{v_s^3}\,. \tag{6.14}$$

6.3 Nuclear Inelastic Scattering in Iron

Now we turn to the experimental results which were obtained with Nuclear Inelastic Scattering (NIS). A tiny ^{57}Fe sample of 0.5 μg was pressurized in a diamond-anvil cell as explained in chapter 4. In the first part of this section we present the measured NIS spectra and the extraction of the phonon DOS. The second part covers the derivation of related properties and their discussion.

6.3.1 NIS Spectra

The NIS spectra were measured for α-Fe (0 GPa, 6 GPa and 11 GPa) and ε-Fe (20 GPa, 32 GPa and 42 GPa) at room temperature (294 K). At 20 GPa and higher, the additionally measured NFS spectra revealed the non-magnetic phase of iron, confirming a complete structural transition to ε-Fe. The energy spectra are shown in figure 6.4 after normalization with Lipkin's sum rule (equation 3.28). They consist of a central peak originating from elastic scattering and sidebands resulting from inelastic scattering with concomitant annihilation (left side) and creation (right side) of phonons. According to equation 3.31 the relative weight of the two sidebands is given by $\exp(|E|/k_B T)$. Under pressure, the main spectral features are shifted to higher energies, reflecting an increase of lattice vibration frequencies; consequently, the asymmetry gets more pronounced at higher pressures.

The spectrum at ambient pressure is shown with the corresponding spectrum calculated with the phonon DOS from neutron scattering [MSN67] using equations 3.25, 3.26 and 3.27. For comparison it is convoluted with the present spectrometer function. The two data sets are shown in absolute scale without any adjustable parameter, demonstrating good agreement between the two methods.

As outlined in section 3.3.2, NIS spectra of iron are dominated by single-phonon scattering. The small contribution of multi-phonon scattering is clearly visible at the high-energy side of the spectra (indicated by a little arrow in the spectrum at ambient pressure). It amounts less than 12% of the total intensity of the sidebands.

The spectra shown in figure 6.4 are added from 20-30 single energy scans of the high-resolution monochromator (HRM) in a range of about $\pm$110 meV around the nuclear resonance. Before summing up, the energy scale of every single scan is calibrated with the zero position from the resolution function, measured in forward direction.

All spectra at high pressure were measured with a nested HRM composed of two channelcut Si(4 2 2) and Si(12 2 2) crystals. The spectrum at ambient pressure was recorded in an earlier beamtime with a similar monochromator but using Si(4 2 2)/Si(9 7 5) reflections. The corresponding energy resolutions are obtained by fitting the measured resolution functions with a Gaussian shape (see table 6.1). For ambient pressure and above 20 GPa (ε-Fe) the observed resolution matches the expected values of $\sim$4.4 meV

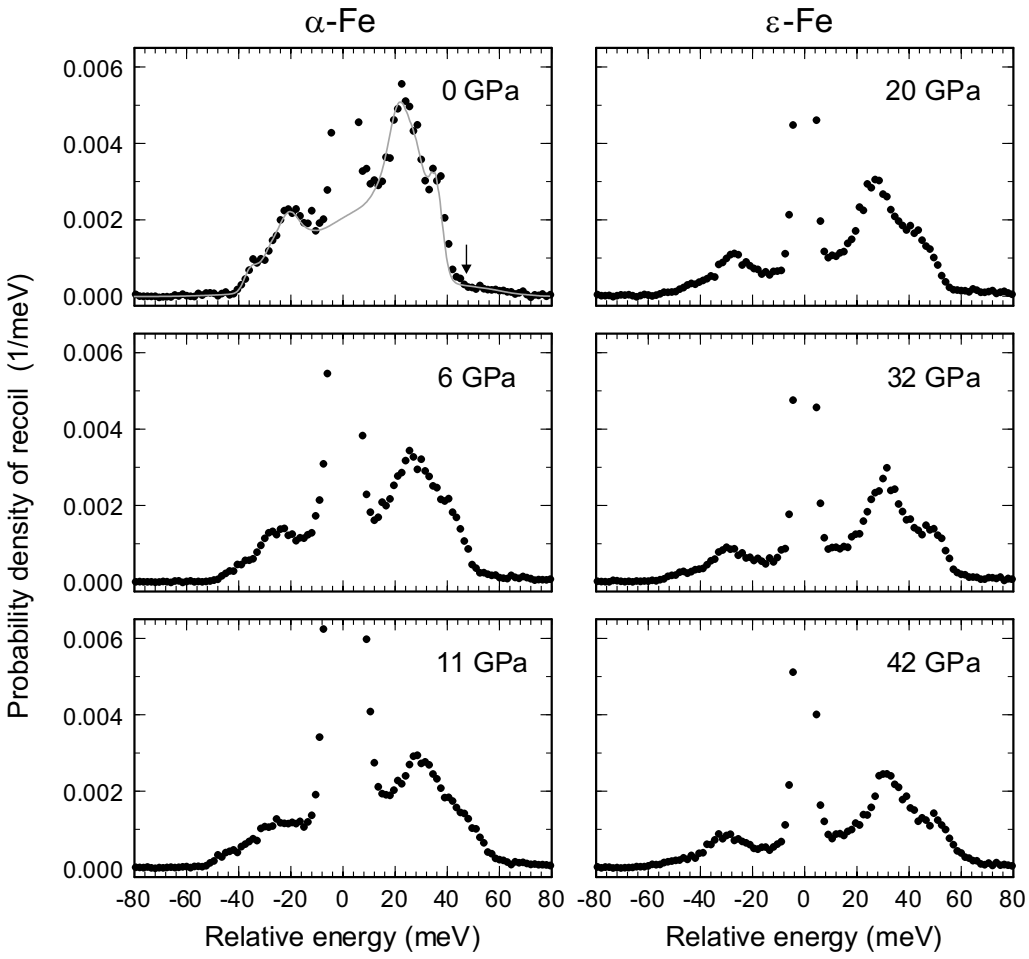

Figure 6.4: Energy dependence of Nuclear Inelastic Scattering in α-Fe (left) and ε-Fe (right) at various pressures. The spectra are normalized according to equation 3.28. The intensity of the inelastic sidebands is proportional to (1- f_{LM}); it decreases with increasing pressure by about 50%, reflecting the change in the recoil-free fraction, f_{LM}, from 0.80 to about 0.90 (see table 6.2). The solid line at 0 GPa is calculated from neutron data [MSN67], convoluted with the spectrometer function. The little arrow in the spectrum at ambient pressure indicates the small contribution of multi-phonon scattering.

and ∼6.4 meV, respectively. However, the spectra at 6 GPa and 11 GPa show higher values of 7.9 meV and 9.8 meV. The reason for this resolution broadening is not completely clear. A defective HRM adjustment can be rejected, because all spectra are measured with the same set-up in the sequence 20 GPa, 32 GPa, 6 GPa, 11 GPa, 42 GPa. One possible reason for the energy broadening is the interplay between focusing optics, pre-monochromator and the HRM, since the spot size of the concentrated synchrotron radiation (100 μm x 100 μm) matches the sample size for 20 - 42 GPa, but is considerable smaller than the sample at 6 - 11 GPa (diameter 250 μm).

Pressure (GPa)	FWHM (meV)
0	4.6
6	7.9
11	9.8
20	6.5
32	6.5
42	6.4

Table 6.1: Energy resolution for the NIS experiments obtained as the FWHM (full width at half maximum) of a Gaussian which is adjusted to the forward scattered energy spectrum.

6.3.2 Extracted Phonon DOS

The procedure to extract the phonon DOS $g(E)$ from the NIS spectra was introduced in detail in section 3.3.2. For this purpose the spectra were normalized and multi-phonon contributions as well as the central elastic peak were subtracted. The remaining spectrum represents the single phonon contribution, from which $g(E)$ was extracted (equation 3.26)[2].

In order to verify the normalization of the resulting phonon DOS, the areas were calculated. They showed a slight variation around unity with a mean deviation of 3.1%. In a previous NIS study of the temperature-dependent behaviour of elemental iron [CRB96], a similar deviation of 2.3% was found and attributed to statistical errors. The uncertainty of the normalization was corrected by renormalizing each $g(E)$.

The resulting phonon DOS for α-Fe and ε-Fe are shown in figure 6.5. The DOS at ambient pressure is again well described by the solid line representing the data from neutron scattering [MSN67]. A strong increase of all spectral features with pressure is obvious. The resolved high-energy maximum of the DOS, originating mainly from longitudinal acoustic (α-Fe) and longitudinal acoustic and optical (ε-Fe) phonon branches, is shifted from 35 meV in α-Fe at ambient pressure to 51 meV in ε-Fe at 42 GPa. The observed changes in the phonon spectra reflect mostly the reduced volume of the unit cell; modifications resulting from the structural transition are small for mono-atomic lattices (see e.g. [AAM93]) and are not resolvable with the present energy resolution. The present resolution, however, is sufficient to derive a set of related parameters from the integral properties of the phonon DOS.

[2] In general, it is possible to extract the phonon DOS individually from both sides of the NIS spectra (see figure 3.12). In practice, the (left) annihilation part is usually discarded due to its lower statistical accuracy.

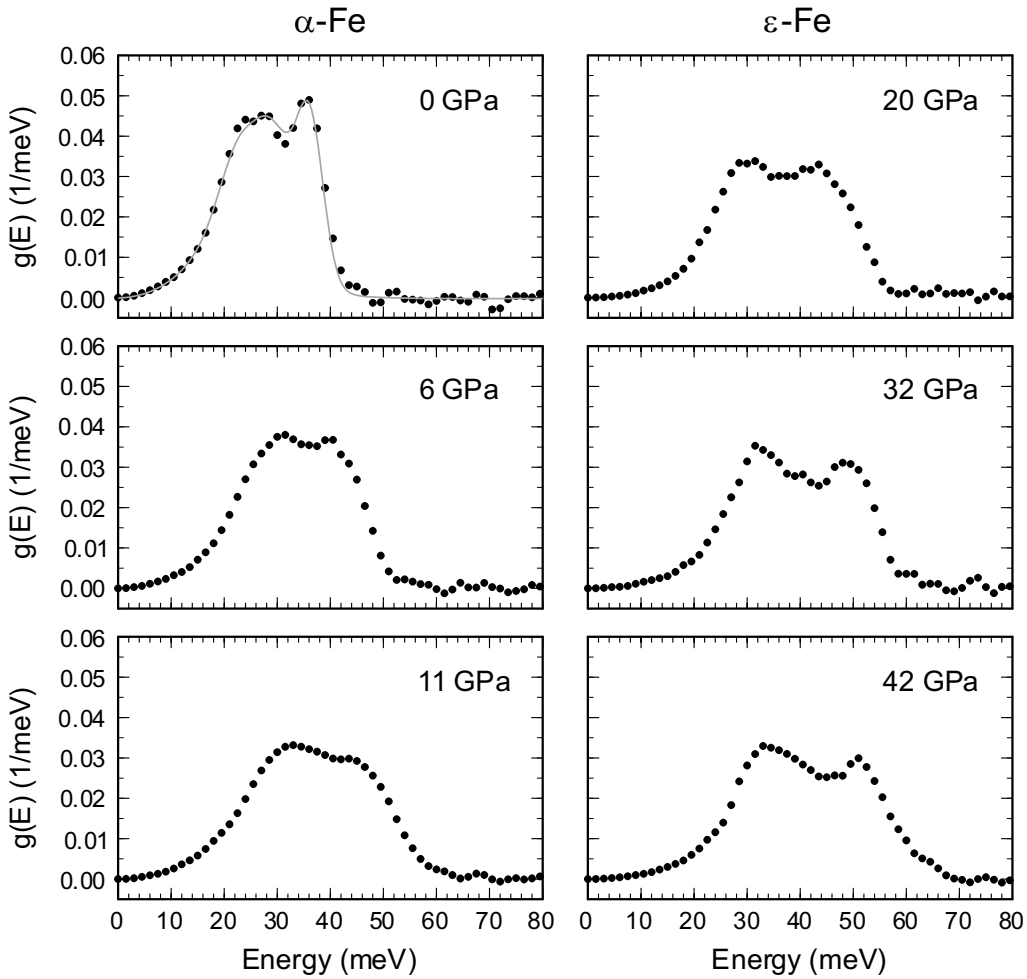

Figure 6.5: Phonon DOS $g(E)$ for α-Fe and ε-Fe derived from the NIS spectra in figure 6.4. The solid line represents the DOS from neutron scattering [MSN67], convoluted with the spectrometer function.

6.3.3 Derived Properties

The phonon DOS $g(E)$ is of fundamental importance for the study of lattice dynamics. Its knowledge provides information on the lattice rigidity as well as thermodynamic properties according to the following equations and figures. The results are summarized in table 6.2. In order to examine the reliability of the derived parameters, they are compared with those from neutron data of α-Fe at ambient pressure (first line in table 6.2).

Pressure (GPa)	V/V_0	f_{LM} (area)	f_{LM} (DOS)	$\langle \Delta x^2 \rangle$ (10^{-3} Å^2)	F_{vib} (meV/at.)	U_{vib} (meV/at.)	c_{V} (k_B/at.)	S_{vib} (k_B/at.)	$\overline{D}$ (N/m)	$\overline{\mathrm{v}}$ (km/s)
neutron	1	-	0.801(4)	4.15	5.9	83.6	2.71	3.07	173	3.54
0	1	0.791(6)	0.802(4)	4.13(8)	7.4(10)	83.4(15)	2.70(3)	3.00(3)	185(12)	3.57(10)
6	0.967	0.848(12)	0.852(8)	3.00(16)	23.1(20)	87.0(30)	2.58(6)	2.52(6)	279(25)	4.10(25)
11	0.945	0.855(12)	0.870(8)	2.61(16)	29.6(20)	89.4(30)	2.52(6)	2.36(6)	322(25)	4.16(25)
20	0.862	0.883(6)	0.882(4)	2.35(8)	31.5(10)	90.0(15)	2.51(4)	2.31(4)	320(15)	4.82(15)
32	0.828	0.893(6)	0.893(4)	2.12(8)	38.1(10)	91.8(15)	2.44(4)	2.12(4)	365(15)	5.00(15)
42	0.805	0.898(6)	0.897(4)	2.03(8)	40.8(10)	93.0(15)	2.42(4)	2.06(4)	388(15)	5.14(15)

Table 6.2: Properties of iron at $T = 294\,K$: Lamb-Mössbauer factor f_{LM} derived from the area of the inelastic spectrum and from the density of phonon states $g(E)$, mean-square displacement $\langle \Delta x^2 \rangle$; lattice contribution to Helmholtz free energy F_{vib}, internal energy U_{vib}, isochoric specific heat c_{V} and entropy S_{vib}; mean force constant $\overline{D}$ and mean sound velocity $\overline{\mathrm{v}}$, derived from the low-energy part of $g(E)$. For details see text. V/V_0 : relative volume of unit cell obtained from the compressibility data for α-Fe [MBT67] and ε-Fe [MWC90] with $V_0 = 7.093$ cm^3/mol. The uncertainties given in brackets represent statistical standard deviations. The error in the recoil fraction 1 - f_{LM} was estimated by the normalization uncertainty of $g(E)$.

Lattice Rigidity

First, the Lamb-Mössbauer factor f_{LM}, describing the elastic (recoil-free) fraction of nuclear scattering, can be calculated from $g(E)$ using an equation from Singwi and Sjölander [SS60]:

$$f_{LM} = \exp\left(-E_R \int_0^\infty \frac{g(E)}{E} \frac{1+e^{-E/k_BT}}{1-e^{-E/k_BT}}\, dE\right). \tag{6.15}$$

As mentioned in chapter 3.3.2, f_{LM} can be also determined from the area under the normalized NIS spectrum ($= 1 - f_{LM}$). The values for both procedures are listed in table 6.2 and show rather good agreement. Due to the possibility to renormalize the obtained $g(E)$, the f_{LM}(DOS) values from equation 6.15 are less influenced by experimental error [CRB96]. They are used to calculate the mean-square displacement

$$\langle \Delta x^2 \rangle = -\frac{\ln(f_{LM})}{k^2}, \tag{6.16}$$

using the wave vector k = 7.31 Å^{-1} of the 14.413 keV quanta.

The Lamb-Mössbauer factor f_{LM}(DOS) from $g(E)$ and the mean-square displacement are plotted in figure 6.6. In α-Fe f_{LM} shows a steep increase from 0.802(4) at ambient pressure to 0.870(8) at 11 GPa. After the phase transition the slope is strongly reduced and a value of 0.897(4) is reached at 42 GPa (V/V_0 = 0.805). Since the recoil-free fraction f_{LM} can not exceed the value of 1, the pressure effect on the lattice dynamics from 0 GPa to 42 GPa is more pronounced in the mean-square displacement $\langle \Delta x^2 \rangle$, which is reduced by 50% from 4.13(8)$\times 10^{-3}$ Å^2 to 2.03(8)$\times 10^{-3}$ Å^2.

The hardening of the crystal lattice is also reflected by the behaviour of the mean force constant $\overline{D}$. Following [CS99, KCR98], $\overline{D}(\vec{s})$ can be obtained along the direction $\vec{s} = \vec{k}/k$ of the incident x-ray beam using the mass m of the vibrating atoms:

$$\overline{D}(\vec{s}) = \frac{m}{\hbar^2} \int_0^\infty g(E)\, E^2\, dE. \tag{6.17}$$

In the investigated pressure range, $\overline{D}$ shows a strong increase from 185(12) N/m to 388(15) N/m.

The mean sound velocity $\overline{v}$ can be determined from the low-energy part of $g(E)$, where one can assume a linear relation between the phonon frequency ω and the lattice k-vector. With an average slope $\overline{v} = \omega/k$ for the three acoustic branches, a quadratic energy dependency is obtained (see equation 6.5 and [KCR98]).

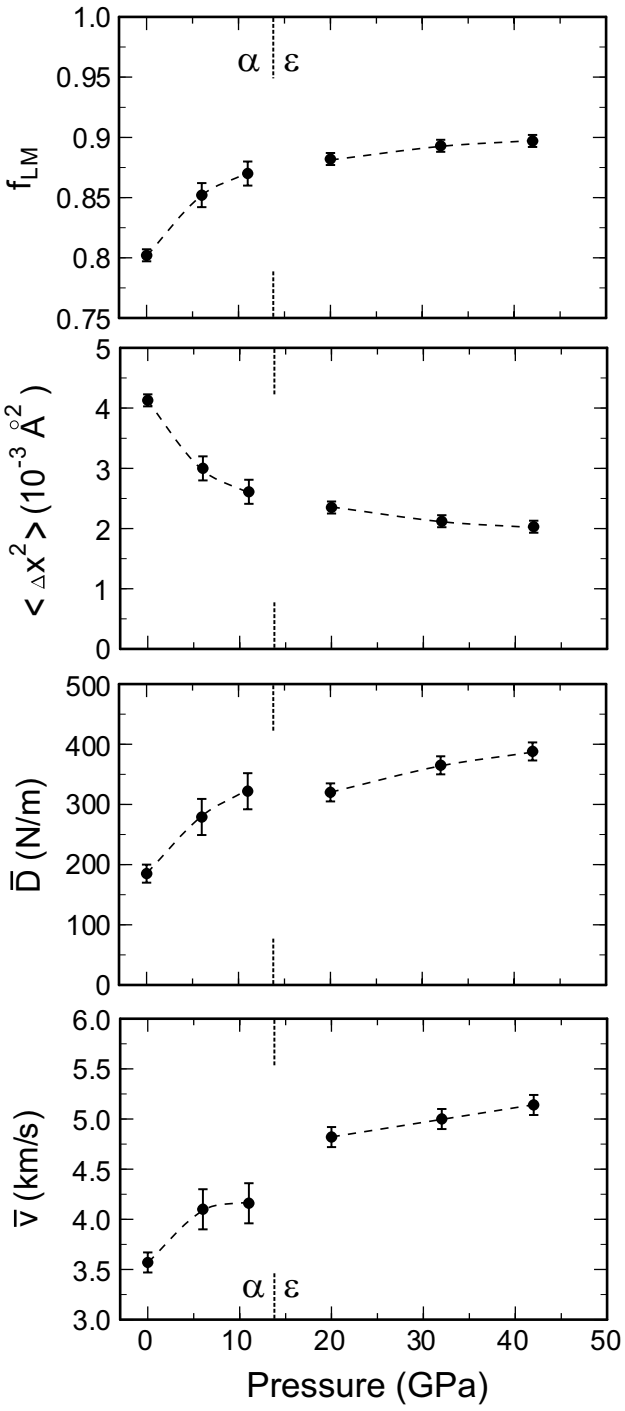

Figure 6.6: Lamb-Mössbauer factor f_{LM} from $g(E)$, mean-square displacement $\langle \Delta x^2 \rangle$, mean force constant $\overline{D}$ and mean sound velocity $\bar{v}$. The dashed lines are guides to the eye. The vertical lines indicate the borders of the α-ε transformation.

The low-energy parts up to 15 meV are shown in more detail in figure 6.7 together with a quadratic fit $g(E) = \alpha E^2$ to the experimental data. In order to increase the number of data points for the fit, the phonon DOS from both sides of the NIS spectra is used. According to equation 6.6, the mean sound velocity $\overline{v}$ was derived from α and the corresponding volume V for each pressure (see fig 6.6).

In contrast to f_{LM} the values of $\overline{v}$ indicate a discontinuity at the phase transition. When the transition pressure is approached, a jump by 16% from 4.16(25) km/s at 11 GPa to 4.82(15) km/s at 20 GPa is observed. Within the ε-phase the change is smaller and $\overline{v}$ increases only to 5.14(15) km/s at 42 GPa.

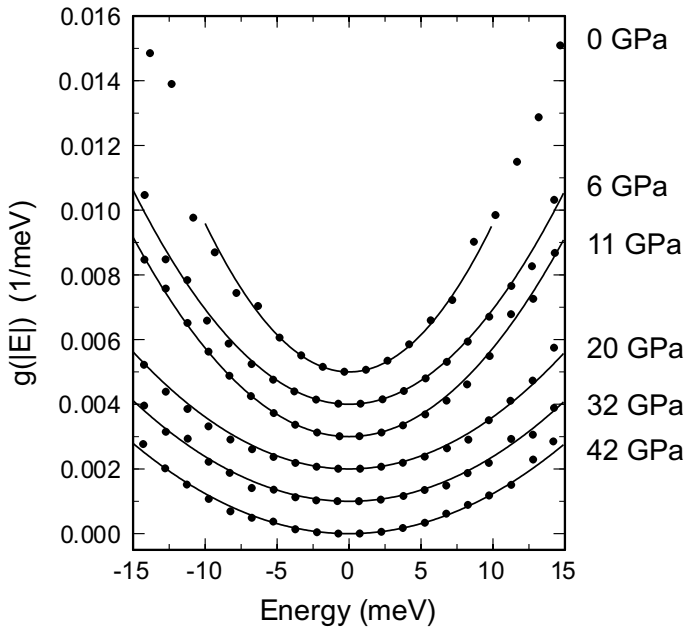

Figure 6.7: Plot of $g(|E|)$ up to 15 meV for each pressure together with a quadratic fit to the experimental data. For clarity the spectra are successively shifted by 0.008 meV^{-1}.

Thermodynamic Properties

The vibrational contribution to a variety of thermodynamic properties can be calculated from $g(E)$ in the quasi-harmonic approximation, beginning with the Helmholtz free energy F_{vib} and deriving the internal energy U_{vib}, the specific heat c_V and the entropy S_{vib} [JM85]:

$$F_{\text{vib}} = 3k_BT \int_0^\infty g(E) \ln\left[e^{E/2k_BT} - e^{-E/2k_BT}\right] dE \tag{6.18}$$

$$U_{\text{vib}} = F - T\left(\frac{\partial F}{\partial T}\right)_V = \frac{3}{2}\int_0^\infty g(E)\, E\, \frac{e^{E/k_BT}+1}{e^{E/k_BT}-1}\, dE \tag{6.19}$$

$$c_v = \left(\frac{\partial U}{\partial T}\right)_V = 3k_B \int_0^\infty g(E)\, \frac{(E/k_BT)^2\, e^{E/k_BT}}{(e^{E/k_BT}-1)^2}\, dE \tag{6.20}$$

$$S_{\text{vib}} = -\left(\frac{\partial F}{\partial T}\right)_V = 3k_B \int_0^\infty g(E) \left[\frac{(E/k_BT)}{2}\frac{e^{E/k_BT}+1}{e^{E/k_BT}-1}\right. \tag{6.21}$$

$$\left. - \ln\left(e^{E/2k_BT} - e^{-E/2k_BT}\right)\right] dE.$$

Using the Bose occupation factor $n_B(E,T) = 1/(\exp(E/k_BT)-1)$, the equation for U_{vib} simplifies to

$$U_{\text{vib}} = 3\int_0^\infty g(E)\, E\, \left(\frac{1}{2} + n_B(E,T)\right) dE. \tag{6.22}$$

This equation elucidates the definition of $g(E)\,dE$ as the number of phonon states within the energy interval $[E,E+dE]$, which has to be multiplied with the energy $E\,(n_B(E,T)+1/2)$ of the corresponding harmonic oscillators to obtain the internal energy U_{vib}.

The pressure dependence of the thermodynamic parameters at 294 K (figure 6.8) indicates a discontinuos behaviour at the α-ε phase transition reflecting the different thermodynamic properties of the two phases. Whereas the pressure-induced increase of F_{vib} and U_{vib} demonstrates the energy gain of the lattice vibrations, the decrease of c_{V} and S_{vib} can be interpreted in terms of a decreasing effective crystal temperature at high pressure. This effective crystal temperature can be defined as the ratio T/Θ_D of the real temperature T and the Debye temperature Θ_D. The latter is discussed in the next section.

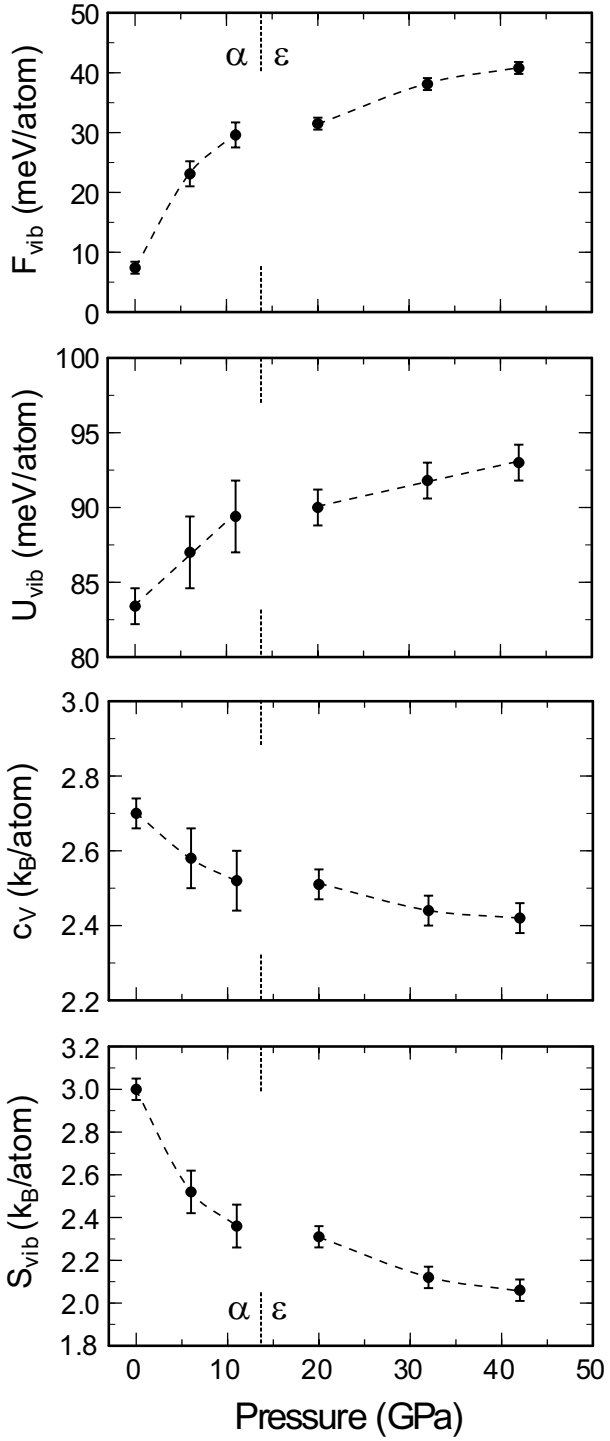

Figure 6.8: Thermodynamic properties of iron at $T = 294\,K$ derived from $g(E)$: lattice contribution to Helmholtz free energy F_{vib}, internal energy U_{vib}, isochoric specific heat c_{V} and entropy S_{vib}. The dashed lines are guides to the eye.

Debye Temperature Θ_D

One of the basic features of the Debye model is the representation of the phonon DOS $g_D(E)$ by a single parameter Θ_D (see page 92). This allows an easy discussion of the volume dependence of the phonon DOS with the widest impact on the related properties. Since the actual $g(E)$ for a real solid is generally not completely Debye-like, it can not be described by a single parameter. However, in the absence of experimental data on $g(E)$, the measured temperature dependence of thermodynamic properties is usually approximated assuming a Debye-like behaviour, e.g. for $c_V(T)$, and within this approximation a single parameter Θ_D is obtained. In principle, these Debye temperatures are related to the energy part of the phonon DOS, which determines the behaviour of the corresponding thermodynamic property. A well-known example is the Debye temperature derived from the specific heat $c_V(T)$ in different temperature regions: whereas the low-temperature part of $c_V(T)$ is governed by low-energy vibrations, the high-temperature part includes information about the complete phonon spectrum (see e.g. [Gsc64]). The two resulting Debye temperatures are usually called low-temperature limit and high-temperature limit of Θ_D.

In the case of a measured phonon DOS, a Debye temperature can be assigned directly to the function $g(E)$. Using certain properties of the Debye DOS $g_D(E)$, three different possibilities to determine Θ_D directly from the experimental $g(E)$ are obvious: the extraction of Θ_D from

1. the low-energy part of $g(E) = \alpha E^2$ from which also the mean sound velocity was derived. According to equation 6.7, Θ_D can be calculated by $k_B \Theta_D = (\alpha/3)^{-1/3}$. These values represent the low-temperature limit of Θ_D (see Θ_D(lt) in table 6.3);

2. the average phonon energy $\overline{E}_{ph}$, i.e. the first moment of the phonon DOS, which is given in the Debye model by $\Theta_D = (4/3)\overline{E}_{ph}/k_B$. The corresponding values represent the high-temperature limit of Θ_D (see Θ_D(ht) in table 6.3);

3. the cut-off energy in the phonon DOS, determined by longitudinal branches. Although this value can be easily estimated from $g(E)$ without further calculation, the exact determination is arbitrary and much more influenced by the energy resolution than the above mentioned procedures. Therefore, this possibility is discarded in the following.

Within the studied pressure range the Debye temperatures in table 6.3 and figure 6.9 show an increase by 45% and 55% for Θ_D(ht) and Θ_D(lt), respectively. The differences between the two values reflect deviations of the measured phonon DOS from the Debye model. In α-Fe the results for Θ_D(lt) are about 30 K higher than for Θ_D(ht) (except 11 GPa). This behaviour is well-known for normal solids, especially with respect to measurements of the specific heat c_V, which are often represented within the Debye model, but with the use of a temperature dependent Θ_D. [3]

[3] However, the phonon DOS itself does not change with temperature and the presentation with a

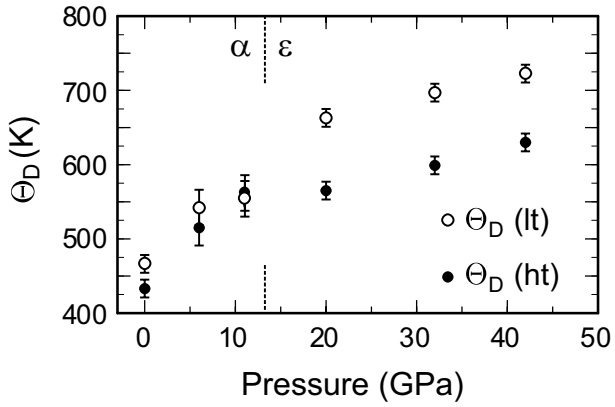

Figure 6.9: Pressure dependence of Debye temperatures, determined from the low-energy part of $g(E)$ (Θ_D(lt)) and the first moment of $g(E)$ (Θ_D(ht)).

In ε-Fe the difference between the two Θ_D values is about 100 K. Consequently, the deviations from the Debye model are much more pronounced in this high-pressure phase. Since the Debye model includes only acoustic vibrations with $\omega = \overline{v}k$, the deviations can be attributed to the existence of optical branches in the hcp phase.

An third set of Debye temperatures can be derived from the recoilless fraction f_{LM}(DOS) in table 6.2 using the formalism of conventional Mössbauer spectroscopy [Gib76]. These values ($\Theta_D(f_{LM})$ in table 6.3) lie in between the above mentioned limits.

Pressure (GPa)	V/V_0	$\overline{E}_{ph}$ (meV)	Θ_D(ht) (K)	Θ_D(lt) (K)	$\Theta_D(f_{LM})$ (K)
neutron	1	27.2	421	460	439
0	1	28.0(8)	433(12)	467(10)	440(5)
6	0.967	33.3(16)	515(24)	542(25)	523(12)
11	0.945	36.4(16)	563(24)	555(25)	563(12)
20	0.862	36.5(8)	565(12)	663(15)	597(10)
32	0.828	38.7(8)	599(12)	697(15)	632(10)
42	0.805	40.7(8)	630(12)	723(15)	646(10)

Table 6.3: Mean phonon energy $\overline{E}_{ph}$ and Debye temperatures Θ_D for iron derived from various procedures as explained in the text.

variable Θ_D can be removed to a large extent by the use of a reasonably adjusted "pseudo-Debye" model [Hol94, Hol98a].

Temperature Behaviour

Considering the usual quasi-harmonic approximation, the phonon DOS $g(E)$ can be treated as temperature-independent. Consequently, once $g(E)$ is determined at room temperature, the calculation of the complete temperature dependence of thermodynamic properties is possible [JM85]. This is demonstrated in figure 6.10 for $f_{LM}(T)$, $\langle \Delta x^2 \rangle (T)$, $F_{\mathrm{vib}}(T)$, $S_{\mathrm{vib}}(T)$, $U_{\mathrm{vib}}(T)$ and $c_V(T)$ at 0 GPa and 42 GPa.

At $T = 0\,\mathrm{K}$ the crystal lattice is not completely frozen leading to a Lamb-Mössbauer factor $f_{LM}(T=0) \neq 1$ and to a zero-point motion with $\langle \Delta x^2 \rangle \neq 0$. The latter value decreases under pressure from $1.5 \times 10^{-3}\,\mathrm{Å}^2$ at 0 GPa to $1.0 \times 10^{-3}\,\mathrm{Å}^2$ at 42 GPa. Furthermore, the Helmholtz free energy and the internal energy are identical at absolute zero. The value $F_{\mathrm{vib}}(T=0) = U_{\mathrm{vib}}(T=0)$ increases from 41.8 meV/atom to

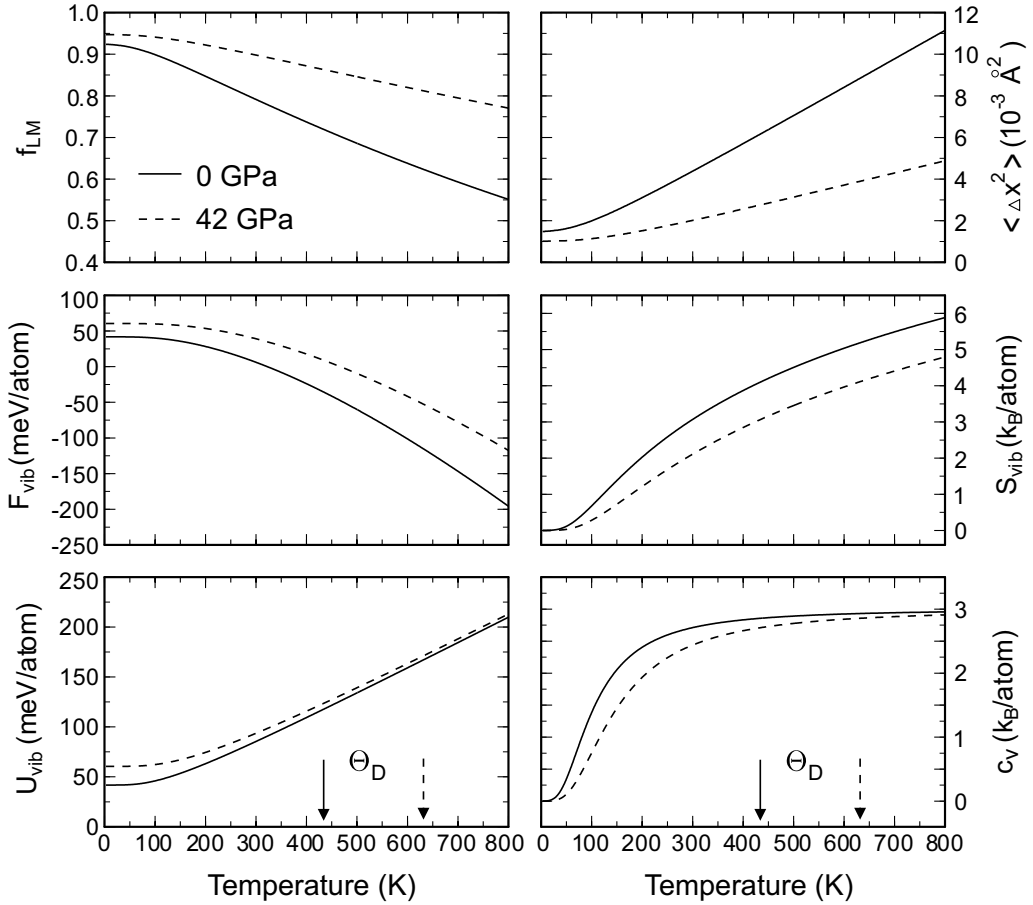

Figure 6.10: Temperature dependence of thermodynamic properties in iron at 0 GPa (solid lines) and 42 GPa (dashed line) derived from the phonon DOS $g(E)$. The corresponding Debye temperatures Θ_D(ht) are depicted at the bottom. S_{vib} represents the temperature derivative of F_{vib} and c_V the derivative of U_{vib}.

60.5 meV/atom at 42 GPa. At high temperature ($T > \Theta_D$) the internal energy U_{vib} approaches the classical behaviour $U_{\mathrm{vib}} = 3\,k_B\,T$. This is also reflected in the specific heat $c_V = (\partial U/\partial T)_V$ where the classical Dulong-Petit value of $3\,k_B$/atom is approached at $T \geq \Theta_D$.

6.4 Discussion

In the following discussion, we concentrate on the Debye temperature Θ_D and its volume dependence, namely the Grüneisen parameter γ_D. Furthermore, the present results for the sound velocity are compared with recent values from ultrasonic and elasticity studies as well as theoretical calculations. Finally, the impact of the derived thermodynamic properties on the α-ε phase transition is discussed.

6.4.1 Grüneisen Parameter

The volume dependence of the phonon DOS can be discussed within the Debye approximation with a common average value γ_D replacing the mode Grüneisen parameters γ_i defined in equation 6.8. Thus, γ_D is related to the average phonon energy $\overline{E}_{ph}$ and can be expressed with the corresponding Debye temperature Θ_D(ht) :

$$\gamma_D = -\,d\ln\Theta_D(ht)/d\ln V\ . \tag{6.23}$$

The left part of figure 6.11 shows the volume dependence of Θ_D(ht) together with a fit according to equation 6.23, including the three points for α-Fe and ε-Fe, respectively. The resulting Grüneisen parameters are γ_D(α-Fe) = 4.3(5) and γ_D(ε-Fe) = 1.5(2).

A similar evaluation for the low-temperature values Θ_D(lt) is depicted in the right part of figure 6.11. The corresponding values $\gamma_{D,lt}$(α-Fe) = 3.4(5) and $\gamma_{D,lt}$(ε-Fe) = 1.3(2) indicate that the volume dependence of the low-energy modes is less pronounced than the average volume dependence.

Both values, γ_D and $\gamma_{D,lt}$, for α-Fe are larger than commonly observed values: The equation for the thermodynamic Grüneisen parameter $\gamma_{th} = \alpha_{\mathrm{V}} K_T V / c_{\mathrm{V}}$ leads to a value for ambient conditions of $\gamma_{th}(V_0)$ = 1.60 (α_{V} = $35.1\times10^{-6}\mathrm{K}^{-1}$ [AM76], K_T = 163 GPa [MBT67], V_0 = 7.093 cm^3/mol [MBT67] and c_{V} = 25.3 J/(K mol) [Kuc82]). Ramakrishan et al. [RBK78] measured γ_{th} up to 3.3 GPa and found $\gamma_{th}(V_0) = 1.66$ and $n = 0.6$, using the form

$$\gamma(V) = \gamma(V_0)\,(V/V_0)^n. \tag{6.24}$$

However, a direct comparison of NIS results with values from ambient or lower pressure is difficult since the NIS results for γ_D represent average values for the pressure

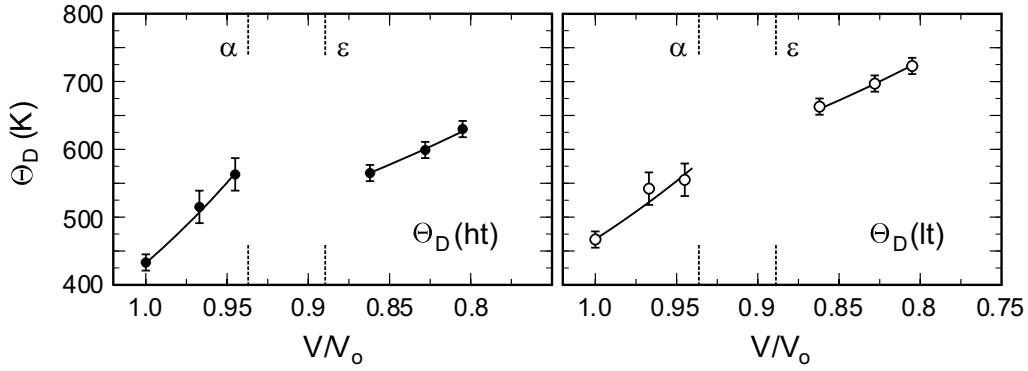

Figure 6.11: Volume dependence of the Debye temperatures Θ_D(ht) and Θ_D(lt). The solid lines represent fits to the experimental data using equation 6.23.

ranges of 0 - 11 GPa (α-Fe) and 20 - 42 GPa (ε-Fe). As shown for example for the γ-α transition in metallic Ce, the Grüneisen parameter can exhibit a strong increase near a high-pressure phase transition [RK80].

A more detailed discussion of the volume dependence of γ, e.g. with equation 6.24 is not possible with the present amount of data. Future NIS studies with further improved flux of SR may provide a larger number of data points in both phases to give a more detailed picture of the high-pressure behaviour of the Grüneisen parameter, especially at the α-ε phase transition.

6.4.2 Aggregate Velocities and Shear Modulus

In order to explain sound velocity data for seismological observations, several recent theoretical investigations deal with the elastic coefficients of hcp iron under strong compression [SC95, SMW96, SSC99]. Due to the difficult experimental access to hcp iron there are little possibilities to compare such calculations with laboratory experiments. Only recently, a new experimental method was developed measuring the lattice strain at high pressure with radial x-ray diffraction [HMS97]. When interpreted in terms of elastic coefficients, this method delivered results on the elastic coefficients in Fe up to 52 GPa [SMH98] and to 211 GPa [MSS98]. However, the interpretation of lattice-strain experiments is controversely discussed and their re-examination is recommended in [SSC99].

The connecting link between seismology and elastic coefficients are the longitudinal (v_p) and transversal sound velocity (v_s), which are determined by the bulk modulus K, the shear modulus G and the density ρ (equations 6.12, 6.13). Although these aggregate velocities can not be obtained directly from the momentum-averaged phonon DOS, they can be determined indirectly when the equation-of-state data is used to provide not only the unit cell volume but also the bulk modulus K at high pressure.

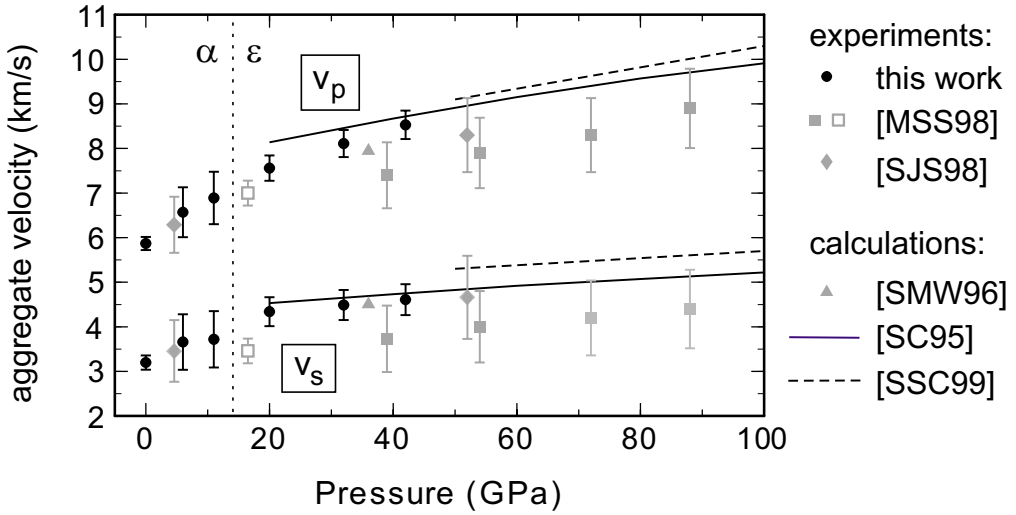

Figure 6.12: Pressure dependence of the aggregate velocities v_p and v_s together with data from the literature. The experimental data points were obtained with lattice-strain (full squares, diamonds) and ultrasound (open square) studies.

In this case, the results for $\overline{v}$ permit the determination of the shear modulus G and the aggregate velocities v_p and v_s from the three equations 6.12, 6.13 and 6.14. The resulting values are listed in table 6.4 and plotted in figure 6.12.

The NIS results for ambient pressure ($G = 81\,\text{GPa}$, $v_p = 5.87\,\text{km/s}$, $v_s = 3.20\,\text{km/s}$, $\overline{v} = 3.57\,\text{km/s}$) are in very good agreement with tabulated values, which were obtained as the mean of the corresponding Voigt and Reuss averages (see section 6.2.3) from

Pressure (GPa)	V/V_0	ρ (g/cm^3)	$\overline{v}$ (km/s)	K (GPa)	G (GPa)	v_p (km/s)	v_s (km/s)
neutron	1	7.86	3.54	163	79	5.84	3.17
0	1	7.86	3.57(10)	163(4)	81(4)	5.87(6)	3.20(10)
6	0.967	8.13	4.10(25)	205(6)	109(12)	6.57(15)	3.66(25)
11	0.945	8.32	4.16(25)	241(6)	115(12)	6.89(15)	3.72(25)
20	0.862	9.12	4.82(15)	292(8)	172(10)	7.56(12)	4.34(15)
32	0.828	9.48	5.00(15)	369(8)	191(10)	8.11(12)	4.49(15)
42	0.805	9.76	5.14(15)	434(8)	207(10)	8.53(12)	4.61(15)

Table 6.4: Elastic properties for iron under pressure. The volume/density data and the bulk moduli K were taken from the compressibility data of α-Fe [MBT67] and ε-Fe [MWC90]. The mean sound velocity $\overline{v}$ is from NIS. The shear modulus G and the aggregate velocities v_p and v_s are derived from equations 6.12, 6.13 and 6.14. The uncertainty of G and v_s is primarily induced by the error in $\overline{v}$, the uncertainty of v_p primarily by the error in K.

single crystal elastic coefficients [SW71]: $G = 80.5(15)$ GPa, $v_p = 5.91(7)$ km/s, $v_s = 3.21(3)$ km/s, $\bar{v} = 3.58(3)$ km/s.[4]

At high pressure, the present results agree with lattice-strain experiments of Singh et al. [SMH98] in both iron phases and with theoretical studies in ε-Fe by Söderlind et al. [SMW96] and Stixrude et al. [SC95]. However, values from recent ultrasound and lattice-strain experiments by Mao et al. [MSS98] are about 20% smaller whereas the theoretical work by Steinle-Neumann et al. [SSC99] tends to give higher aggregate velocities.

6.4.3 The α-ε Phase Transition

With respect to the α-ε phase transition in iron, the present NIS values for the vibrational entropy S_{vib} can be used to determine the slope of the phase boundary in the T, P phase diagram at $T = 294\,K$ (see figure 6.13).

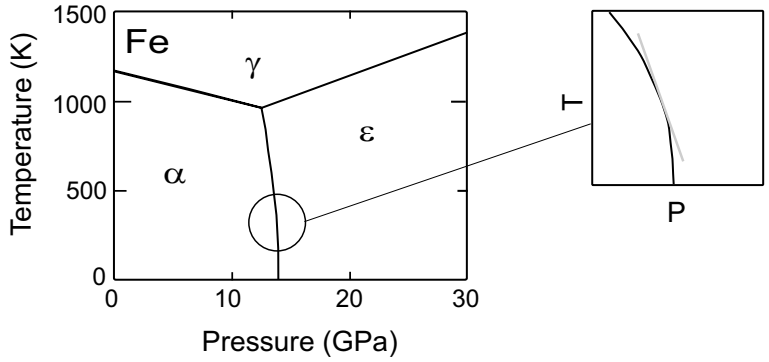

Figure 6.13: Phase diagram of *Fe* showing enlarged the phase boundary between the α- and ε-phase around 294 K, which can be determined with the Clausius-Clapeyron equation 6.25.

The Clausius-Clapeyron equation

$$\frac{dT_{tr}}{dP_{tr}} = \frac{\Delta V}{\Delta S} \tag{6.25}$$

relates the slope dT_{tr}/dP_{tr} of transition temperature T_{tr} versus transition pressure P_{tr} to the volume and entropy differences between the two phases. The value for ΔV at 13 GPa and 294 K can be calculated from the literature data [MBT67, MWC90] and amounts to $\Delta V = -0.344$ cm^3/mol. For an estimation of ΔS, the values of S_{vib} for both iron phases are extrapolated to 13 GPa as shown in figure 6.14. Hereby, the small electronic contribution to the entropy is neglected. With the value of $\Delta S_{\mathrm{vib}} =$

[4]The values in brackets give the mean deviation of the tabulated data sets.

$0.16(2)$ k_B/atom a slope of

$$\frac{dT_{tr}}{dP_{tr}} = -260(40)\,K/GPa \tag{6.26}$$

is obtained for the phase boundary at 294 K.

Due to the sluggish nature of the α-ε transition and the strong variation of the transition pressure for different pressure-transmitting media, values for dT_{tr}/dP_{tr} are difficult to obtain with x-ray diffraction. Consequently, the results in the literature exhibit a large variation. A collection of different values given by Manghnani et al. [MMN87] covers a range of -169 K/GPa up to -455 K/GPa, which is consistent with the NIS result.

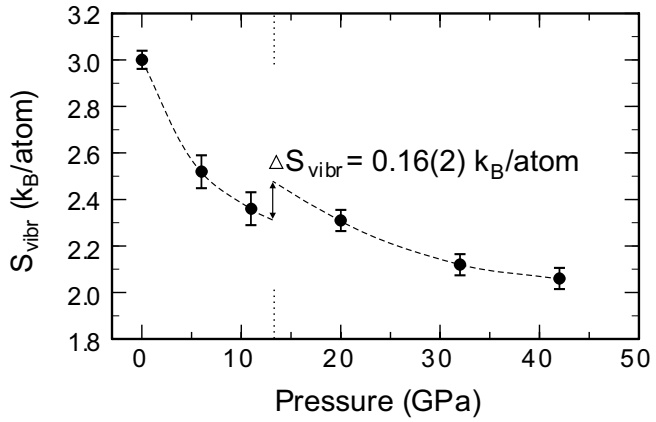

Figure 6.14: Extrapolated pressure dependence of the vibrational entropy S_{vib} for α-Fe and ε-Fe. For the transition pressure at 13 GPa an entropy difference $\Delta S_{vib} = 0.16(2)k_B/$ atom between the two phases is obtained.

The results presented in this chapter represent an extensive characterization of the lattice dynamics of elemental iron under pressure. A geophysical relevance of the work can be derived from the first measurement of the phonon DOS in ε-Fe, which is a major component of the Earth's inner core.

For the derived thermodynamic properties, it should be emphasized that, in contrast to other (e.g. calorimetric) measurements, pure vibrational parts of internal energy, specific heat and entropy are provided. They are free of possible electronic or magnetic contributions and are therefore extremely useful for testing theoretical calculations of thermodynamic parameters responsible for the equation-of-state [SMW96] or the melting temperature of iron [AGP99].

Chapter 7

Summary

In the framework of this thesis the new methods of Nuclear Resonant Scattering of synchrotron radiation have been successfully applied to the investigation of magnetic properties and lattice dynamics under pressure. For this purpose a new generation of diamond-anvil cells has been developed according to the specific properties of synchrotron radiation and the individual needs for Nuclear Forward Scattering (NFS) and Nuclear Inelastic Scattering (NIS).

The NFS experiments were performed on magnetic Laves phases with the composition RFe_2 (R = Y, Gd, Sc) at pressures up to 115 GPa. This pressure range allowed the study of iron magnetism in these model systems with a large variation of interatomic Fe-Fe distances. The competing variation of exchange interactions and Fe band moments is reflected by a systematic change of the *magnetic ordering temperatures* and of the *magnetic ordering type*. The latter varied from ferromagnetism with well-localized Fe moments via antiferromagnetism with more itinerant Fe moments to a non-magnetic state. This behaviour is similar to the observations in elemental iron (γ-Fe), when the lattice parameter is changed. We conclude from comparative studies on $ScFe_2$ that the antiferromagnetic state can only be obtained after a pressure-induced structural phase transformation from the cubic C15 to the hexagonal C14 structure.

It is further demonstrated that the variety of different magnetic phenomena in the RFe_2 series with non-magnetic R atoms can be reproduced by a single model system, namely YFe_2, when exposed to high pressure. A comparison with $GdFe_2$, exhibiting large Gd 4f moments, indicated a strongly increased interaction between the Fe and the Gd sublattices under pressure, which leads to a stabilization of the Fe moment.

The objective of the second part of the thesis was the pioneering application of NIS for the *study of phonons in iron* under pressure. With a new high-pressure technique, based on a Be gasket for sufficient transmission of the Fe $K_{\alpha,\beta}$ x-ray fluorescence, the phonon density of states in the ε-phase of iron was experimentally determined for the first time. From NIS spectra measured in α-Fe and ε-Fe at various pressures up to 42 GPa, a variety of thermodynamic parameters, such as Debye temperatures,

Grüneisen parameters, the Helmholtz free energy and the vibrational contributions to the specific heat and the entropy were derived. Since ε-Fe is the main component of the Earth's solid inner core, the derived *sound velocities* have direct geophysical impact. The present results can be further used to test theoretical *ab initio* calculations, which describe the physics of the Earth's core.

Outlook

The success of the present NFS and NIS studies is intimately connected with the use of synchrotron radiation from 3^{rd} generation sources. Further developments can be expected from improvements in the performance of existing synchrotron facilities and from the instrumentation of the beamlines, where for high-pressure studies the use of focusing optics is most important. In this field, there is already a strong (and fruitful) competition between different groups performing Nuclear Resonant Scattering at ESRF (Grenoble), APS (Argonne, Chicago) and SPring8 (Tsukuba, Japan).

The use of focusing devices was essential for the NIS studies of iron under pressure. The NFS experiments in this thesis were, however, performed without focusing optics. Further high-pressure NFS studies at ESRF would benefit very much from a tenfold increased photon flux on the sample, possible with the focusing elements already in use. Such a gain in photon flux may lead to major improvements of NFS studies in two directions:

- confinement of the measuring time from the order of hours to 5-10 minutes, allowing a systematic study of magnetic ordering temperatures under pressure, and
- diminishing the sample dimensions by an order of magnitude, providing access to pressures well above 200 GPa.

From the geophysical point of view, it is obvious that higher pressures than the present 42 GPa are desirable for NIS experiments on iron; the pressure of the Earth's core varies from 140 GPa to 360 GPa. An actual approach to such high pressures was obtained in recent experiments at APS, where a collaboration between the Geophysical Laboratory (H.K. Mao et al., Washington), APS beamline scientists (W. Sturhahn et al.) and the Paderborn group reached 153 GPa in a NIS study of iron [MXS00].

For both spectroscopic applications, NIS and NFS, high-pressure experiments at elevated temperatures are envisaged. Although relevant temperatures for the Earth's core (6000-8000 K) are far beyond the experimental possibilities, the feasible temperature range up to about 1300 K with electrical heating [DST00] is already sufficient to test theoretical forecasts of temperature-dependent lattice dynamics and to study ordering temperatures of magnetic systems of interest, like the RFe_2 systems with magnetic rare-earth constituents.

Bibliography

[AAM93] J. D. Althoff, P. B. Allen, J. A. Moriarty, *Phase Diagram and Thermodynamic Properties of Solid Magnesium in the Quasiharmonic Approximation*, Phys. Rev. B **48**, 13253 (1993).

[AD97] O. L. Anderson, A. Duba, *Experimental Melting Curve of Iron Revisited*, J. Geophys. Res. B **102**, 22659 (1997).

[ADM86] J. G. M. Armitage, T. Dumelow, R. H. Mitchell, P. C. Riedi, J. S. Abell, P. Mohn, K. Schwarz, *Pressure Dependence of the Magnetisation of YFe_2 and $ZrFe_2$: Computation and Experiment*, J. Phys. F: Met. Phys. **16**, L141 (1986).

[AGP99] D. Alfè, M. J. Gillan, G. D. Price, *The Melting Curve of Iron at the Pressures of the Earth's Core from ab initio Calculations*, Nature **401**, 462 (1999).

[AM76] N. Ashcroft, N. D. Mermin, *Solid State Physics*, Saunders College, Philadelphia (1976).

[And95] O. L. Anderson, *Equations of State of Solids for Geophysics and Ceramic Science*, Oxford University Press (1995).

[And97] O. L. Anderson, *Iron: Beta Phase Frays*, Science **278**, 821 (1997).

[Bar95] A. Q. R. Baron, *Report on the X-ray Efficiency and Time Response of a 1 cm^2 Reach Through Avalanche Diode*, Nucl. Instr. Meth. A **352**, 665 (1995).

[Bar99] A. Q. R. Baron, *Transverse Coherence in Nuclear Resonant Scattering of Synchrotron Radiation*, in: *Nuclear Scattering of Synchrotron Radiation: Principles and Applications* (Edited by E. Gerdau, H. de Waard), Baltzer (1999), in press.

[BB73] M. Brouha, K. H. Buschow, *Pressure Dependence of the Curie Temperature of Intermetallic Compounds of Iron and Rare-Earth Elements, Th, and Zr*, J. Appl. Phys. **44**, 1813 (1973).

[BB90] N. van Bargen, R. Boehler, *Effect of Non-Hydrostaticity on the $\alpha - \varepsilon$ Transition of Iron*, High Press. Res. **6**, 133 (1990).

[BBM74] M. Brouha, K. H. J. Buschow, A. R. Miedema, *Magneto-Volume Effects in Rare-Earth Transition Metal Intermetallics*, IEEE Trans. Mag. **10**, 182 (1974).

[BCG96] A. Q. R. Baron, A. I. Chumakov, H. F. Grünsteudel, H. Grünsteudel, L. Niesen, R. Rüffer, *Transverse X-ray Coherence in Nuclear Scattering of Synchrotron Radiation*, Phys. Rev. Lett. **77**, 4808 (1996).

[BCK90] E. Burzo, A. Chelkowski, H. Kirchmayr, *Compounds of Rare Earth Elements and 3d Elements*, in: *Landolt-Börnstein New Series III: Magnetic properties of rare earth elements, alloys and compounds*, Volume 19d2, Springer, Berlin (1990).

[BCR96] A. Q. R. Baron, A. I. Chumakov, R. Rüffer, H. Grünsteudel, H. F. Grünsteudel, O. Leupold, *Single-Nucleus Quantum Beats Excited by Synchrotron Radiation*, Europhys. Lett. **34**, 331 (1996).

[BD76] K. H. J. Buschow, A. M. van Diepen, *Effect of Hydrogen Absorption on the Magnetic Properties of YFe_2 and $GdFe_2$*, Solid State Comm. **19**, 79 (1976).

[Ber94] U. Bergmann, *Resonant Nuclear Scattering Using Synchrotron Radiation*, PhD thesis, State University of New York at Stony Brook (1994).

[BFM98] U. Buontempi, A. Filliponi, D. Martinez, P. Postorino, M. Mezouar, J. P. Itie, *Anomalous Bond Length Expansion in Liquid Iodine at High Pressure*, Phys. Rev. Lett. **80**, 1912 (1998).

[BGG73] B. Barbara, D. Gignoux, D. Givord, F. Givord, R. Lemaire, *Magnetic Properties of Rare Earth Intermetallic Compounds*, Int. J. Magnetism **4**, 77 (1973).

[BH74] L. M. Barker, R. E. Hollenbach, *Shock Wave Study of the $\alpha - \varepsilon$ Phase Transition in Iron*, J. Appl. Phys. **45**, 4872 (1974).

[BM86] J. M. Brown, R. G. McQueen, *Phase Transitions, Grüneisen Parameter, and Elasticity for Shocked Iron Between 77 GPa and 400 GPa*, J. Geophys. Res. B **91**, 7485 (1986).

[BNJ91] M. S. S. Brooks, L. Nordström, B. Johansson, *Magnetism in RFe_2 Compounds*, J. Appl. Phys. **69**, 5683 (1991).

[Boe93] R. Boehler, *Temperatures in the Earth's Core from Melting-Point Measurements of Iron at High Static Pressures*, Nature **363**, 534 (1993).

[BPM56] D. Bancroft, E. L. Peterson, S. Minshall, *Polymorphism of Iron at High Pressure*, J. Appl. Phys. **27**, 291 (1956).

[BR94] A. Q. R. Baron, S. L. Ruby, *Time Resolved Detection of X-rays Using Large Area Avalanche Photodiodes*, Nucl. Instr. Meth. A **343**, 517 (1994).

[BSH92] U. v. Bürck, D. P. Siddons, J. B. Hastings, U. Bergmann, R. Hollatz, *Nuclear Forward Scattering of Synchrotron Radiation*, Phys. Rev. B, **46**, 6207 (1992).

[BSS99] J. Badro, V. V. Struzhkin, J. Shu, R. J. Hemley, H. K. Mao, C. Kao, J. Rueff, G. Shen, *Magnetism in FeO at Megabar Pressures from X-Ray Emission Spectroscopy*, Phys. Rev. Lett. **83**, 4101 (1999).

[BU79] E. Burzo, I. Ursu, *On the Magnetic Behaviour of Iron in Ternary Gadolinium-Yttrium Compounds*, J. Appl. Phys. **50**, 1471 (1979).

[Buk99] M. S. T. Bukowinski, *Taking the Core Temperature*, Nature **401**, 432 (1999).

[BW97] J. C. Boettger, D. C. Wallace, *Metastability and Dynamics of the Shock-Induced Phase Transition in Iron*, Phys. Rev. B **55**, 2840 (1997).

[CR98] A. I. Chumakov, R. Rüffer, *Nuclear Inelastic Scattering*, Hyp. Int. **113**, 59 (1998).

[CRB96] A. I. Chumakov, R. Rüffer, A. Q. R. Baron, H. Grünsteudel, H. Grünsteudel, *Temperature Dependence of Nuclear Inelastic Absorption of Synchrotron Radiation in α-57Fe*, Phys. Rev. B **54**(14), R9596 (1996).

[Cre92] K. C. Creager, *Anisotropy of the Inner Core from Differential Travel Times of the Phases PKP and PKIKP*, Nature **356**, 309 (1992).

[CS99] A. I. Chumakov, W. Sturhahn, *Experimental Aspects of Inelastic Nuclear Resonance Scattering*, in: *Nuclear Scattering of Synchrotron Radiation: Principles and Applications* (Edited by E. Gerdau, H. de Waard), Baltzer (1999), in press.

[CTW82] G. Cort, R. Taylor, J. Willis, *Search for Magnetism in ε-Fe*, J. Appl. Phys. **53**, 2064 (1982).

[Dep87] P. Deppe, *Mössbauer Untersuchungen einiger neuer Seltenerd-Eisen-Bor-Verbindungen*, PhD thesis, Universität Bochum (1987).

[DRM86] T. Dumelow, P. C. Riedi, P. Mohn, K. Schwarz, Y. Yamada, *Pressure Dependence of the Hyperfine Field of YFe_2 and $ZrFe_2$*, J. Magn. Magnet. Mat. **54-57**, 1081 (1986).

[DST00] L. S. Dubrovinsky, S. K. Saxena, F. Tutti, S. Rekhi, T. LeBehan, *In Situ X-Ray Study of Thermal Expansion and Phase Transition of Iron at Multimegabar Pressure*, Phys. Rev. Lett. **84**, 1720 (2000).

[EEB98] M. Ekman, K. Einarsdotter, P. Blaha, *Ab initio Study of the Martensitic bcc-hcp Transformation in Iron*, Phys. Rev. B **58**, 5296 (1998).

[ESR92] ESRF, *Annual Report* (1992).

[ESR97] ESRF, *Beamline Handbook* (1997).

[ESR96] ESRF, *Annual report* (1995/96).

[FCH98] A. K. Freund, F. Comin, J. Hazemann, P. Hustache, B. Jenninger, K. Lieb, M. Pierre, *Performances of Various Types of Benders for Sagitally Focusing Crystals on ESRF Synchrotron Beamlines*, in: *SPIE Conference 3448, San Diego* (July 1998).

[FPB72] R. A. Forman, G. J. Piermarini, S. Block, Science **176**, 284 (1972).

[GBB81] J. M. Genin, P. Bauer, M. J. Besnus, *Mössbauer Study of the Temperature Dependence of the Magnetization Direction and the Hyperfine Interactions in Laves Phase Compound $GdFe_2$*, Phys. Stat. Sol. a **64**, 325 (1981).

[Gib76] T. C. Gibb, *Principles of Mössbauer Spectropscopy*, Chapman and Hall, London (1976).

[GR66] G. Gilat, L. J. Rubenheimer, *Accurate Numerical Method for Calculating Frequency-Distribution Functions in Solids*, Phys. Rev. **144**, 390 (1966).

[Grü97] H. F. Grünsteudel, *Der $\alpha - /\varepsilon$–Übergang in Eisen als Beispiel für nukleare Vorwärtsstreuung von Synchrotronstrahlung an Proben unter hohem Druck*, PhD thesis, Universität Paderborn (1997).

[GRW85] E. Gerdau, R. Rüffer, H. Winkler, W. Tolksdorf, C. P. Klages, J. P. Hannon, *Nuclear Bragg Diffraction of Synchrotron Radiation in Yttrium Iron Garnet*, Phys. Rev. Lett. **54**(8), 835 (1985).

[Gsc64] K. A. Gscheidner, *Physical Properties and Interrelationships of Metallic and Semimetallic Elements*, Solid State Phys. **16**, 275 (1964).

[GSW98] H. Giefers, M. Strecker, G. Wortmann, K. Attenkofer, J. Przewoznik, A. Fontaine, F. Baudelet, *XMCD of Gd Garnets and Laves Phases Under High Pressure*, ESRF Report HE-371 (1998).

[Hei67] V. Heine, *s-d Interaction in Transition Metals*, Phys. Rev. **153**, 673 (1967).

[Hes97] H.-J. Hesse, *Hochdruckuntersuchungen zur Eu-Valenz in intermetallischen EuM_2Ge_2-Systemen (M = Ni, Pd, Pt)*, PhD thesis, Universität Paderborn (1997).

[HMS97] R. J. Hemley, H. K. Mao, G. Shen, J. Badro, P. Gillet, M. Hanfland, D. Häusermann, *X-Ray Imaging of Stress and Strain of Diamond, Iron, and Tungsten at Megabar Pressures*, Science **276**, 1242 (1997).

[Hol75] W. B. Holzapfel, *Mössbauer Studies at High Pressure*, CRC Critical Reviews in Solid State Sciences, 89 (1975).

[Hol94] W. B. Holzapfel, *Approximate Equations of State for Solids from Limited Data Sets*, J. Phys. Chem. Sol. **55**, 711 (1994).

[Hol96] W. B. Holzapfel, *Physics of Solids Under Strong Compression*, Rep. Prog. Phys. **59**, 29 (1996).

[Hol98a] W. B. Holzapfel, *Equations of State for Solids Under Strong Compression*, High Press. Res. **16**, 81 (1998).

[Hol98b] W. B. Holzapfel, *Hochdruck in Natur und Technik*, Forschungs Forum Paderborn **1**, 54 (1998).

[HSB91] J. B. Hastings, D. P. Siddons, U. van Bürck, R. Hollatz, U. Bergmann, *Mössbauer Spectroscopy Using Synchrotron Radiation*, Phys. Rev. Lett. **66**(6), 770 (1991).

[HT94] J. P. Hannon, G. T. Trammell, *Resonant γ-ray Scattering and Coherent Excitations of Nuclei*, in: *Resonant Anomalous X-Ray Scattering* (Edited by G. Materlik, C. J. Sparks, K. Fischer). Elsevier Science B.V. (1994).

[IFF92] IFF, *Synchrotronstrahlung zur Erforschung kondensierter Materie. 23. IFF Ferienkurs*, Kernforschungszentrum Jülich GmbH, Institut für Festkörperforschung (1992).

[IGS78] R. Ingalls, G. A. Garcia, E. A. Stern, *X-Ray Absorption at High Pressure*, Phys. Rev. Lett. **40**, 334 (1978).

[IYI92] T. Ishikawa, Y. Yoda, K. Izumi, C. K. Suzuki, X. W. Zhan, M. Ando, S. Kikuta, *Constuction of a Precision Diffractometer for Nuclear Bragg Scattering at the Photon Factory*, Rev. Sci. Instr. **63**, 1015 (1992).

[Jac75] J. D. Jackson, *Classical Electrodynamics*, Whiley, New York (1975).

[Jay83] A. Jayaraman, *Diamond Anvil Cell and High-Pressure Physical Investigations*, Rev. Mod. Phys. **55**, 65 (1983).

[Jil91] D. Jiles, *Introduction to Magnetism and Magnetic Materials*, Chapman and Hall, London (1991).

[JM85] W. Jones, N. H. March, *Theoretical Solid State Physics*, Volume 1, p. 273, Dover Publications, Inc., New York (1985).

[KAK79] Y. Kagan, A. M. Afanas'ev, V. G. Kohn, *On Excitation of Isomeric Nuclear States in a Crystal by Synchrotron Radiation*, J. Phys. C **12**, 615 (1979).

[KAO97] C. Keppler, K. Achterhold, A. Ostermann, U. van Bürck, W. Potzel, A. I. Chumakov, A. Q. R. Baron, R. Rüffer, F. Parak, *Determination of the phonon spectrum of iron in myoglobin using inelastic X-ray scattering of synchrotron radiation*, Biophys. Letter **25**, 221 (1997).

[KB76] G. L. Kinsland, W. A. Bassett, *Modification of the Diamond Dell for Measuring Strain and the Strength of Materials at Pressures up to 300 kbar*, Rev. Sci. Instr. **47**, 130 (1976).

[KBB97] S. Klotz, J. M. Besson, M. Braden, K. Karch, P. Pavone, D. Strauch, W. G. Marshall, *Pressure Induced Frequency Shifts of Transverse Acoustic Phonons in Germanium to 9.7 GPa*, Phys. Rev. Lett. **79**, 1313 (1997).

[KBS95] S. Klotz, J. M. Besson, M. SchwoererBoehning, R. J. Nelmes, M. Braden, L. Pintschovius, *Phonon Dispersion Measurements at High Pressures to 7 GPa by Inelastic Neutron Scattering*, Appl. Phys. Lett. **66**, 1557 (1995).

[KCR98] V. G. Kohn, A. I. Chumakov, R. Rüffer, *Nuclear Resonant Inelastic Absorption of Synchrotron Radiation in an Anisotropic Crystal*, Phys. Rev. B **58**, 8437 (1998).

[Kis91] S. Kishimoto, *An Avalanche Photo Diode Detector for X-Ray Timing Measurements*, Nucl. Instr. Meth. A **309**, 603 (1991).

[KMM97] M. H. Krisch, A. Mermet, A. S. Miguel, F. Sette, C. Masciovecchio, G. Ruocco, R. Verbeni, *Acoustic-Phonon Dispersion in CdTe at 7.5 GPa*, Phys. Rev. B **56**, 8691 (1997).

[KSF95] D. Keavey, D. F. Storm, J. W. Freeland, I. L. Grigorov, J. C. Walker, *Site-Specific Mössbauer Evidence of Structure-Induced Magnetic Phase Transition in fcc Fe(100) Thin Films*, Phys. Rev. Lett. **74**, 4531 (1995).

[Kuc82] H. Kuchling, *Taschenbuch der Physik*, Harri Deutsch, Frankfurt/Main (1982).

[LAB95] C. Larica, K. M. B. Alves, E. Baggio-Saitovitch, *The Effects of High-Energy Milling on the Structural and Hyperfine Properties of YFe_2*, J. Mag. Magn. Mater. **145**, 306 (1995).

[LBC94] J. P. Liu, F. R. de Boer, P. F. de Chatel, R. Coehoorn, K. H. J. Buschow, *On the 4f-3d Exchange Interaction in Intermetallic Compounds*, J. Magn. Magnet. Mat. **132**, 159 (1994).

[LHZ96] J. Lu, H. J. Hesse, J. Zukrowski, J. Przewoznik, G. Wortmann, *Effect of Pressure and Temperature on the Magnetic Properties of $TiFe_2$*, in: *Conference Proceedings "ICAME-95"* (Edited by I. Ortalli), p. 243. SIF, Bologna (1996).

[Lip60] H. J. Lipkin, *Some Simple Features of the Mössbauer Effect*, Ann. of Phys. **9**, 332 (1960).

[Lip95] H. J. Lipkin, *Mössbauer Sum Rules for Use with Synchrotron Radiation*, Phys. Rev. B **52**, 10073 (1995).

[LLH96] P. Loubeyre, R. LeToullec, D. Häusermann, M. Hanfland, R. J. Hemley, H. K. Mao, L. W. Finger, *X-Ray Diffraction and Equation of State of Hydrogen at Megabar Pressures*, Nature **383**, 702 (1996).

[LPH99] R. Lübbers, M. Pleines, H.-J. Hesse, G. Wortmann, H. F. Grünsteudel, R. Rüffer, O. Leupold, J. Zukrowski, *Magnetism Under High Pressure Studied by Fe-57 and Eu-151 Nuclear Scattering of Synchrotron Radiation*, Hyp. Int. **120/121**, 49 (1999).

[LRW00] R. Lübbers, K. Rupprecht, G. Wortmann, *High-Pressure Mössbauer Studies of Magnetism in RFe_2 Laves Phases and Eu-Chalkogenides*, submitted to Hyp. Int.

[LTW99] P. Loubeyre, R. Toullec, E. Wolanin, M. Hanfland, D. Häusermann, *Modulated Phases and Proton Centring in Ice Observed by X-Ray Diffraction up to 170 GPa*, Nature **397**, 503 (1999).

[Lu00] J. Lu, PhD thesis, Universität Paderborn (2000).

[MBS78] H. K. Mao, P. M. Bell, D. J. Steinberg, J. Appl. Phys. **49**, 3276 (1978).

[MBT67] H. K. Mao, W. A. Bassett, T. Takahashi, *Effect of Pressure on Crystal Structure and Lattice Parameters of Iron up to 300 kbar*, J. Appl. Phys. **38**, 272 (1967).

[MH98] H. K. Mao, R. J. Hemley, *New Windows on the Earth's Deep Interior*, in: *Ultrahigh-Pressure Mineralogy: Physics and Chemistry of the Earth's Deep Interior* (Edited by R. J. Hemley), Mineralogical Society of America, Washington D.C. (1998).

[MJ96] E. G. Moroni, T. Jarlborg, *B.c.c. and h.c.p. phase competition in Fe*, Europhys. Lett. **33**, 223 (1996).

[MMH69] W. H. McMaster, J. H. Mallett, J. H. Hubbell, *Compilation of X-Ray Cross Sections*, Lawrence Livermore Laboratory, Livermore (1969).

[MMN87] M. H. Manghnani, L. C. Ming, N. Nakagiri, *High-Pressure Research in Mineral Physics*, Chapter Investigation of the α-ε Phase Transition by Synchrotron Radiation, p. 155, Terra Scientific Publishing Company, Tokyo (1987).

[Moo51] P. B. Moon, Proc. Phys. Soc., London **A 64**, 76 (1951).

[Mös58a] R. L. Mössbauer, *Kernresonanzfluoreszenz von Gammastrahlung in Ir-191*, Z. Phys. **151**, 124 (1958).

[Mös58b] R. L. Mössbauer, *Kernresonanzfluoreszenz von Gammastrahlung in Ir-191*, Naturwissenschaften **45**, 538 (1958).

[MS85] P. Mohn, K. Schwarz, *Binding Mechanism and Itinerant Magnetism of $ZrFe_2$ and YFe_2*, Physica B **130**, 26 (1985).

[MSN67] V. J. Minkiewicz, G. Shirane, R. Nathans, *Phonon Dispersion Relation for Iron*, Phys. Rev. **162**, 528 (1967).

[MSS98] H. K. Mao, J. Shu, G. Shen, R. J. Hemley, B. Li, A. K. Singh, *Elasicity and rheology of iron above 220 GPa and the nature of the Earth's inner core*, Nature **396**, 741 (1998), and Nature **399**, 280 (1999).

[MWC90] H. K. Mao, Y. Wu, L. C. Chen, J. F. Shu, A. P. Jephcoat, *Static Compression of Iron to 300 GPa and $Fe_{0.8}Ni_{0.2}$ Alloy to 260 GPa: Implications for Composition of the Core*, J. Geophys. Res. B **95**, 21737 (1990).

[MXS00] H. K. Mao, J. Xu, V. V. Struzhkin, R. J. Hemley, W. Sturhahn, M. Y. Hu, E. E. Alp, L. Vacadlo, D. Alfè, G. D. Price, M. J. Gillan, M. Schwoerer-Böhning, D. Häusermann, P. Eng, G. Shen, H. Giefers, R. Lübbers, G. Wortmann, *Phonon Density of States of Iron up to 153 GPa*, submitted to Phys. Rev. Lett.

[Nes98] F. Nessel, *EXAFS Untersuchungen des temperaturinduzierten Phasenübergangs in YMn_2 sowie an LaOCl unter hohem Druck*, Diploma thesis, Universität Paderborn (1998).

[NMR98] L. Niesen, A. Mugarza, M. F. Rosu, R. Coehoorn, R. M. Jungblut, F. Roozeboom, A. Q. R. Baron, A. I. Chumakov, R. Rüffer, *Magnetic Behavior of probe layers of ^{57}Fe in thin Fe films by means of nuclear resonant scattering of synchrotron radiation*, Phys. Rev. B **58**, 8590 (1998).

[NY85] Y. Nishihara, Y. Yamaguchi, *Magnetic structures in the $Sc_{1-x}Ti_xFe_2$ system – Magnetic phase transitions in itinerant electron systems*, J. Phys. Soc. Japan **54**, 1122 (1985).

[NY86] Y. Nishihara, Y. Yamaguchi, *Magnetic properties of the $Sc_{1-x}Ti_xFe_2$ system having two magnetic states with different degrees of localization*, J. Phys. Soc. Japan **55**, 920 (1986).

[OJ97] H. Olijnyk, A. P. Jephcoat, *Effect of Pressure on Raman Phonons in Zirconium Metal*, Phys. Rev. B **56**, 10751 (1997).

[Ols97] P. Olson, *Probing Earth's dynamo*, Nature **389**, 337 (1997).

[PBD61] R. V. Pound, G. B. Benedek, R. Drever, *Effect of Hydrostatic Compression on the Energy of the 14.4-keV Gamma Ray From ^{57}Fe in Iron*, Phys. Rev. Lett. **7**, 405 (1961).

[PCR99] L. Paolasini, R. Caciuffo, B. Roessli, G. H. Lander, K. Myers, P. Canfield, *Iron spin waves in YFe_2 and UFe_2*, Phys. Rev. B **59**, 6867 (1999).

[PLS99] M. Pleines, R. Lübbers, M. Strecker, G. Wortmann, O. Leupold, J. Metge, Y. Shvyd'ko, E. Gerdau, *Pressure-Induced Valence Transition in $EuNi_2Ge_2$ Studied by Eu-151 Nuclear Forward Scattering of Synchrotron Radiation*, Hyp. Int. **120/121**, 181 (1999).

[PT89] M. P. Pasternak, R. D. Taylor, Hyp. Int. **47**, 415 (1989).

[PT96] M. P. Pasternak, R. D. Taylor, in: *Mössbauer Spectroscopy Applied to Magnetism and Materials Science*. Plenum Press, New York (1996).

[PTJ97] M. P. Pasternak, R. Taylor, R. Jeanloz, X. Li, J. Nguyen, C. McCammon, *High Pressure Collapse of Magnetism in $Fe_{0.94}O$: Mössbauer Spectroscopy Beyond 100 GPa*, Phys. Rev. Lett. **79**, 5046 (1997).

[RBK78] J. Ramakrishan, R. Boehler, G. C. Kennedy, *Behaviour of Grüneisen's parameter of some metals at high pressures*, J. Geophys. Res. B **83**, 3535 (1978).

[Rei00] G. Reiss, *Energiedispersive Röntgenbeugungsuntersuchungen an einigen Laves-Phasen unter hohem Druck*, PhD thesis, Universität Paderborn (2000).

[Ric98a] M. Richter, *Band Structure Theory of Magnetism in 3d-4f Compounds*, J. Phys. D: Appl. Phys. **31**, 1017 (1998).

[Ric98b] M. Richwin, *Focusing of X-Rays Using Compound Refractive Lenses*, Diploma thesis, RWTH Aachen (1998).

[RK80] J. Ramakrishnan, G. C. Kennedy, *Anomalous Behavior of the Grüneisen Parameter in Cerium Near the High-Pressure Phase Transition*, J. Appl. Phys., **51**, 2586 (1980).

[RL94] J. Röhler, R. Lübbers, *The Valence of Elemental Praseodym in the Collapsed "Pr IV" Phase from L_{III} X-Ray Absorption up to 260 kbar*, Physica C **235-240**, 1031 (1994).

[RL95] J. Röhler, R. Lübbers, *X-Ray Absorption Study of the "Pr III" - "Pr IV" Transition in Elemental Praseodymium*, Physica B **206 & 207**, 368 (1995).

[Rub74] S. L. Ruby, *Mössbauer Experiments without Conventional Sources*, J. Phys. **C6**, 209 (1974).

[Rup99a] K. Rupprecht, *Hochdruck-Mössbaueruntersuchungen zum Magnetismus von RFe_2 Laves-Phasen*, Diploma thesis, Universität Paderborn (1999).

[Rup99b] K. Rupprecht, *private communication* (1999).

[RW99] K. Rupprecht, G. Wortmann, *Nuclear Scattering of Eu-151 21.5 keV-radiation: High-Pressure Studies of Magnetism in CsCl-type EuS, EuSe, EuTe*, ESRF Report HE-592 (1999).

[SAS73] E. Schreiber, O. L. Anderson, N. Soga, *Elastic Constants and their Measurement*, McGraw-Hill, New York (1973).

[SB62] E. J. Seppi, F. Böhm, *Nuclear Resonance Excitation Using a Diffraction Monochromator*, Phys. Rev. **128**, 2334 (1962).

[SC95] L. Stixrude, R. E. Cohen, *High-Pressure Elasticity of Iron and Anisotropy of Earth's Inner Core*, Science **267**, 1972 (1995).

[Sco74] J. H. Scofield, *Exchange Corrections of K X-Ray Emission Rates*, Phys. Rev. A **9**, 1041 (1974).

[SG94] W. Sturhahn, E. Gerdau, *Evaluation of Time Differential Measurements of Nuclear Resonance Scattering of X-Rays*, Phys. Rev. B **49**, 9285 (1994).

[SGG98] M. Strecker, H. Giefers, S. György, K. Attenkofer, G. Wortmann, *A Versatile High-Pressure Cell for XAS and XMCD in the Energy Range 6-10 keV*, HASYLAB Jahresbericht, p. 839 (1998).

[SH72] D. A. Shirley, H. Haas, Ann. Rev. Phys. Chem. **23**, 385 (1972).

[She98] G. Shen, *private communication* (1998).

[SJ98] R. F. Sabiryanov, S. S. Jaswal, *Electronic Structure and Magnetic Properties of Y-Fe Compounds*, Phys. Rev. B **57**, 7767 (1998).

[SKS96] A. Snigirev, V. Kohn, I. Snigireva, B. Lengeler, *A Compound Refractive Lens for Focusing High-Energy X-Rays*, Nature **384**, 49 (1996).

[SMH98] A. K. Singh, H. K. Mao, R. J. Hemley, *Estimation of Single-Crystal Elastic Moduli from Polycrystalline X-Ray Diffraction at High Pressure: Application to FeO and Iron*, Phys. Rev. Lett. **80**, 2157 (1998).

[Smi96] G. V. Smirnov, *Nuclear Resonant Scattering of Synchrotron Radiation*, Hyp. Int. **97/98**, 551 (1996).

[SMW96] P. Söderlind, J. A. Moriarty, J. M. Wills, *First-principles Theory of Iron up to Earth-Core pressures: Structural, Vibrational and Elastic Properties*, Phys. Rev. B **53**, 14063 (1996).

[Squ78] G. L. Squires, *Introduction to the Theory of Thermal Neutron Scattering*, Cambridge University Press, Cambridge (1978).

[SR96] X. Song, P. G. Richards, *Seismological Evidence for Differential Rotation of the Earth's Inner Core*, Nature **382**, 221 (1996).

[SRF84] S. Sinnema, R. J. Radwanski, J. J. M. Franse, D. B. deMooij, K. Buschow, *Magnetic Properties of Ternary Rare-Earth Compounds of the Type $R_2Fe_{14}B$*, J. Mag. Magnet. Mat. **44**, 333 (1984).

[SS60] K. S. Singwi, A. Sjölander, *Resonance Absorption of Nuclear Gamma Rays and Dynamics of Atomic Motions*, Physical Review **120**(4), 1093 (1960).

[SSC99] G. Steinle-Neumann, L. Stixrude, R. Cohen, *First-principles Elastic Constants for the hcp Transition Metals Fe, Co, and Re at High Pressure*, Phys. Rev. B **60**, 791 (1999).

[STA95] W. Sturhahn, T. S. Toellner, E. E. Alp, X. Zhang, M. Ando, Y. Yoda, S. Kikuta, M. Seto, C. W. Kimball, B. Dabrowski, *Phonon Density of States Measured by Inelastic Nuclear Resonant Scattering*, Phys. Rev. Lett. **74**, 3832 (1995).

[Str00] M. Strecker, PhD thesis, Universität Paderborn (2000).

[SW71] G. Simmons, H. Wang, *Single Crystal Elastic Constants and Calculated Aggregate Properties*, MIT Press, Cambrigde, MA (1971).

[SW99] M. Strecker, G. Wortmann, *High-Pressure ^{155}Gd-Mössbauer Study of Magnetic Properties in $GdMn_2$ Laves Phases (M=Mn,Fe,Al)*, Hyp. Int. **120/121**, 187 (1999).

[SYK95] M. Seto, Y. Yoda, S. Kikuta, X. Zhang, M. Ando, *Observation of Nuclear Resonant Scattering Accompanied by Phonon Excitation Using Synchrotron Radiation*, Phys. Rev. Lett. **74**, 3828 (1995).

[TP90] R. D. Taylor, M. P. Pasternak, *Sub-Megabar Mössbauer Studies Using Diamond Anvil Cells*, Hyp. Int. **53**, 159 (1990).

[TPJ91] R. D. Taylor, M. P. Pasternak, R. Jeanloz, *Hysteresis in the High Pressure Transformation of bcc- to hcp-Iron*, J. Appl. Phys. **69**, 6126 (1991).

[WBI72] D. L. Williamson, S. Bukshpan, R. Ingalls, *Search for Magnetic Ordering in hcp Iron*, Phys. Rev. B **6**, 4194 (1972).

[Web95] S. Weber, *Röntgenbeugung an metallischen LnM_2 Verbindungen unter Druck*, Diploma thesis, Universität Paderborn (1995).

[WI98] F. M. Wang, R. Ingalls, *Iron bcc-hcp Transition: Local Structure from X-Ray-Absorption Fine Structure*, Phys. Rev. B **57**, 5647 (1998).

[Wil96] K. Wille, *Physik der Teilchenbeschleuniger und Synchrotronstrahlungsquellen*, Teubner, Stuttgart (1996).

[Woh81] E. P. Wohlfahrt, *Metallic Magnetism Under High Pressure*, in: *Physics of Solids Under High Pressure* (Edited by J. S. Shilling, R. N. Shelton), p. 175, North-Holland Publishing Company (1981).

[WW81] D. Wagner, E. Wohlfahrt, *The Pressure Dependence of the Curie Temperature of Heterogenous Ferromagnetic Alloys*, J. Phys. F: Metal Phys. **11**, 2417 (1981).

[YAC95] C. S. Yoo, J. Akella, A. J. Campbell, H. K. Mao, R. J. Hemley, *The Phase Diagram of Iron by in situ x-ray Diffraction: Implications for Earth's Core*, Science **270**, 1473 (1995).

[You91] D. A. Young, *Phase Diagrams of the Elements*, Universiy of California Press, Berkeley (1991).

[ZS87] J. Zarestky, C. Stassis, *Lattice Dynamics of γ-Fe*, Phys. Rev. B **35**, 4500 (1987).

Danksagung

Die Arbeit mit Synchrotronstrahlung ist nichts für Einzelkämpfer. Ich möchte daher allen danken, die mich auf meiner *Reise ins Innere der Erde* unterstützt haben:

Mein besonderer Dank gilt Prof. Gerhard Wortmann. Sein großes Engagement für das Forschungsprojekt hat entscheidend zum Gelingen der Arbeit beigetragen. Es hat viel Spaß gemacht, mit ihm zu arbeiten und ich denke, wir waren ein gutes Team. Herzlich danken möchte ich ihm auch für seine ortskundigen Führungen in Chicago und zum Grab des Wildschütz' Jennerwein.

Bei den verbliebenen Gruppenmitgliedern Kirsten Rupprecht und Hubertus Giefers bedanke ich mich für die Unterstützung vor und während der Strahlzeiten und das gute Arbeitsklima. Kirstens Ordnungssinn im gemeinsamen Büro machte das Leben leichter, genau wie die sehr amüsanten Hamburgermahlzeiten mit Hubertus in Chicago.

Ich danke auch den ehemaligen Mitgliedern der Arbeitsgruppe für ihre Hilfe. Marianne Pleines und Hans-Josef Hesse waren meine Mitstreiter bei den NFS-Experimenten in Grenoble. Meinem Weggefährten aus Diplomzeiten, Matthias Strecker, danke ich für Diskussionen über den Magnetismus als solchen und für viele Jahre guter Zusammenarbeit. Mein großer Rückhalt im Mössbauerlabor war Jiangang Lu; seine Spektren waren mir bei den NFS-Auswertungen eine wichtige Stütze. Viel Spaß bei den Experimenten in Hamburg hatte ich mit Jens Dumschat. Genau wie Stephan I. Györy, Frank Nessel und Günther Nowitzke gehört er noch zu meinem früheren Leben mit Röntgenabsorptionsspektrospie.

Wie schon zu Zeiten der Diplomarbeit, war die Zusammenarbeit mit der Hochdruckgruppe von Prof. Wilfried Holzapfel hervorragend. Mit Prof. Holzapfel hatte ich einen äußerst kompetenten Diskussionspartner in vielen Bereichen der Hochdruckphysik, besonders auf dem Gebiet der Gitterdynamik. Gerd Reiss und Felix Porsch danke ich für die gute Kooperation bei den Laves-Phasen. (Was hätte ich wohl ohne Eisenabstände unter Druck gemacht?) Andreas Schiwek hat freundlicherweise einige Kapitel dieser Arbeit durchgesehen. Thomas Tröster, Werner Sievers und Wilfried Bröckling waren immer gute Ansprechpartner, wenn es um neue Entwicklungen in der Hochdrucktechnik ging.

Der Beitrag von Herrn Franz Risse und seinen Mitarbeitern der mechanischen Werkstatt bei der Planung und Ausführung dieser Entwicklungen ist gar nicht hoch genug einzuordnen.

Die Arbeit an internationalen Forschungseinrichtungen wie dem ESRF in Grenoble kann nur erfolgreich sein, wenn man eine engagierte und hilfsbereite Mannschaft vor Ort antrifft. Hanne und Hermann Grünsteudel, Olaf Leupold, Joachim Metge, Alessandro Barla, Sasha Chumakov, Alfred Baron und Rudolf Rüffer waren so eine Mannschaft, mit der die Strahlzeiten auch noch viel Spaß machten. Hanne und Hermann waren dabei fast wie eine französische Familie für mich. Hermann und Sasha danke ich zudem für die besonders erfolgreiche Zusammenarbeit, die zur Veröffentlichung in *Science* führte.

Der Kölner Gruppe von Prof. Mohsen Abd-Elmeguid danke ich für viele interessante Stunden beim ESRF mit anregenden Diskussionen.

Obwohl die Zinn-Experimente nicht in dieser Arbeit auftauchen, danke ich dem Team um Wolfgang Sturhahn bei APS in Chicago für die freundliche Aufnahme in der neuen Welt.

Meiner lieben Mutter und meinen Schwestern mit ihren Familien habe ich es zu verdanken, dass ich die Verbindung zur Oberfläche der Erde nicht verlor. Sie haben mich in allen Phasen der Arbeit treu unterstützt. Das Gleiche gilt auch für meine Schwiegereltern, die mir während meiner Reisen und auch sonst so oft den Rücken frei gehalten haben.

Mein letzter und herzlichster Dank gilt meiner wunderbaren Frau Nataly. Sie musste viel Verständnis dafür aufbringen, dass man für eine Reise ins Innere der Erde erst zweimal drumherum fliegen muss. Ihr und unseren beiden Töchtern Johanna und Pauline ist diese Arbeit gewidmet.

Publications

1. J. Röhler and R. Lübbers, *The Valence of Elemental Praseodym in the Collapsed "Pr IV"-Phase from L_{III} X-Ray-Absorption up to 260 kbar,* Physica C **235-240**, 1031 (1994).

2. J. Röhler and R. Lübbers, *X-Ray Absorption Study of the "Pr III" - "Pr IV" Transition in Elemental Praseodymium,* Physica B **206 & 207**, 368 (1995).

3. H. Welker, H.F. Grünsteudel, G. Ritter, R. Lübbers, H.-J. Hesse, G. Nowitzke, G. Wortmann and H.A. Goodwin, *Combined Mössbauer and EXAFS Study of the High-spin/Low-spin Transition in $[Fe(II)(bpp)_2](BF_4)_2$,* Conf. Proc. Vol.50 (SIF Bologna), (1996) p. 19-22.

4. R. Lübbbers, G. Nowitzke, H.A. Goodwin and G. Wortmann, *X-Ray Absorption Study of the High-spin/Low-spin Transition in $[Fe(II)(bpp)_2](BF_4)_2$,* J. Phys. IV France **7**, C2-651 (1997).

5. R. Lübbers, J. Dumschat, G. Wortmann and E. Bauer, *Temperature and Pressure Induced Valence Transitions in $YbCu_{5-x}Ga_x$ Studied by Yb-L_{III} XANES,* J. Phys. IV France **7**, C2-1021 (1997).

6. G. Nowitzke, H. Meier, R. Lübbers, J. Dumschat and G. Wortmann, *EXAFS Study of Oxygen Distortions in Gd_2CuO_4 as Function of Temperature and Pressure,* J. Phys. IV France **7**, C2-1023 (1997).

7. J. Dumschat, R. Lübbers, I. Felner, G. Lucazeau and G. Wortmann, *(Tb,Ce)-L_{III} XAS High-pressure Study of Tetravalent $BaTbO_3$ and $SrCeO_3$,* J. Phys. IV France **7**, C2-1019 (1997).

8. H.-J. Hesse, R. Lübbers, M. Winzenick, H.W. Neuling, G. Wortmann, *Pressure and Temperature Dependence of the Eu Valence in $EuNi_2Ge_2$ and Related Systems Studied by Mössbauer Effect, X-ray Absorption and XRD,* J. Alloys and Compounds **246**, 220-232 (1997).

9. R. Lübbers, H.-J. Hesse, H.F. Grünsteudel, R. Rüffer, J. Zukrowski and G. Wortmann, *Probing Magnetism in the Mbar Range,* ESRF Highlights 1996/97, p. 56-57

10. R. Lübbers, H.-J. Hesse, H.F. Grünsteudel, R. Rüffer, J. Zukrowski and G. Wortmann, *High-Pressure Studies of Magnetism by Nuclear Scattering of Synchrotron Radiation,* Proc. 2^{nd} Russian-German Workshop on Synchrotron Radiation Research, in: Poverhnost 1998, Vol. 8-9, p.134-139 (Russian Acad. Science), engl. transcription: "Surface Investigations: X-Ray, Synchrotron and Neutron Techniques" (Gordon & Breach, 1999).

11. R. Lübbers, M. Pleines, H.-J. Hesse, G. Wortmann, H.F. Grünsteudel, R. Rüffer, O. Leupold, J. Zukrowski, *Magnetism Under High Pressure Studied by Fe-57 and Eu-151 Nuclear Scattering of Synchrotron Radiation,* Hyperfine Interactions **120/121**, 49-58 (1999).

12. M. Pleines, R. Lübbers, M. Strecker, G. Wortmann, O. Leupold, J. Metge, Yu.V. Shvyd'ko, E. Gerdau, *Pressure-Induced Valence Transition in $EuNi_2Ge_2$ Studied by Eu-151 Nuclear Forward Scattering of Synchrotron Radiation,* Hyperfine Interactions **120/121**, 181-185 (1999).

13. O. Leupold, E. Gerdau, M. Gerken, H.D. Rüter, R. Lübbers, M. Pleines, M. Strecker, G. Wortmann, *Charge Fluctuations and Magnetism Studied by Nuclear Forward Scattering at the Eu-151 Resonance,* ESRF Highlights 1997/1998, p.37-39.

14. R. Lübbers, G. Wortmann, H.F. Grünsteudel, *High-Pressure Studies with Nuclear Scattering of Synchrotron Radiation,* Chapter in: "Nuclear Scattering of Synchrotron Radiation: Principles and Applications", edited by E. Gerdau and H. de Waard, Baltzer, 1999, in print (33 pages).

15. G. Wortmann and R. Lübbers, *Forschung mit Synchrotronstrahlung*, Forschungs-Forum Paderborn **3**, 52-56 (2000).

16. R. Lübbers, H.F. Grünsteudel, A.I. Chumakov, G. Wortmann, *Density of Phonon States in Iron at High Pressure,* Science **287**, 1250-1253 (2000).

17. R. Lübbers, K. Rupprecht, G. Wortmann, *High-Pressure Mössbauer Studies of Magnetism in RFe_2 Laves Phases and Eu-Chalcogenides*, Hyp. Int. (submitted).

18. H. K. Mao, J. Xu, V. V. Struzhkin, R. J. Hemley, W. Sturhahn, M. Y. Hu, E. E. Alp, L. Vacadlo, D. Alfe, G. D. Price, M. J. Gillan, M. Schwoerer-Böhning, D. Häusermann, P. Eng, G. Shen, H. Giefers, R. Lübbers, G. Wortmann, *Phonon Density of States of Iron up to 153 GPa*, Phys. Rev. Lett. (submitted).